Quantitative imaging of vulnerable atherosclerotic plaque using MARS Spectral CT

A thesis submitted in partial fulfilment
of the requirements for the degree of

Masters of Science
in Medical Physics

School of Physics and Astronomy
University of Canterbury
New Zealand

Emily Searle

February 27, 2018

Abstract

This thesis details the novel use of the Medipix All Resolution System (MARS) Spectral CT scanner for quantitative imaging of vulnerable atherosclerotic plaque. The motivation behind this research was to see how well the MARS scanner could identify and quantify common components that are present in atheromas. Characteristic features of vulnerable plaque include a large necrotic lipid core, thin fibrous cap, increased inflammation, and intraplaque haemorrhage. The ability to identify lipid was investigated by joining high-Z contrast agents to low-density lipoproteins, enhancing the signal of a lipid component using spectral CT. Contrast agents were also implemented using U937 cells and macrophages, following the progressive lifecycle of the disease.

The elements iron and calcium were investigated in relation to their similar spectral profiles. With microcalcifications attributed to plaque instability, and iron a key component in blood, and hence intraplaque haemorrhage, the ability to distinguish these materials is crucial for identifying vulnerable plaque features in a clinical setting. Phantom studies involving iron- and calcium- like materials were performed to optimise the phantom and scanning protocol. Misidentifications between specific material concentrations in the material decomposition underwent further analysis with new methods that used the energy information from the scan. This revealed that misidentified materials could be separated and distinguished with the spectral information, demonstrating the advantage of spectral CT for atherosclerosis imaging over other imaging modalities. With the coexistence of iron and calcium deposits in atherosclerotic plaque, a point of discussion surrounds the issue of whether the MARS scanner can identify these two materials simultaneously, given there is a large enough signal. This was investigated through a mixed phantom of iron- and calcium- like solutions, to determine the point at which the iron signal predominates, and predominates over every other signal. In time, improvements to the scanner and the material decomposition software will lead to reduced misidentification of materials, and stronger distinction between iron and calcium .

The experiments performed throughout this thesis contribute to the field of atherosclerosis and the capabilities of the MARS Spectral CT scanner to identify and quantify elemental features of vulnerable plaque. With the MARS team fast approaching the goal of bringing multi-energy CT to human scanning, this research establishes firm ground for continued atheroma studies to help bring spectral CT to clinical imaging of atherosclerosis.

Acknowledgements

I would like to thank my supervisory team for all their guidance and encouragement throughout this past year. To Prof. Anthony Butler and Dr Aamir Raja, your regular meetings always provided me with valuable direction, reinforcing my morale whenever it wavered. To Assoc. Prof. Steven Gieseg, your passion for the field of atherosclerosis is something I truly admire. Thank you also to Steven Marsh, for showing interest in my progress throughout the year, and to the now retired Nigel Anderson, for always believing in my thesis story.

Thank you to the MARS group for offering me such an amazing project with the atheroma group. All members have such an admirable passion for their research and work as great team, one I look forward to joining as I commence further study with them through a PhD. I have enjoyed every minute, having the opportunity to learn new skills and meet new people. Thank you to Hannah Prebble and Joe Healy, for all the valuable discussions regarding experiment planning, either in person or via email, and to all my newfound friends in the Bioengineering office, you guys are superstars. Mention must also be given to Arron Dyer, Sarah Rogers and Erin Lally at the Christchurch School of Medicine (CSM), for always being a friendly face in the lab. Special thanks to Arron for answering every query and teaching me everything rodent related, I really appreciated learning these skills from you.

Finally, I would like to express my thanks to all my family and friends for your infinite support during my studies. To my friends near and far, I've valued all the encouragement you've given me in times of self doubt. To my twin sister Charlotte, you have been my no.1 fan from day one, and I can't thank you enough for the love and advice you've given me this past year. To Mum and Paul, Dad and Rose, you have created a determination in me to succeed that I am truly grateful for, and the completion of this thesis is in no small part attributed to your hard work and support. Thank you.

Academic Contribution

During the course of this thesis I have contributed to the MARS project through the clinical field of atherosclerosis, performing experiments relating to the distinction of elemental components of atherosclerotic plaque, including lipid, iron, and calcium. The following contributions have also been made, laying a strong foundation for continued atherosclerosis studies using spectral CT.

- Co-author in the following paper, which has been accepted for publication in Immunobiology:
  Hannah Prebble, Sean Cross, Edward Marks, Joe Healy, **Emily Searle**, Raja Aamir, Anthony Butler, Justin Roake, Barry Hock, Nigel Anderson, and Steven P Gieseg,
  Induced macrophage activation in live excised atherosclerotic plaque.

  This paper examined whether macrophages in plaque can be activated and compared this to monolayer cells. The volume of calcium in the plaque was compared to the level of macrophage activation measured by total neopterin output. The calcium content of two plaques was investigated by spectral imaging. There was an inverse association (R2 = 0.91) between the volume of calcium and macrophage activation as measured by total neopterin production in stimulated plaque tissue. Resident macrophages within excised carotid plaque activated either directly or indirectly generate the biomarkers 7,8-dihydroneopterin and neopterin. Macrophage activation rather than the oxidative environment is associated with plaque calcification. My contribution was scanning the plaque specimens and the calibration phantom.

- Co-author in the abstract presented at the 2017 Annual Scientific Meeting of the Australian Atherosclerosis Society held in Sydney:
  Gieseg SP, Healy JL, Prebble HM, Panta RK, **Searle E**, Aamir R, de Ruiter NJA, Bateman CJ, Walsh MF, Bell ST, Anderson NG, Butler APH, Butler PH, White V, Roake J,
  Spectral imaging of unstable atherosclerotic plaque by MARS-scanning.

  This presentation showed results of human carotid plaque specimens scanned with the MARS scanner. Known indicators of unstable plaque including micro-calcification, necrotic lipid core, ulceration and fibrous cap at a resolution of approximately 100 microns were identified. Staining of selected specimens for lipids showed the MARS imaging cameras

and software were correctly identifying the components of the plaque. My contribution was scanning the plaque specimens and the calibration phantom to perform material decomposition. I optimised the plaque images using the MARS Vision software to be presented by Steven Gieseg at the Annual Scientific Meeting.

- Co-author to a paper accepted as an abstract for the Biomaterials conference to be held in April 2018:
  Hannah M. Prebble, **Emily Searle**, Raja Aamir, Nigel Anderson, Anthony Butler, and Steven Gieseg, Labelling Low-Density Lipoprotein with Gold Nanoparticles or Iodine Prevents Uptake in U937 cells.

  This study investigated attaching contrast agent directly to LDL, to identify foam cells. To test this, a monocyte-like culture line, U937, was used, which can be differentiated into macrophage-like cells. It was possible to label LDL with iodine or gold nanoparticles at low concentrations (10mg/ml) that are measurable using spectral x-ray imaging. However, labelled LDL did not appear to be taken up by cells. My contribution included scanning the U937 phantom with the cell samples and calibration vials. I performed material decomposition on the phantom, and attempted to identify a gold and iodine signal in the labelled U937 samples.

- Helped with the day-to-day supervision and activities of summer research student Harshil Gulati, who undertook work with atherosclerotic plaque scanning.

- I became the main person responsible for the apoE mice colony. This entails completing a monthly mouse register, and completing ethics approval applications to euthanise animals for tissue through the Animal Ethics Committee. Throughout the timeframe of the thesis, I completed animal training through the Animal Welfare Office module training, completing modules including Ethics and Legislation, and Experimental Techniques (rodents). These techniques will be carried through to any further research using the apoE colony.

- Developed additional Matlab code to complement the PCA code, which generated an average slice from multiple slices chosen, rather than analysing just one slice. This optimised the PCA results. This code will get passed onto the Vision group within the MARS team for other members to utilise.

- Presented results at regular Atheroma meetings with members of the atheroma group throughout the year, which allowed for guidance to be given for future experiments.

Contents

List of Figures

List of Tables

Chapter 1

Introduction

This thesis details work contributing to the quantification of vulnerable atherosclerotic plaque features using MARS spectral CT. Spectral CT technology is at the forefront of the medical imaging field, with the ultimate goal of the MARS team being the establishment of a commercial spectral CT scanner for clinical use. The goal of this thesis is to set out a framework for atherosclerosis imaging using the MARS scanner. This was achieved by investigating the main components that feature in vulnerable atherosclerotic plaque. Each component of vulnerable plaque is organised into a designated chapter, including experiments involving lipid characterisation, and the distinction between calcifications and iron deposits. It demonstrates that spectral CT can image and quantify biological progresses taking place at a molecular level, through the use of high-Z contrast agents such as iodine and gold nanoparticles.

The visualisation of low contrast materials such as lipid is difficult in conventional CT, where the separation between materials is not easily recognisable in greyscale images. This thesis accesses the high-Z contrast agents iodine and gold joined to low-density lipoproteins (LDL's), to image and quantify the amount of nanoparticles joined to LDL's through the material decomposition. The motivation for this was based on the stages of plaque progression, where LDL's are initially recruited to the arterial wall due to a dysfunction of the endothelium [1]. Further contrast agent studies lead to the application of a human macrophage cell line known as U937 cells. The amount of contrast taken up by the cells more closely resembles the mechanism of uptake in human cells in atherosclerosis progression.

This thesis also delves into the matter of distinguishing iron and calcium. Iron is the material component of vulnerable plaques that represents the feature of intraplaque haemorrhage. Calcium relates to both the prevention and progression of plaque vulnerability. Large calcified regions provide plaques with stability, while microcalcifications indicate destabilisation of the atheroma. The major challenge in separating these materials relates to their similar spectral profiles. Neither material has a k-edge within the diagnostic energy range (20 - 120 keV), and hence exhibit similar Compton and photoelectric contributions to their attenuation coef-

ficients over the energy range investigated [2]. As a result, iron and calcium cannot be easily distinguished using material decomposition. Phantom studies investigated the ability to separate these materials on the energy information collected from each scan, with new methods comparing the material decomposition result with the material separation at each energy range.

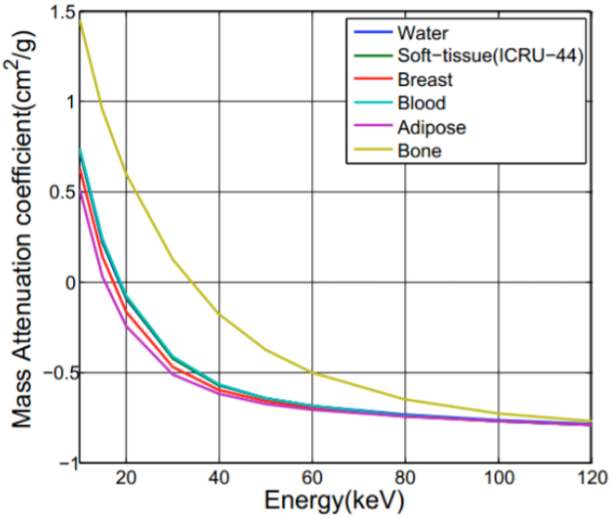

Figure 1.1: A logarithmic plot of x-ray attenuation for different human tissues as a function of x-ray energy. It illustrates that the attenuation difference between tissues is maximum at the lower energies and decreases with increasing energy. Notice bone (calcium) and blood (iron) have no k-edge jump within this energy range, and hence cannot be easily distinguished within the diagnostic energy range.

Throughout the timeframe of this thesis, multiple excised plaque specimens and atherosclerosis mouse models were scanned and visualised using the MARS Spectral scanner. The results of the optimised images produced are showcased in this thesis, demonstrating the abilities of the MARS scanner to obtain multi-energy datasets from a single acquisition using a standard x-ray tube operated at a single accelerating voltage [3]. Compared to current clinical imaging techniques, multi-energy CT is a superior imaging modality for atherosclerosis research, providing images with improved contrast, spatial resolution, and a reduction in imaging artefacts. With the MARS technology in the process of being adapted to a commercial, human-sized scanner, the clinical applications of spectral CT and the ability to improve patient treatments will be fully realised.

My contribution in the MARS project is mentioned in the previous section of Academic Contribution. This chapter introduces the motivation of the thesis and the goals of the Medipix All Resolution System (MARS) research group. The clinical relevance of this work is given in section 1.1. An overview of spectral CT imaging and the MARS scanner is provided in section 1.2, with a thesis outline provided in section 1.3.

1.1 Clinical Significance

The ability of the MARS Spectral scanner to simultaneously acquire high resolution images with spectral information creates the potential for major clinical advances. The utilisation of high-atomic number materials as contrast agents enables the MARS scanner to show the presence of these nanoparticles bound to biological samples in regions activated by vulnerable plaque rupture. This allows for identification and quantification of inflammatory components of vulnerable plaque, a feat not yet achieved with other imaging modalities. Recognition of plaque vulnerability is paramount to successful prevention of thrombotic events in patients, such as a stroke or myocardial infarction.

Atherosclerosis is a progressive but silent killer, with usual measures put in place too late before consequences present themselves. In New Zealand and across the world, cardiovascular disease is the leading cause of death. 33% of New Zealand deaths are attributed to the disease annually, with 172,000 New Zealanders living with heart disease [4]. Current imaging methods for patients presenting with a transient ischaemic attack measure plaque size as a basic tool for determining whether the patient requires endarterectomy or continued medical assessment [5]. Spectral molecular imaging has the potential to identify active disease activity, hence providing personalised preventative treatment for stroke patients. Patients susceptible to coronary artery disease could have unstable lesions identified and stented, thus directing treatment to prevent a myocardial infarction occurring [5]. As the MARS group prepares to transition to human scanning in coming years, this technique could facilitate in vivo visualisation and assessment of atherosclerotic plaques in patients ahead of treatment, effectively streamlining the selection of candidates for surgery, and the ability to monitor atherosclerosis disease.

1.2 Background

Spectral computed tomography (CT) is shifting the traditional view of medical imaging, revolutionising the way medical professionals and researchers view and interpret CT images. This technology has the ability to image in colour by using energy-resolving detectors to acquire spectral data [3], succeeding greyscale CT from which it is based. Spectral molecular imaging is opening avenues for interpretation of images and diagnosis of diseases which were not achievable or fully exploited with conventional CT.

The imaging modality of CT uses a polychromatic x-ray source to produce a 3D image of an object being scanned. The image is attained due to the photon interactions within the object. As x-rays of varying energies are emitted from the source and travel through the object, the photons are attenuated to different degrees depending on the material's atomic composition, and the energy of the respective photons. Conventional CT encodes the attenuations from different materials in greyscale (Hounsfield Units) by using energy integration detectors across the entire

broad x-ray spectrum. The issue surrounding this tactic is that different materials appearing in the CT image may have similar, if not the same, Hounsfield Units at specific concentrations. Therefore, these materials cannot be distinguished from each other, and the energy dependent characteristics of the materials attenuation are not observed.

Spectral CT acquires attenuation information by measuring x-ray absorption at multiple energy ranges. This is achieved by dividing a single energy spectrum into separate energy bins to extract energy information from the x-ray beam. By sampling several sections of the energy spectrum simultaneously, this provides a range of energy-dependent Hounsfield units across the spectrum [5]. For the energy range relevant to diagnostic imaging, x-ray interactions are predominantly a combination of the photoelectric effect and Compton scatter. The photoelectric effect is the release of an electron from the innermost shell of an atom (the K shell) by a photon with an energy greater than the binding energy of the K shell [6]. This is depicted by the spike in attenuation in a materials' spectral profile, representing the total energy of any incoming photon being absorbed. Compton scattering is the collision of photons with valence electrons of the outermost shell of an atom. In this collision, the energy of the incoming photon is not fully absorbed, leading to photon scatter.

Materials have specific spectral profiles based on their distinctive energy-dependent attenuation characteristics. For each material, this relates to differences in the photoelectric effect at low photon energies and the stability of Compton scattering at higher photon energies [7]. The Hounsfield units of high-atomic number (high-Z) materials decrease with energy as the effect of photoelectric absorption diminishes, whereas the Hounsfield units for low-Z materials increases with energy. This gives each material a unique Hounsfield unit shaped spectral profile, including k-edge peaks relating to the composition of the material. Both photoelectric effect and Compton scattering are energy dependent, and thus spectral decomposition is feasible with CT data acquired over at least two energy bins [3].

The MARS Spectral scanner is a multi-energy system that uses an energy-discriminating Medipix detector, capable of measuring the attenuation of x-rays in various energy ranges. The MARS scanner uncouples the x-ray spectrum into separate energy bins to extract energy information from the x-ray beam. The photon-processing abilities of the Medipix3RX detector implemented in the scanner enables high atomic number materials to be identified through their respective K-edges, which are observed by the sudden increase in attenuation due to photoelectric absorption of the photons [8]. In this arrangement, when a photon collides with the Medipix3RX detector, a current pulse is generated proportional to the energy of the detected x-ray photon [6]. If the energy of the detected photon is above the energy threshold on the detector chip then it is counted. Subsequently the detected photon is allocated to a respective energy bin, providing energy-selective images. By setting limits on the energy bins for a ma-

terial of interest, a specific material can be detected more easily. As such, sampling selected photon energy bins simultaneously allows characterisation of tissues on the basis of the k-edge behaviour of the materials making up the tissue [6].

Current imaging modalities have been implemented to study atherosclerosis, but are limited in assessing plaque vulnerability. CT is an excellent calcium quantifier, but cannot distinguish or quantify components of vulnerable plaque if they occupy the same voxel [7]. Magnetic resonance imaging (MRI) is able to distinguish components of vulnerable plaque, but cannot accurately quantify necrotic lipid cores [9]. Dual-energy CT (DECT) acquires images at two x-ray energy levels, however the modality is limited by the inconsistency between low and high x-ray energy data, resulting in beam-hardening artefacts [7]. The combination of high spatial resolution with improved intrinsic soft tissue contrast and specificity gives spectral CT the potential to characterise features of vulnerable plaque.

(a) Picture of MARS spectral scanner.

(b) Picture of the MARS gantry.

Figure 1.2: The MARS spectral scanner.

The MARS group is a multidisciplinary team of physicists, medical physicists, clinical radiologists, mathematicians, engineers, computer scientists, and biologists. Based at the University of Canterbury, the MARS group works alongside the University of Otago and their associated partners. A significant partnership is with CERN in Geneva, where the Medipix detectors are developed. At present, MARS spectral CT has been implemented at the pre-clinical stage, in a small animal scanner suitable for scanning phantoms, small animal models and excised tissue samples. The future focus of the MARS group is translating this technology to develop a commercial, human scale MARS scanner suitable for clinical use.

1.3 Thesis Outline

This thesis reports on the contributions made towards quantifying and identifying features of vulnerable atherosclerotic plaque. The present chapter provides a background to x-ray physics and spectral CT technology. The experimental work covering the lipid component of atherosclerosis is covered in chapter 2. Chapter 3 details experiments performed to distinguish iron from calcium. A new analysis method PCA is developed in chapter 4, using results from experiments in chapter 3. Chapter 5 showcases the ability of the MARS spectral scanner with plaque specimens and apoE mice material decomposition results. A conclusion to the thesis is given in chapter 6. Detailed summaries for chapters 1-5 are provided below.

Chapter 1 provides an introduction to the thesis, including the motivation of the project, the goal of the MARS team, and the clinical significance in the field of atherosclerosis. An outline of the contents of the thesis is also given.

Chapter 2 introduces lipid, an important feature of vulnerable atherosclerotic plaques. The use of nanoparticle contrast agents for plaque imaging is introduced. Experiments joining high-Z contrast agents are explored through the various stages of plaque progression. Material decomposition performed on the phantom studies reveals the nanoparticles' ability to visualise and quantify lipid components in plaque.

Chapter 3 discusses the components of iron and calcium, and their importance in determining plaque stability and indicating plaque vulnerability. The coexistence of these materials is investigated in an attempt to separate their spectral signals. The experiments aim to optimise the phantom and scanning protocol used throughout this chapter.

Chapter 4 provides an overview to Principal Component Analysis, an analysis technique applied to the spectral datasets in Chapter 3 for evaluating the separation of materials. Improvements to the method are briefly discussed.

Chapter 5 showcases the potential of the MARS spectral scanner through numerous plaque and apoE mice scans. Material decomposition images are shown and interpreted by optimising the MARS MD visualisation settings. Issues with the material identification in the images are raised, with future experiments to improve material decomposition discussed.

Chapter 6 gives a conclusion to the thesis.

Chapter 2

Lipid

2.1 Overview

The aim of this chapter is to investigate lipid in atherosclerosis through experiments reflecting the composition of lipid in atheromas. The significance of this chapter enables visualisation and quantification of lipid components using spectral CT, facilitating the long term goal of vulnerable plaque recognition in patients and directing suitable treatment. This chapter provides a background to the lipid component of atherosclerosis and the processes involved in vulnerable plaque formation. The progression of atherogenesis is investigated through a sequence of experiments that follow the lipid lifecycle until its furthermost intention, the occurrence of a thrombotic event. This involves the use of high-Z material based exogenous contrast agents such as gold and iodine, which are essential for categorizing soft tissue biomarkers of vulnerable plaque within the human imaging energy range (20 – 120 keV).

Section 2.2 gives an overview of lipids in atherosclerosis and their role in a plaques progression to vulnerability. The use of nanoparticle contrast agents for plaque imaging is also introduced. The methods, results, and analysis of each lipid experiment are given in individual sections. Section 2.3 talks about the iodinated LDL experiment, while section 2.4 describes the experiment joining gold and iodine to native-LDL. Section 2.5 investigates the use of contrast agents joined to U937 cells for translation to a biological specimen. Section 2.6 gives insight to the experiment implementing gold nanoparticles to macrophages, with the chapter summary in section 2.7.

2.2 Lipid in atherosclerosis

Unstable or vulnerable plaque is an adverse component of atherosclerosis, with the risk of suffering a thrombotic event more dependent on the biochemical and cell composition of the plaque, rather than the lesions stenotic severity [11]. Following the systemic inflammatory process of atherosclerosis, vulnerable plaques are characterized having features including: (a) a large necrotic lipid core; (b) thin fibrous cap; (c) increased inflammation; (d) reduced collagen and

amount of vascular smooth muscle cells (VSMCs); (e) increased vasa-vasorum neovascularization; and (f) intraplaque haemorrhage.

Low-density lipoproteins

Lipids such as cholesterol and triglycerides are insoluble in water, hence they must be transported in association with proteins. Lipoproteins are particles that comprise a central core containing cholesterol esters and triglycerides surrounded by free cholesterol, phospholipids, and apolipoproteins. The governing role of lipoprotein particles is to transfer these lipids throughout the body in the extracellular fluid, facilitating the availability of fats to cells via receptor-medicated endocytosis. Plasma lipoproteins can be categorized into seven classes based on their size, lipid composition, and apolipoproteins: chylomicrons, chylomicron remnants, very low-density lipoproteins (VLDL), intermediate-density lipoproteins (IDL), low-density lipoproteins (LDL), high-density lipoproteins (HDL), and lipoprotein(a) (Lp(a)).

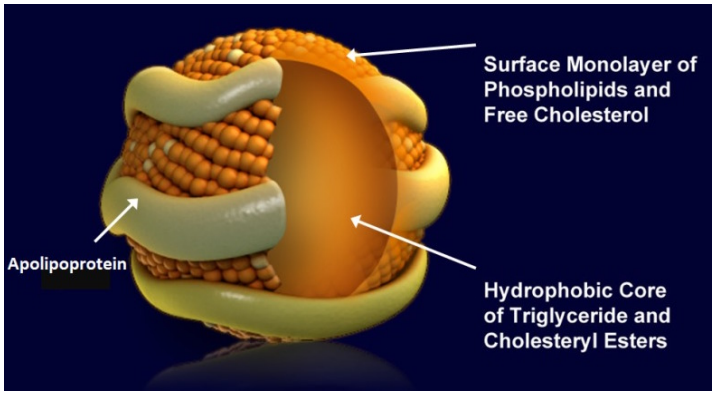

Figure 2.1: Image detailing the structure of a LDL particle. Accessed from [12].

The two main groups of lipoproteins are HDL and LDL. HDL particles are known as the 'good' cholesterol in the body, as they collect free cholesterol from peripheral tissues and transport these out of arterial walls [13], and reduce macrophage accumulation, potentially forestalling any onset of atherosclerosis. LDL particles are classified as the 'bad' cholesterol, as when they invade the endothelium, the oxidized forms they become are more easily retained by proteoglycans, and hence promote atherosclerosis development.

Apolipoproteins are proteins that bind lipids like cholesterol and triglycerides to form lipoproteins, and play a crucial role in lipoprotein metabolism. Their major functions include a) serving a structural role for maintaining the lipoprotein particle, b) acting as ligands for interaction with lipoprotein receptors in tissues (apoB100 and apoE for LDL-receptors, and apoA-I for HDL receptors), c) guiding the formation of lipoproteins, and d) serving as activators or inhibitors of enzymes involved in lipoprotein metabolism [12].

The role of macrophages

Macrophages are a type of white blood cell responsible for engulfing cellular debris, apoptotic cells, and other foreign bodies through phagocytosis. In atherosclerosis, macrophages contribute to size-dependent variations in plaque morphology, particularly the formation of the necrotic core and fibrous cap thinning [14]. Macrophages accumulated in plaques tend to have diminished ability to migrate, making it inactive in resolving inflammation and contributing to plaque progression. Through their death via necrosis or apoptosis, the immobile macrophages release their lipid contents to form the pro-thrombotic necrotic core [15]. The thin fibrous cap is the connective tissue layer that covers the necrotic core, and is composed of VSMCs and the extracellular matrix (ECM) they synthesise (predominantly collagen and proteoglycans). The fibrous cap also contains macrophage foam cells. The balance between the constituents within the ECM plays a vital role in maintaining the integrity of the fibrous cap, and its vulnerability to rupture [11].

Plaque progression

The development of atherosclerosis is initiated by the dysfunction of the endothelium, due to stimuli such as smoking, hypertension, or dyslipidemia. The endothelium is a semipermeable membrane that forms the inner layer of blood vessels, and controls the transit of materials in and out of the bloodstream [13]. A compensatory response to a disruption in the endothelium leads to recruitment of low-density lipoproteins (LDL's) by increasing the endothelium's permeability, allowing adhesion and migration into the arterial wall. A focal area for this migration is at branch points of the arterial tree, which encounter laminar flow disturbance [16]. The LDL's are retained in the intima through the binding of apolipoproteins B100 to negatively charged proteoglycans of the ECM[17][18].

As the LDL particles accumulate, they undergo chemical modifications inside the intima. Oxidation of the LDL particles renders them pro-atherogenic. This results from the chemical reactions of reactive oxygen species (ROS) and pro-oxidant enzymes produced by the endothelium, smooth muscle cells (SMCs), or macrophages penetrating the intima to induce oxidative stress [19]. As the LDL particles are progressively oxidized, they are capable of acting as a chemoattractant, exerting their pro-atherogenic effects to recruit leukocytes (monocytes and lymphocytes), which migrate into the intima. This generally occurs in preferential areas where the subendothelial layer is abundant with oxidized LDL particles [11].

When monocytes enter the intima, they differentiate into phagocytic macrophages and express scavenger receptors. LDL particles that are completely oxidized, as characterized by an increased apolipoprotein B100 negative charge, are recognized by the scavenger receptors and internalized to form foam cells, the hallmark of vulnerable atherosclerotic plaques [17]. The inflammatory response for plaque formation is perpetuated through the release of cytokines,

growth factors, metalloproteinase (MMP) and ROS, all playing a continued role in inducing vascular remodeling and escalating the plaque's susceptibility to rupture and likelihood of a thrombotic event.

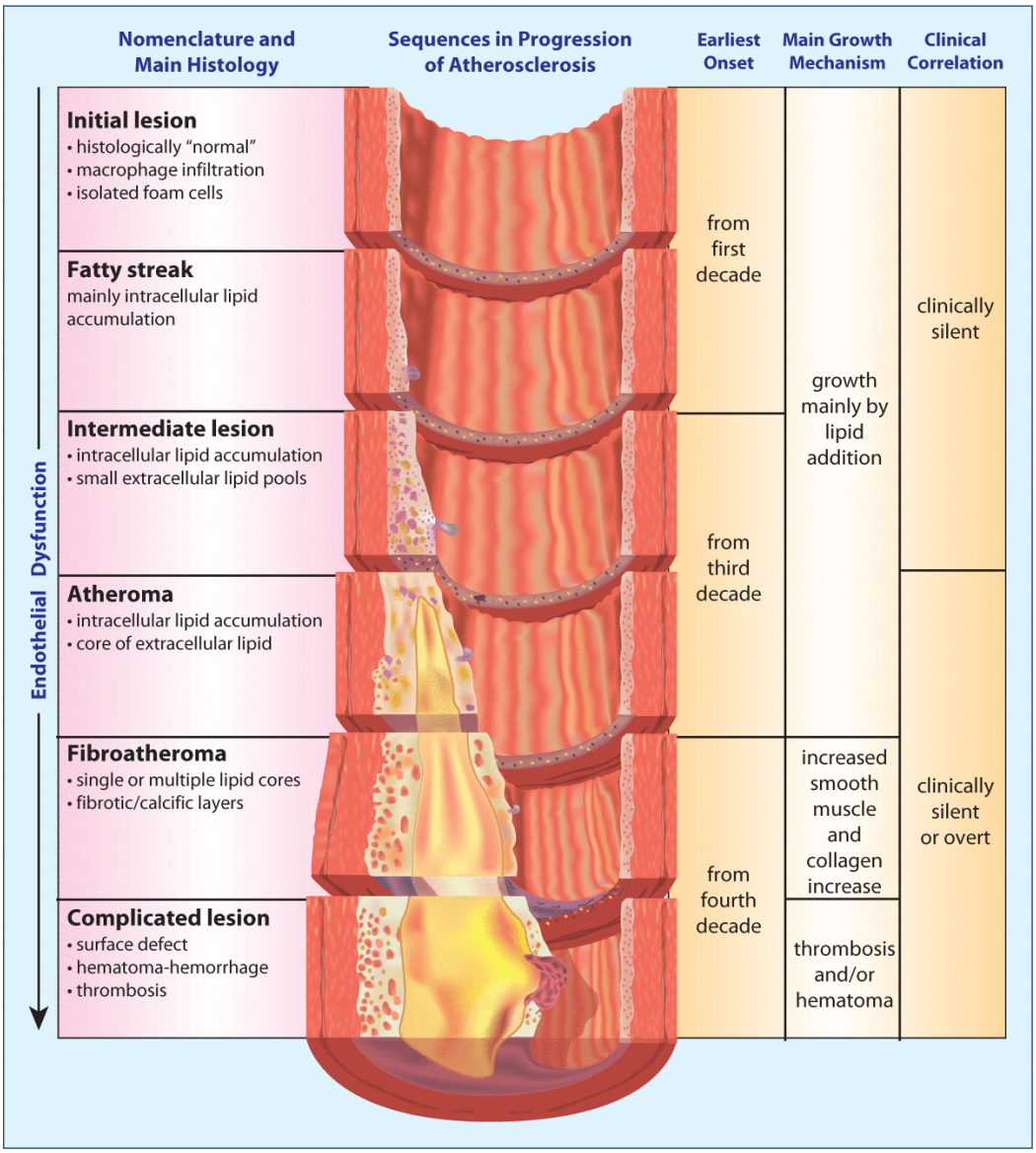

Figure 2.2: Image detailing the progression of atherosclerotic plaque to vulnerability. As a necrotic core is increasingly remodelled, the plaque is prone to a thrombotic event, resulting in a stroke or myocardial infarction. Image accessed from [20].

Nanoparticle contrast agents

The use of contrast agents in medical imaging is essential for soft tissue visualization. Materials with a high atomic number (more than 40 protons in the nucleus) have unique x-ray absorption edges known as k-edges, which are within the diagnostic energy range. The energy of the attenuation k-edge is characteristic for each element. Implementation of high-Z contrast agents enables spectral imaging to detect and quantify biomarkers in soft tissue components that are

low contrast, such as lipid [5].

Nanoparticles can be engineered for successful targeted labeling in imaging, overcoming many biological, biomedical, and biophysical barriers [21]. One fundamental challenge is packing the nanoparticles in sufficient numbers for accurate distinction and quantification. Gold has several advantages compared to iodinated contrast agents, achieving a contrast up to 3 times greater than iodine per unit mass at $\sim$ 100keV. Additionally, gold nanoparticles have very low viscosity and osmolality (number of moles of solute per kilogram of solvent), and carry more gold atoms per molecules than iodine (250 atoms of Au compared of 3-6 atoms of iodine) [22]. These factors make gold a sought after radiopharmaceutical in research.

A past study employed gold containing HDL (Au-HDL) nanoparticles to visualize atherosclerotic plaque in the abdominal aortas of apoE$^{-\backslash -}$ mice using spectral CT [23]. Areas of high attenuation were attributed to the accumulation of Au-HDL, which were found to largely localize in macrophages. This high attenuation was observed in regions susceptible to atherosclerotic plaque formation, such as the aortic arch, the region near the renal arteries, and the bifurcation [24]. Colloidal gold has also been explored as a non-degradable marker joined to LDL's, for studying receptor binding and endocytosis. Conjugation of LDL to colloidal gold occurs by electrostatic surface absorption due to the negative charge of the gold particle. As the colloidal gold is completely enclosed within a surrounding monolayer of LDL particles, it is easily identified within the cell and presents a totally biological surface for cellular interaction [25]. Experiments tracking gold nanoparticles labeled to LDL particles have been successful in visualising lipoprotein biointeractions in vitro and in a tumour mouse model [26]. It was shown that Au-LDL expressed similar characteristics to native LDL in regards to size, morphology, composition, ApoB100 function, oxidation state, and molecular weight. With Au-LDL permitting the uptake by macrophages, hepatocytes and a melanoma cell line in vitro through receptor dependencies, the study supports the use of gold as a marker to study LDL interactions, cholesterol metabolism, and atherosclerotic plaque progression [26].

2.3 Iodinated LDL experiment

2.3.1 Aim

In this experiment, the objective was to join a contrast agent such as iodine to low-density lipoproteins (LDL's), which could be visualized in the scanner as a result of the agent's high atomic properties. This experiment is significant because lipid is a low contrast material, meaning it doesn't observe an increase in attenuation through a k-edge, hence it is difficult to distinguish from other tissue-like components in conventional CT. Successfully joining a high-Z material would allow lipid regions in atheromas with accumulated LDL to be enhanced using spectral CT.

2.3.2 Methods

A member of the MARS team undertaking their PhD in Biological Sciences prepared the LDL samples in this study and following experiments.

Plasma was obtained from healthy donors under ethics approval CTY/98/07/069 granted by the Upper South (B) Regional Ethics Committee. LDL was isolated from donor plasma using a centrifugation gradient separation method as described by Gieseg and Esterbauer (1994). Isolated LDL was washed with phosphate buffered saline (PBS) using an Amicon Ultra-15 membrane filter centrifugation tubes (Millipore, USA) at 3000 g, 4 C for 30 minutes, and repeated twice. LDL concentration was adjusted to 10 mg (LDL total mass) per mL, which was determined using a total cholesterol assay kit (Roche Diagnostics, Germany), assuming the total cholesterol accounts for 31.69% of the LDL particle (MW 2500kDa).

This first attempt included prepared liquid and precipitated LDL samples that were either in its native form (control) or iodinated (I-LDL). These were at a concentration of 10mg/ml LDL, and the method used should have added 20 iodine atoms per LDL particle. The four PCR tubes containing the LDL were ordered as follows:

- Liquid n-LDL (in phosphate-buffered saline (PBS)).
- Liquid I-LDL (in PBS. Iodinated the LDL using iodine monochloride).
- Pelleted n-LDL (pellets in 50% water, 50% trichloroacetic acid (TCA). Precipitated with TCA).
- Pelleted I-LDL (pellets in 50% water, 50% TCA. Precipitated with TCA. Iodinated the LDL using iodine monochloride).

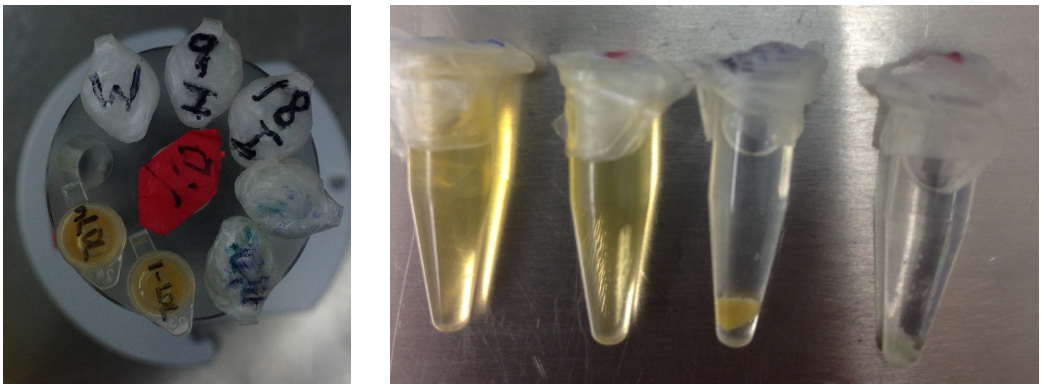

(a) Iodinated phantom. (b) Iodinated LDL samples.

Figure 2.3: Iodinated LDL phantom with the iodinated LDL samples in liquid and pelleted from. From left: liquid n-LDL, liquid I-LDL, pelleted n-LDL, and pelleted I-LDL.

The phantom contained these samples alongside standards for iodine at 9mg/ml and 18mg/ml (I9 and I18), lipid, and water. The FactoryProtocol_Al protocol was used, with an X-ray tube

voltage of 118 kVp, tube current of 13μA, and exposure time of 300ms. The four energy bins were set as 18.0 – 29.9 keV, 29.9 – 44.9 keV, 44.9 – 77.9 keV, and 77.9 keV - 118.0 keV.

2.3.3 Results and Analysis

To analyse the results from the scan, the reconstructed dataset labelled 'RECON' was downloaded from MARS Transfer. To identify the linear attenuation for each material in the phantom, the dataset was loaded into ImageJ, where math processing was performed to generate rescaled, 32-bit images. To initiate material decomposition (MD) of the dataset, the linear attenuation values for the iodine standard concentrations and water across the four energy bins were inputted into a Matlab code, which separated the water signal from the material to calculate the material bases. The high-Z element and water material bases, along with the lipid linear attenuation values, were saved in a config file, which was subsequently used to run the MD with the reconstructed DICOM dataset.

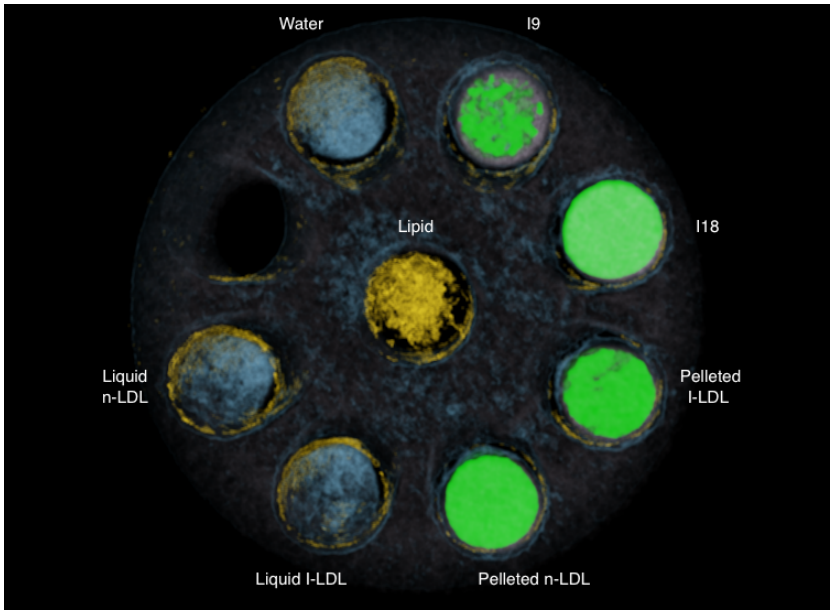

Figure 2.4: Material decomposition of iodinated LDL phantom using MARS Vision. Iodine signal is green, water is blue, and lipid is yellow.

By performing material decomposition on the reconstructed dataset, the above MARS Vision image was produced. The minimum threshold of iodine in the LUT setting was selected as 0.009 to coincide with the lowest concentration of the iodine standard in the phantom at 9 mg/ml. By doing this, any iodine signal less then 9 mg/ml is eliminated, as it could be considered a misclassification. This is supported by the misidentification chart produced, which establishes 100% correct identification of I9 and I18 (Figure 2.5).

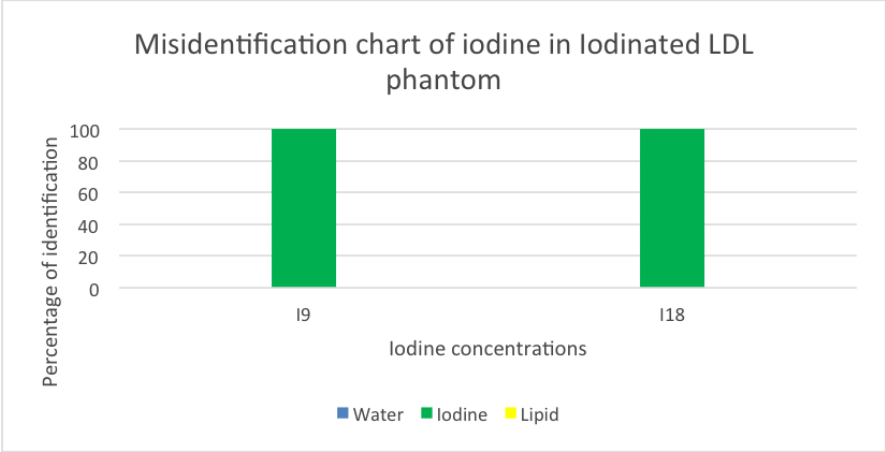

Figure 2.5: Misidentification chart for the standards of iodine used in the iodinated LDL phantom.

It was observed that at 10 mg/ml LDL, there was no measurable iodine signal in the liquid LDL samples in its native (control) or iodinated form. This is evident in Figure 2.6, with the spectral plot of the liquid I-LDL and liquid n-LDL samples having a trend similar to lipid. In the precipitated LDL, both the native and iodinated samples revealed a significant iodine signal not only in the pellet but also throughout the 50% water 50% TCA solution the pellets were held in. In Figure 2.6, the pelleted samples have Hounsfield units closely following I9, but do not exhibit the k-edge of iodine within the second energy bin, only showing a continued decrease in HU across the four energy bins.

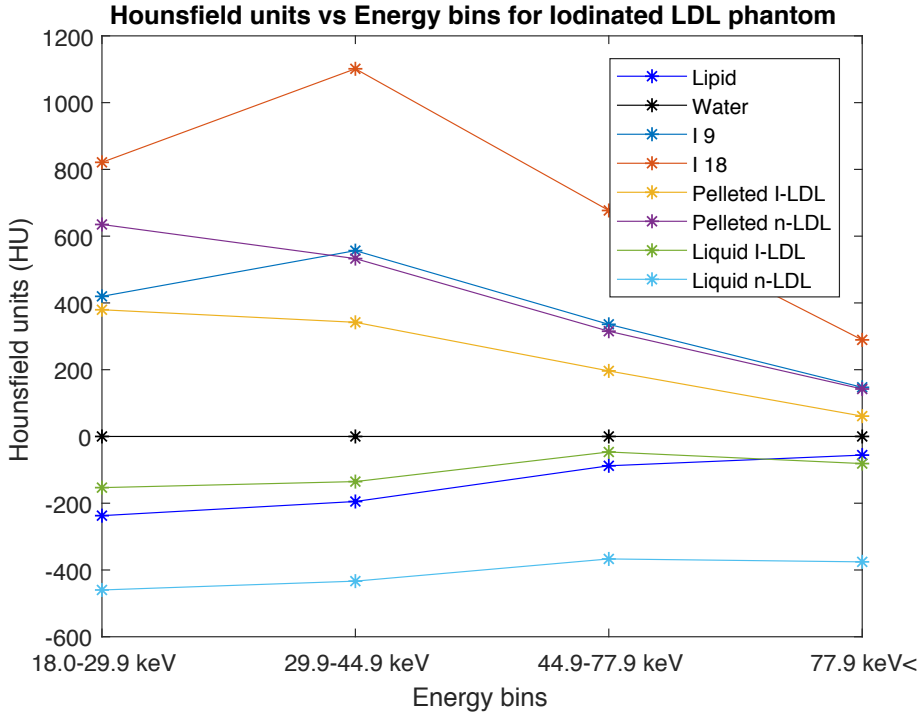

Figure 2.6: Spectral plot for the iodinated LDL phantom.

It was expected that an iodine signal would be detected in the I-LDL pellet alone, which led to the conclusion that chlorine atoms in the trichloroacetic acid (TCA), used for precipitation and was present within the solution that held the pellets, were responsible for the signal throughout the tube. The calibration phantom only contained standards for iodine at 9 mg/ml and 18 mg/ml, lipid, and water. A signal from the presence of chorine in the pelleted samples would not express as lipid or water, and therefore must identify as an iodine signal. To avoid this, all further precipitations were conducted using acetonitrile (ACN), with pellets held in air in the PCR tubes.

2.3.4 Conclusion

In this experiment, the aim of joining iodine to LDL was met in the precipitated samples (both native and iodinated). However, the samples prepared did not react as anticipated. Rather than the pellets displaying an iodine signal alone, the chlorine in the TCA solution contributed to the iodine signal. As a result of this finding, following experiments used pelleted samples held in air, to eliminate any unnecessary signal from materials/solutions other than the pellets.

2.4 Gold, iodinated, and native LDL

2.4.1 Aim

Following from the results of the first LDL experiment using iodinated LDL in pelleted and liquid form, a similar experiment was formulated with modification to the methodology. The objective was to observe how gold and iodine join to LDL's in pellets held in air, and verify their ability as contrast agents to be identified in the material decomposition of the scan result. The significance of this experiment enables joining of high-Z materials to LDL's in optimal conditions, allowing lipid, a low contrast material, to be enhanced using the MARS spectral scanner.

2.4.2 Methods

Iodinated LDL (I-LDL) was prepared by gently mixing 500uL of 20mM ICl in 2M NaCl with 1 mL of 10 mg/mL LDL. This solution was washed using ultra membrane filter tubes. Native LDL (n-LDL) was prepared in the same manner except with the addition of 500uL of PBS rather than ICl. Gold nanoparticle labelled LDL (Au-LDL) was prepared by mixing 500uL of 0.5 mg/mL AuNPs with 1 mL of 10 mg/mL LDL, a method modified from Handley, 1981 (Handley, Arbeeny, Chien, 1981). All solutions were filter sterilised through a 0.22 um filter prior to use in cell culture. To form LDL precipitates; 500uL of acetonitrile (ACN) was added to 500uL of LDL (native, iodinated or Au-labelled) in 1.7 mL eppendorf tubes and vortexed for 30 seconds. Precipitates were then centrifuged at 15,000 RPM for 10 minutes at 4 C to form pellets. The ACN supernatant was then removed and the pellets were removed with care from

the eppendorfs and placed into PCR tubes.

The phantom contained standards for gold at 4mg/ml and 8mg/ml, (Au4 and Au8), iodine at 9mg/ml and 18mg/ml (I9 and I18), lipid, water, and the three PCR tubes containing the 10mg/ml pelleted LDL's:

- Pelleted Au-LDL in air.
- Pelleted I-LDL in air.
- Pelleted n-LDL in air.

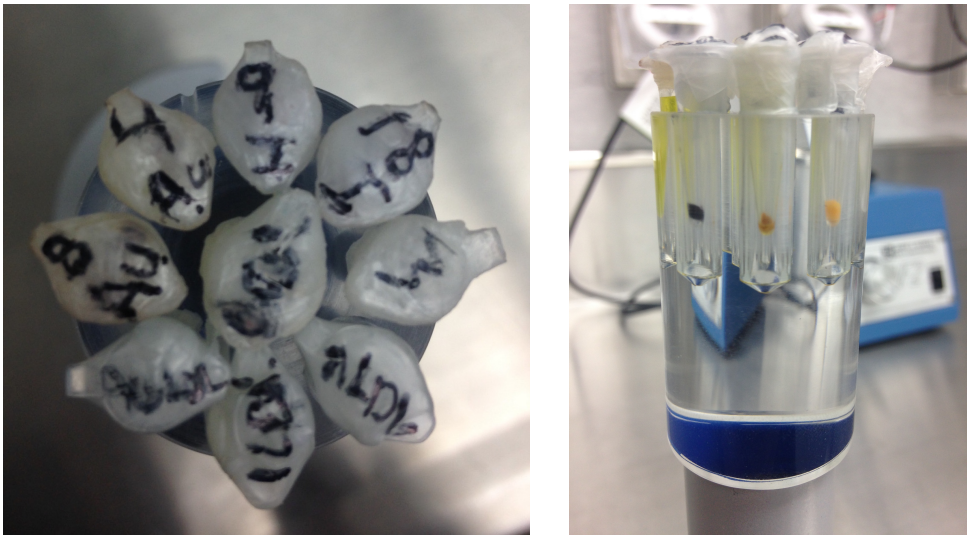

(a) Gold, iodine, and native-LDL phantom.

(b) Au-LDL, I-LDL, and n-LDL pellets.

Figure 2.7: Pictures of the gold, iodine, and native-LDL phantom. In (b), from left: Au-LDL, I-LDL, and n-LDL pellet.

The scan was completed using the FactoryProtocol_Al protocol using identical parameters as in the iodinated LDL experiment. The energy bin range used (18.0 - 29.9 keV, 29.9 - 44.9 keV, 44.9 - 77.9 keV, and 77.9 keV - 118.0 keV) incorporated the k-edge of iodine at approximately 33.2 keV, and captures the attenuation of gold in the higher energy, representing its k-edge at approximately 80.7 keV.

2.4.3 Results and Analysis

To optimise the MD image, the LUT minimum thresholds were set as 0.002 and 0.009 for gold and iodine, respectively, in relation to their misidentification charts for correct material classification at these concentrations (Figure 2.5) The following material decomposition of the phantom was produced.

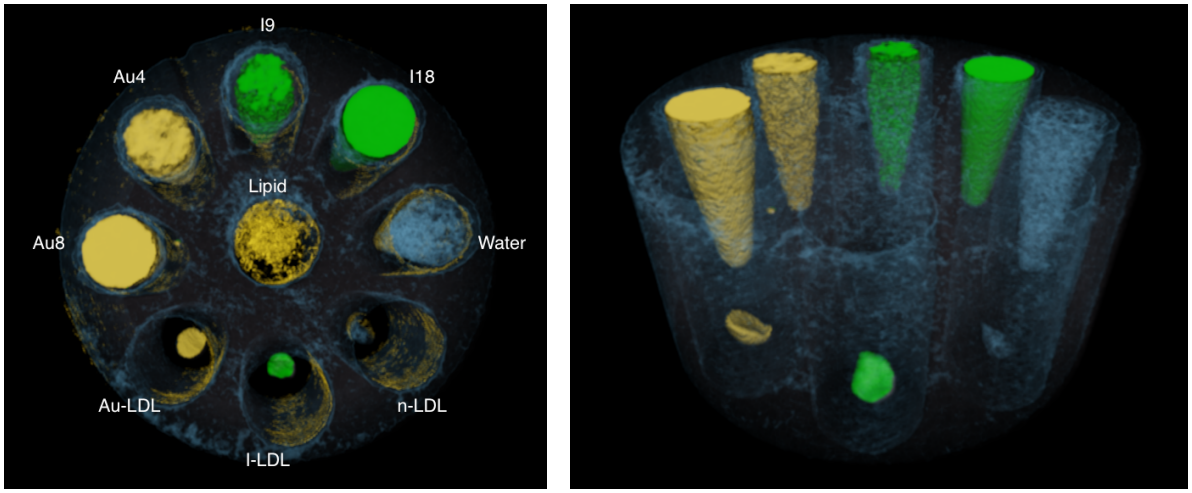

(a) Gold, iodine, and native-LDL phantom.

(b) Side view of gold, iodine, and native-LDL phantom.

Figure 2.8: Material decomposition of gold, iodine, and native-LDL pellets. Gold signal is shown as gold, iodine as green, water as blue, and lipid as yellow (centre vial). In (b), the lipid signal has been suppressed.

The spectral plot representing Hounsfield Units across the energy bins clearly displays the increase in attenuation at the second energy bin, illustrating the k-edge of iodine. The gold standards also show a small incline between the third and fourth energy bin, depicting the k-edge of gold at 80.7 keV. Most notable is the pronounced signal from the I-LDL pellet, which also follows the spectral profile of that of the iodine standards. In the second energy bin (29.9 – 44.9 keV) the I-LDL signal measures close to 4000HU, whereas the k-edge peak of the iodine standard I18 measures just over 1000HU. The Au-LDL pellet possesses a signal slightly higher than Au8. As expected, the control pellet containing LDL in its native form did not reveal any Au or I signal, and maintained a spectral profile between water and lipid.

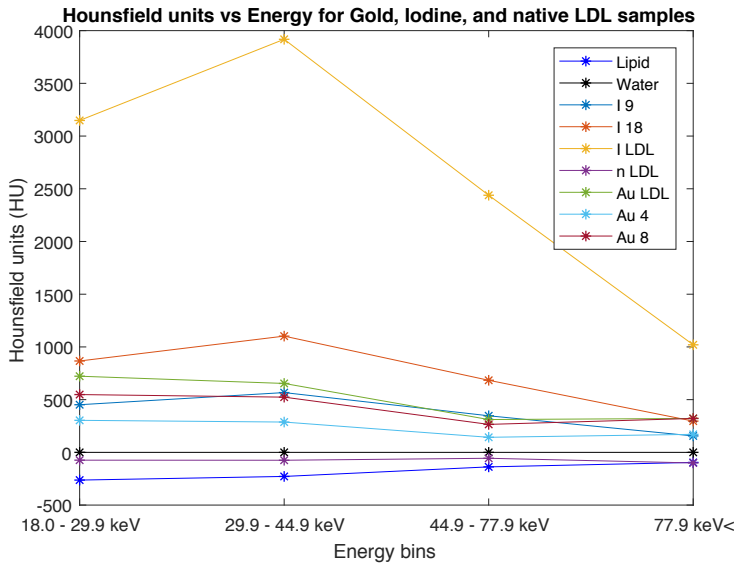

Figure 2.9: Spectral plot for the Au-LDL, I-LDL and n-LDL phantom.

Using MARS Vision, the concentration of gold and iodine in the Au-LDL and I-LDL pellet, respectively, was quantified by taking a measurement from an axial, coronal, and sagittal slice using the polygon tool to select the region of interest.

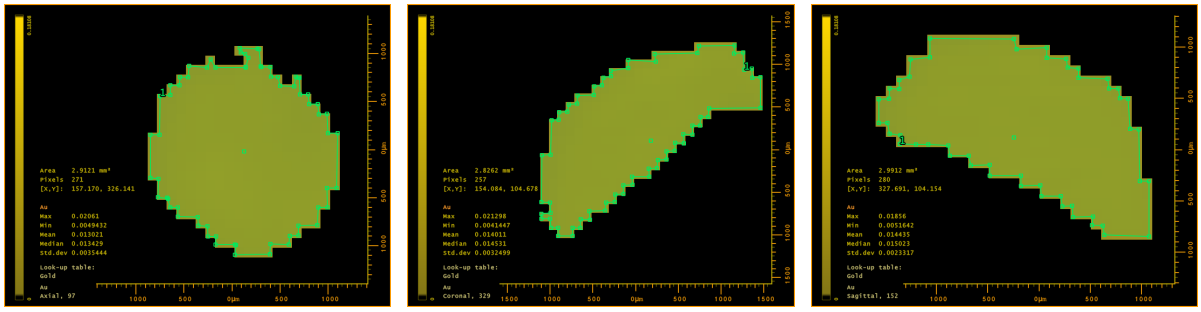

(a) Axial slice. (b) Coronal slice. (c) Sagittal slice.

Figure 2.10: Polygon selections for axial, coronal, and sagittal slice in Au-LDL pellet.

Au in Au-LDL pellet	Mean (mg/ml)	Standard deviation	No. of pixels
Axial	13.0207	3.54443	271
Coronal	14.5312	3.24986	257
Sagittal	14.4345	2.33171	280

Table 2.1: Quantity of gold in Au-LDL pellets, measured in an axial, coronal, and sagittal slice, as seen in Figure 2.10.

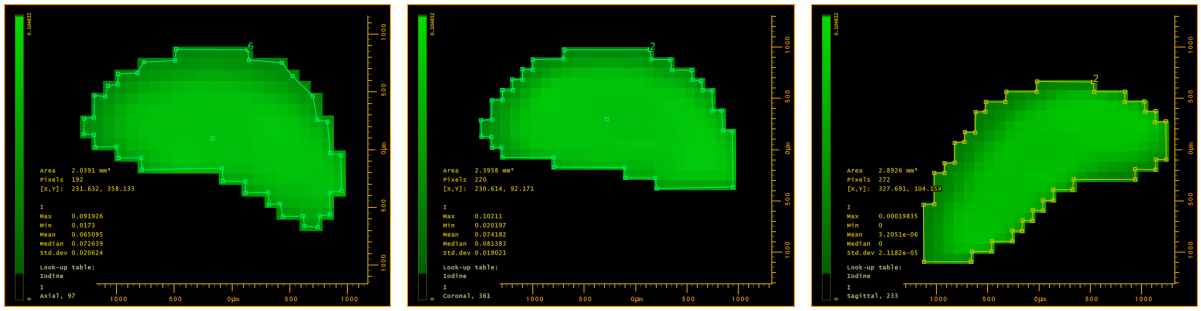

(a) Axial slice. (b) Coronal slice. (c) Sagittal slice.

Figure 2.11: Polygon selections for axial, coronal, and sagittal slice in I-LDL pellet.

I in I-LDL pellet	Mean (mg/ml)	Standard deviation	No. of pixels
Axial	65.0954	20.6237	192
Coronal	74.1821	19.0206	220
Sagittal	67.8592	22.6289	272

Table 2.2: Quantity of iodine in I-LDL pellets, measured in an axial, coronal, and sagittal slice, as seen in Figure 2.11.

2.4.4 Conclusion

This experiment effectively joined gold and iodine to 10 mg/ml precipitated LDL, with the material decomposition measuring a gold signal in the Au-LDL pellet in the range 13-14 mg/ml

across axial, coronal, and sagittal slices. Iodine measurements produced a significant signal in the I-LDL pellet, in the range 65-74 mg/ml across axial, coronal, and sagittal slices. The n-LDL produced no gold or iodine signal as anticipated, displaying as water in the MD.

With the success of joining gold and iodine to precipitated LDL and observing a signal at concentrations measurable using the MARS scanner, the experiment was translated to U937 cells, which are commonly used in research to study monocytic differentiation.

2.5 U937 cells with gold and iodinated LDL

2.5.1 Aim

The objective of this experiment, following the success of joining gold and iodine to 10mg/ml precipitated LDL in Section 2.4, was to use the human macrophage cell line known as U937 cells to attempt to observe the uptake of Au-LDL and I-LDL within the cells. Through the high atomic properties of the contrast agents, it is anticipated the MARS scanner will detect the uptake of the gold and iodine from the cells. The significance of employing a human macrophage cell line allows the amount of contrast taken up by the cells to more closely resemble the mechanism of uptake in human cells in atherosclerosis progression.

2.5.2 Methods

The U937 cells were cultured in RPMI-1640 media containing 5% fetal bovine serum (FBS). U937s were plated into 12 well plates (Nunc, Thermo Fisher Scientific, NZ Ltd) and differentiated for 24 hours with the addition of 100 ng/mL of phorbol-12-meristate-13-acetate (PMA). Cells were then treated with n-LDL, Au-LDL and I-LDL at a final concentration of 2 mg/mL for 24 hours. The supernatant was then removed and the U937 cells were lifted from the plate using 200uL of accutase. The resulting liquid was transferred to PCR tubes and the cells were pelleted by centrifugation (1500 RPM, 5 minutes at 20°C).

The U937 cell samples were scanned in a phantom containing standards for gold at 2mg/ml and 4mg/ml (Au2 and Au4), iodine at 9mg/ml and 18mg/ml (I9 and I18), lipid, and water.

- Au-LDL U937 cells in air.
- I-LDL U937 cells in air.
- n-LDL U937 cells in air.

The scan was run using the FactoryProtocol_Al protocol, with identical scan parameters to previous LDL experiments.

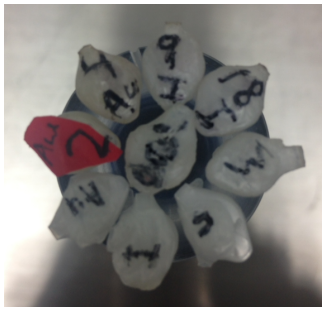

(a) Phantom for U937 cells experiment.

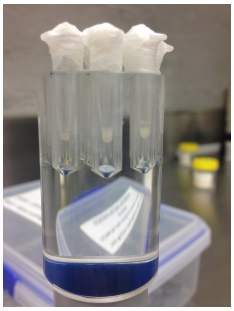

(b) Au-LDL, I-LDL, and n-LDL pellets joined to U937 cells.

Figure 2.12: The phantom for the U937 cells experiment. In b), from left: Au-LDL with U937 cells, I-LDL with U937 cells, and n-LDL with U937 cells

2.5.3 Results and Analysis

The U937 cells were differentiated to be macrophage-like using PMA, after the addition of Au-LDL and I-LDL. Initial observations of the pelleted U937 cells (2 million per pellet) revealed very little colour change, suggesting poor uptake of the Au-LDL and I-LDL. As a result, it was anticipated the cells might not produce a strong gold or iodine signal. It is noteworthy that the maximum LDL concentration that could be added to the cells was 2 mg/ml, which is markedly lower than the concentration used for the precipitates.

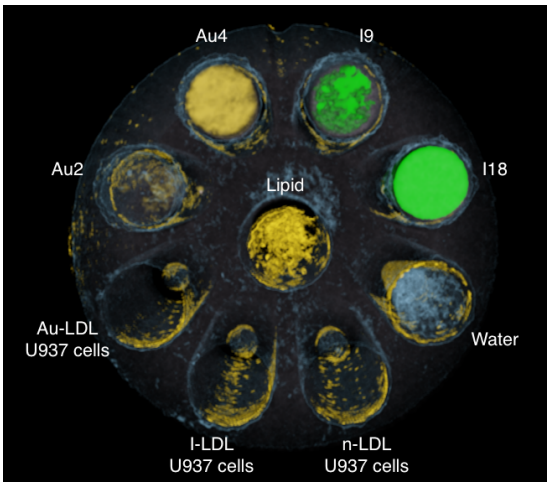

(a) Optimised MD image of the phantom for the U937 cells experiment.

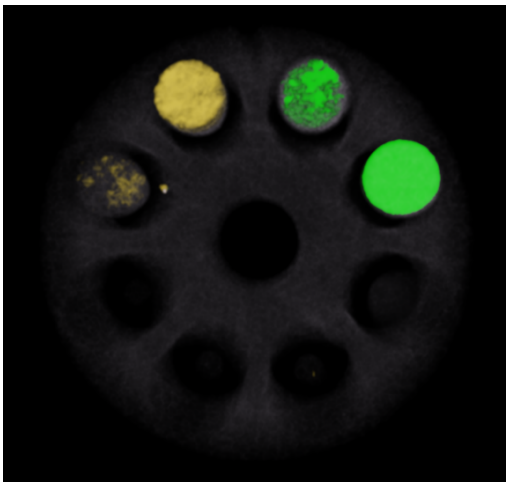

(b) MD image displaying gold and iodine signal only.

Figure 2.13: Optimised MD images of the U937 cells experiment phantom. In (a), the gold signal is shown in gold, iodine as green, lipid in yellow, and water as blue. In (b), the lipid and water signals have been suppressed to show the high-Z channels only.

The images were optimised on MARS Vision, with the LUT minimum threshold set to 0.002 for gold and 0.009 for the iodine channel. Due to the insufficient amount of LDL that could be added to the U937 cells, there was no gold or iodine contrast detected in the cell samples. This is evident in Figure 2.13b, which shows a gold and iodine signal only as part of the gold and

iodine standards.

The absence of contrast agent in the U937 cells is reflected in the spectral plot in Figure 2.14, which shows all three cell samples with signals especially close to water. They follow water's horizontal trend for the first three energy bins, with a decrease in attenuation below that of water for the fourth energy bin. The iodine standards express their characteristic k-edge profile in the energy range 29.9 – 44.9 keV, with an increase in attenuation apparent for the gold standards in the energy range 77.9 keV <.

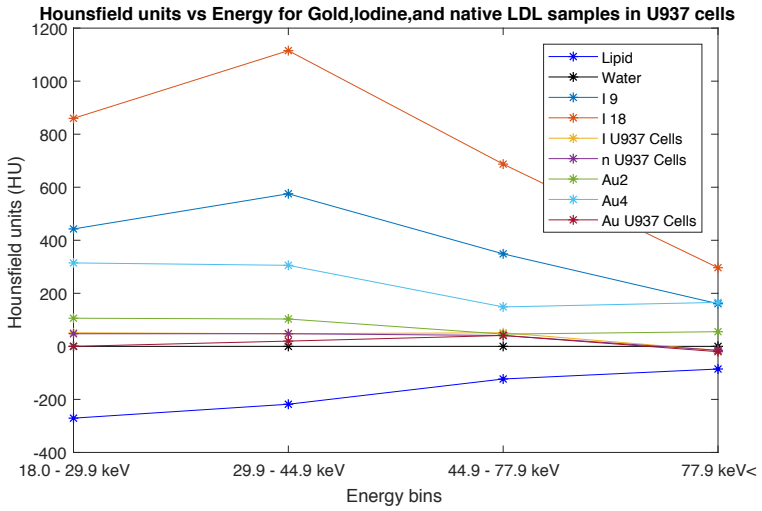

Figure 2.14: Spectral plot for the experiment joining Au-LDL, I-LDL and n-LDL to U937 cells.

A possible rationale for the unsuccessful detection of contrast agents in the U937 cells might be due to the uptake mechanisms of LDL. LDL is taken up in a regulated manner by the cells, whereas oxidized LDL is taken up by scavenger receptors in a completely uncontrolled way. This generally leads to foam cell formation. It may also be possible that the modification of LDL means that it is no longer recognised by the LDL receptor on U937 cells, or the LDL uptake is severely limited by the number of receptors available. For further LDL experiments, it may be worth using ox-LDL rather than native-LDL, which may increase the uptake by the cells. Another alternative is to look at increasing the number of iodine atoms or AuNPs per LDL, so there is a higher concentration of contrast agent per protein, and hence a higher expectation of detecting a signal if the rate of uptake remained the same.

2.5.4 Conclusion

The goal of observing the uptake of Au-LDL and I-LDL in U937 cells was unsuccessful due to poor uptake of the contrast agent by the cells. Further experiments using ox-LDL rather than native-LDL may increase the uptake and signal of the contrast agents. Discontinuing further LDL experiments for this thesis, movement towards macrophage cell experiments could allow the quantification of contrast agents within cell samples.

2.6 Macrophage experiment

2.6.1 Aim

The aim of this experiment was to measure the quantity of gold nanoparticles (AuNP) in two macrophage cell samples (one with serum and one without), and in their respective controls (cells only, with no AuNP). The significance of this experiment relates to macrophages contribution to necrotic core formation and plaque progression. The ability to visualise high contrast gold nanoparticles in macrophage samples could translate to plaque imaging in patients for signs of plaque vulnerability, such as necrotic core formation and fibrous cap thinning.

2.6.2 Methods

Primary cultures of human peripheral blood mononuclear cells (PBMC), which are a mixture of lymphocytes and monocytes, were isolated from donated fresh whole blood under ethics approval CTY/98/07/069. The mononuclear cells were prepared by density gradient centrifugation over Lymphoprep^{TM} (Axis-Shield PoC AS, Oslo, Norway), as described by the manufacturer, and washed in sterile phosphate-buffered saline (PBS) containing 150 mM sodium chloride and 10 mM sodium dihydrogen orthophosphate pH 7.4. The cells were plated in 12-well tissue culture plates (Nunc, ThermoFisher Scientific, Auckland, NZ) at 5×10^6 cells per mL in Roswell Park Memorial Institute (RPMI)-1640 containing penicillin (100 U/mL) and streptomycin (100 g/mL), supplemented with 10% human serum. Human monocyte-derived macrophages (HMDM) were prepared from the PBMC preparation by incubating for 40 h in serum-free RPMI before plating at 5×10^6 cells/well in RPMI-1640, as described for the PBMC, except 3 μg/mL of granulocyte-macrophage colony-stimulating factor (GM-CSF) was added to the media on the first day after plating but not added during subsequent media changes, which occurred every 3 d. The monocytes differentiated into adherent macrophages over 7 to 14 d.

The cells were grown in the tissue culture plate, in RPMI1640 with 10% human serum. The control cells were left in this for 24 hours and then the media was removed. 250uL of Accustase was used to lift the cells off the plate, which were then transferred to a 1.7ml eppendorf and centrifuged (2000rpm for 5 minutes) to generate a pellet. Any liquid was suctioned off with a vacuum. The control cells without serum were cultured for 24 hours just with RPMI, and pelleted the same method as the control cells containing serum. The cells with nanoparticles were produced by firstly concentrating the particles 10x, then adding 100uL (10x dil) to either RPMI only or RPMI with human serum. The nanoparticle concentration was about 150ug/ml. The same technique as above was used to generate the pellet.

The phantom used for the scan contained standards for gold at 2mg/ml, 4mg/ml and 8mg/ml (Au2, Au4, Au8), lipid, water, the macrophage cell samples and their controls.

- CH: Control (cells only, no AuNP), with human serum.

- NH: Cells with Au nanoparticles, with human serum.
- C-H: Control, without human serum.
- N-H: Cells with Au nanoparticles, without human serum.

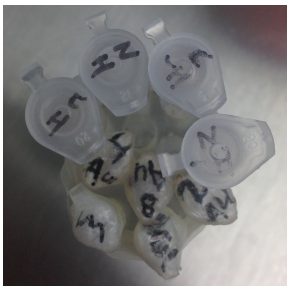

Figure 2.15: Picture of macrophage phantom containing standards for gold, lipid, water, and the macrophage cell samples.

The MARS Spectral scanner was used to scan the phantom, using the FactoryProtocol_Al protocol. This protocol had scan parameters comprising an X-ray tube voltage of 118 kVp, tube current of 13μA, and a 300ms exposure (acquisition) time per frame. The four energy bins were specified as 18.0 – 29.9 keV, 29.9 – 44.9 keV, 44.9 – 74.9 keV, and 74.9 keV - 118.0 keV. This energy range captures the attenuation of gold at the higher energies, representing gold's k-edge at approximately 80.7 keV.

2.6.3 Results and Analysis

The following images were produced by uploading the reconstructed dataset and material information on MARS Vision. Using the Look Up Table (LUT) setting, the minimum threshold of the Au signal was adjusted to 0.002 (equivalent to the lowest concentration of the gold standard in the phantom at 2mg/ml). The Au and second energy bin (29.9 – 44.9 keV) are visible in Figure 2.16b, as the lipid and water channels have been disabled. A strong Au signal can be observed in the pellet containing cells with nanoparticles, without human serum.

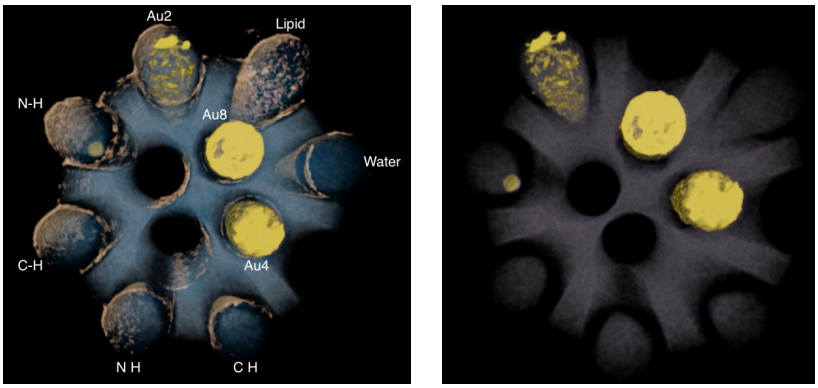

(a) Optimised MD image of the macrophage phantom.

(b) Optimised MD image displaying gold signal only.

Figure 2.16: Optimised MD image of the macrophage phantom. Gold is displayed as yellow, lipid as a pale yellow/beige colour, and water as blue.

Using MARS Vision, the concentration of gold in the pellet was quantified by taking a measurement from an axial, coronal, and sagittal slice using the polygon tool to select the region of interest (recorded in Table 2.3).

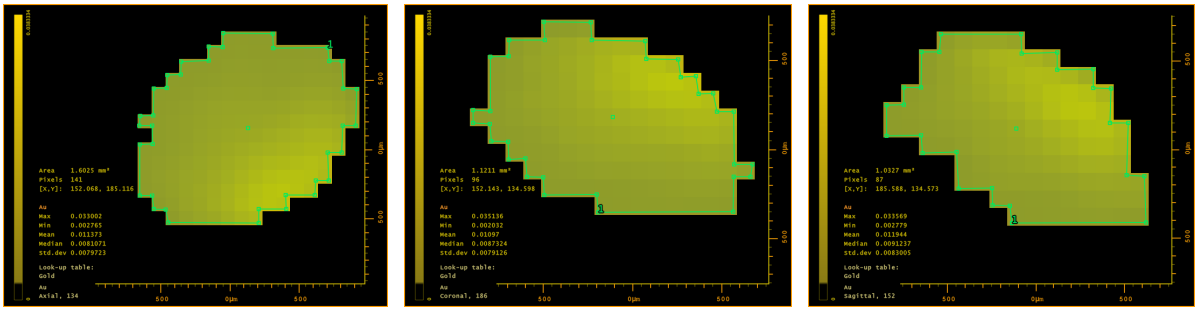

(a) Axial slice. (b) Coronal slice. (c) Sagittal slice.

Figure 2.17: Polygon selections for axial, coronal, and sagittal slice for macrophage sample containing gold nanoparticles without human serum (N-H).

Slice from N-H sample	Mean (mg/ml)	Standard deviation	No. of pixels
Axial	11.3728	7.797227	141
Coronal	10.9698	7.91263	96
Sagittal	11.9442	8.30049	87

Table 2.3: Quantity of gold in macrophages containing Au nanoparticles without human serum, measured in an axial, coronal, and sagittal slice, as seen in Figure 2.17.

The decision to set the minimum threshold of the Au signal to 0.002 is consistent with the percentage of misidentification in the standards of gold. In the following misidentification chart, Au2 has a percentage of correctly identifying gold at 85%, water 15%, and lipid 0.2%. Correct identification for gold above 80% detection for the lowest gold standard concentration instates a confidence for correct material identification, and by setting the minimum threshold at 0.002, eliminates areas identifying as gold, which can be classified as a misidentification.

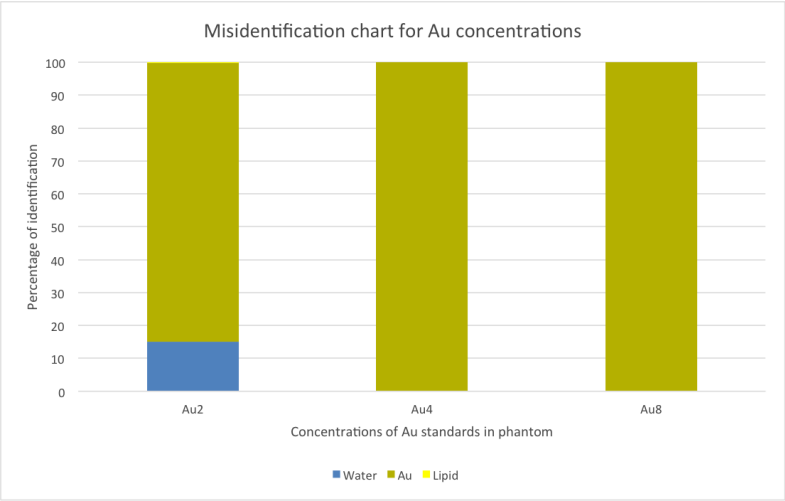

Figure 2.18: Misidentification chart for gold concentrations.

By modifying the Au signal displayed in MARS Vision to coordinate with the gold standards in the phantom, there was a strong signal from the pellet containing cells with nanoparticles without human serum, and no signal from the other three samples. This is observed in the spectral plots, displaying the Hounsfield Units for each material across the four energy bins. Hounsfield Units were used in the spectral plot, so that the linear attenuations were normalized so water and air would yield the same value across the energy bins. Water at standard pressure and temperature is defined as 0 HU, and air is defined to be -1000 HU. The cells containing nanoparticles without human serum exhibit a HU signal between the gold standards Au4 and Au8, whereas the control cells with human serum, and the cells with nanoparticles with human serum demonstrate a signal close to water. The control cells without human serum have a trend following that of lipid.

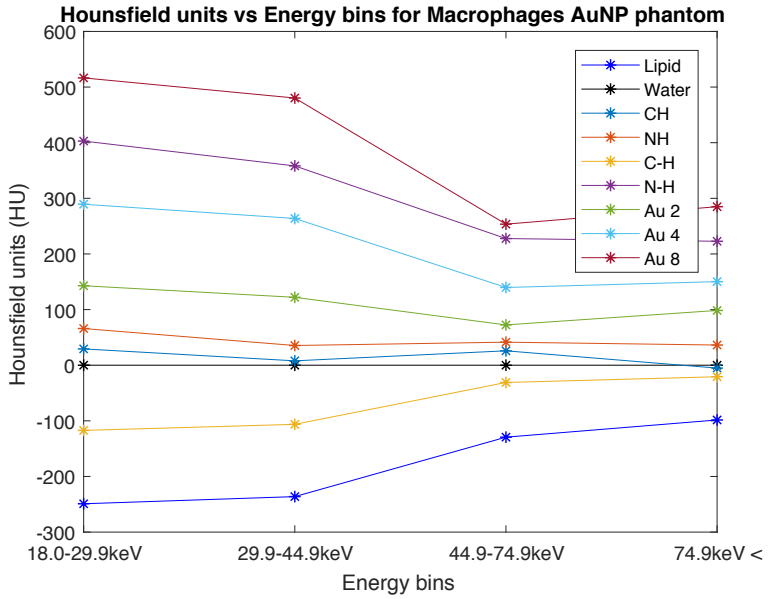

Figure 2.19: Spectral plot for the macrophages gold nanoparticle phantom.

With gold being the primary focus of the macrophage experiment, it is important to select the parameters for the scan that will best accommodate the spectral characteristics of this high Z material. Gold has a k-edge of approximately 80.7 keV [27], and our fourth energy bin is in the range of 74.9 keV - 118.0 keV. To potentially improve this experiment, the range of the fourth energy bin could be increased to better incorporate gold's k-edge, or adding a fifth energy bin to encompass the k-edge fully.

2.6.4 Conclusion

The goal of quantifying the amount of gold in macrophage cell samples was successful in the pellet containing cells with gold nanoparticles, without human serum. In the material decomposition, axial, coronal, and sagittal slices measured a quantity of gold signal in the range of 10-11mg/ml. To optimise this experiment further, optimising the energy bins in the protocol used would incorporate gold's k-edge effectively, potentially improving the analysis of the gold

spectral signal.

2.7 Summary

To summarise the key points of this chapter:

- The governing role of lipoproteins is to transport lipids such as cholesterol and triglycerides around the body in the extracellular fluid, facilitating the availability of fats to cells via receptor-medicated endocytosis.
- Low-density lipoproteins (LDL's) are deemed pro-atherogenic, as oxidized forms invading the endothelium become more easily retained by proteoglycans, hence promoting atherosclerosis progression and vulnerable plaques susceptibility to rupture.
- The use of high-Z material based exogenous contrast agents such as gold and iodine are an essential tool for categorizing soft tissue biomarkers of vulnerable plaque within the human imaging energy range (20 – 120 keV). All atoms have a unique x-ray absorption edge known as a k-edge. Some high atomic materials are within the diagnostic energy range, enabling them to detect and quantify low contrast materials such as lipid.
- The pelleted iodinated and native LDL samples were affected by the chlorine atoms in the trichloroacetic acid (TCA) used for precipitation, which resulted in the misidentification of iodine throughout the PCR tube.
- Pelleted I-LDL and Au-LDL in air at 10mg/ml-precipitated LDL produced a significant signal at concentrations measurable using the MARS Vision software.
- The use of U937 cells resulted in poor uptake of the Au-LDL and I-LDL, as observed by the very minimal colour change of the pelleted cells. This may be due to the uptake mechanisms of LDL, which is a more regulated process compared to the uptake of ox-LDL.
- The macrophage cell sample of the pellet containing cells with nanoparticles without human serum displayed a strong gold signal in the MARS Vision software, with the quantity of AuNPs being successfully measured.

Chapter 3

Iron vs. Calcium

3.1 Overview

The aim of this chapter was to distinguish iron and calcium using spectral CT by optimising a scanning protocol and phantom with iron- and calcium- like materials. The significance of the experiments set out in this chapter includes the long term goal of scanning atheromas to visualise intraplaque haemorrhage and calcifications accurately. The coexistence of iron and calcium in atherosclerotic plaque provides an interesting challenge for imaging modalities, with both materials possessing similar spectral profiles. Iron is an important component of vulnerable plaques due to the feature of intraplaque haemorrhage. Calcium can both prevent and progress plaque vulnerability. Large calcified regions provide plaques with stability, while microcalcifications indicate destabilisation of the atheroma. The ability to distinguish iron and calcium is investigated through multiple phantom studies, with the aim of optimising a phantom suitable for visualising intraplaque haemorrhages and calcifications within vulnerable plaques.

Section 3.2 introduces iron and calcium, and the role they play in vulnerable plaque progression. Previous studies demonstrating the identification of these materials is detailed, along with evidence of their relationship with other components of atheromas. Section 3.3 describes the experiment using large ferric nitrate concentrations, while section 3.4 implements the use of small ferric nitrate concentrations. Section 3.5 attempts to optimise the ferric nitrate phantom (large concentrations) using two different scanning protocols. The ability of iron to have a predominate signal over calcium is investigated in section 3.6, with the blood clot experiment described in section 3.7. A summary of the chapter is given in section 3.8.

3.2 Iron and calcium in atherosclerosis

Intraplaque haemorrhage

The study of iron and calcium is consequential to understanding the mechanisms that support the progression of vulnerable atherosclerotic plaques. Intraplaque haemorrhage is a common

identifying feature of complex lesions leading to acute ischaemic events, which arises from a disruption of thin-walled microvessels, resulting in erythrocytes (red blood cells) leaking into the plaque [28]. Induced is macrophage infiltration and erythrophagocytosis, which prompts intracellular deposits of iron from the erythrocytes haemoglobin content. The leakage of erythrocytes often instigates coagulation, forming a delicate mesh network of fibrin fibers. Thus, the occurrence of intraplaque haemorrhage can be defined by the presence of fresh or lysed erythrocytes, iron deposits in macrophages, and/or a fibrin clot [29].

The relevance of the iron component of intraplaque haemorrhage transpires from the haemoglobin contained in erythrocytes. Haemoglobin is the iron-containing metalloprotein responsible for oxygen and carbon dioxide transport between the lungs and tissues. A haemoglobin molecule consists of four haem groups surrounding a globin group, which consists of two alpha-globin chains and two beta-globin chains. Embedded within the haem compound is an iron ion (charged atom), which is the site of oxygen binding and is gives blood its red colour. Collectively, the four haem groups per haemoglobin molecule can bind four oxygen molecules.

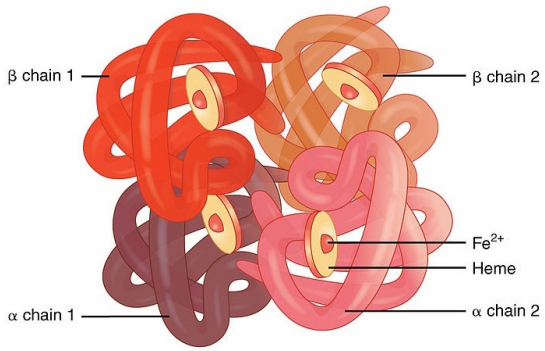

Figure 3.1: Haemoglobin molecule. Accessed from [30].

Iron regulation

Iron is an essential biometal in human physiology, but is potentially hazardous due to the toxicity of free iron ions. For this reason, the vast majority of iron in the body exists in bound form, with effective iron regulation mechanisms to satisfy the metabolic needs of cells. A large part of body iron, approximately 2500mg, is distributed in erythrocyte haemoglobin, while 1000mg is present within ferritin in specific storage tissues such as the liver and spleen. Approximately 170mg is stored in skeletal muscle myoglobin, with 3mg of iron circulating in the transport protein transferrin [31]. Although electron transfer between iron ions is essential for iron transportation, use and storage, it also allows free irons to form highly reactive free radials that can lead to cell damage [32]. Fe^{2+} is involved in iron-induced oxidative stress through the creation of highly reactive hydroxyl radicals, contributing to the formation of insoluble fibrin clots [31]. Fe^{3+} on the hand is rather bio-unavailable due to its poor solubility. As iron readily shuttles between the reduced ferrous (Fe^{2+}) and the oxidised ferric (Fe^{3+}) forms, maintaining successful iron regulation is paramount [33].

Iron is transported around the body bound to transferrin, with each transferrin protein binding two iron atoms. A large part of this iron is taken up by developing erythrocytes within the bone marrow, and incorporated into the production of haemoglobin [32]. Old or damaged erythrocytes are removed from the bloodstream by the macrophages of the reticuloendothelial (RE) system, where the iron is liberated from haemoglobin to be stored in ferritin, the intracellular iron storage protein, or released back into the bloodstream as transferrin-bound iron.

Calcifications

The role calcifications play has shifted in the way atherosclerotic lesions are interpreted. Calcification is a common feature of atherosclerotic plaques, and is easily recognised due to the high resolution of computed tomography. A study evaluating individual plaques revealed an ischaemic event was more likely in plaques that were noncalcified rather than calcified. The new theory suggests that calcium may defend against plaque destabilisation by creating a region of mechanical stability at the interface between calcified and non-calcified plaque [34]. Calcifications may also stabilise plaque by excluding intra-lesion iron that has a higher likelihood of contributing to a thrombotic event [35]. By using three ion-beam techniques to spatially map iron and calcium simultaneously within lesions, Rajendran et al. revealed a spatial inverse correlation, suggesting iron may simultaneously accelerate the progression of atherosclerotic plaques while suppressing calcium. Alternatively, calcification could be a defense mechanism that protects against large accumulations of localised iron.

In the same mindset, more insignificant calcifications that are seemingly harmless may contribute to plaque destabilisation. It is hypothesised that spotty calcification ($>30\mu$m) may be an indication of active remodeling, while microcalcifications (1μm - 30μm) cause plaque instability by promoting stress accumulation within the ECM. Cavitation results due to mismatch between the small, stiff microcalcifications and the surrounding collagen medium [36]. As microcalcifications develop to large macrocalcifications that form beneath the thick fibrous cap, it is suggested that the vascular atherosclerotic plaque increases in stability [37].

Intraplaque haemorrhage association with lipid deposition

Numerous atherosclerosis studies have investigated the relationship between iron and calcium and their association with other materials in vulnerable plaques. Especially apparent is the role intraplaque haemorrhage holds in contributing to local lipid deposition, acting as a source for proinflammatory responses [38]. The leakage of erythrocytes could lead to increased cholesterol deposition and plaque destabilisation. With this knowledge, the cholesterol content in erythrocytes could be a marker for the progression of atherosclerotic plaque and an indicator

of vulnerability [39].

Extravasated erythrocytes constitute the main cellular component of intraplaque haemorrhage [39], and therefore promote cholesterol accumulation and oxidative stress through their makeup of haemoglobin and rich unesterified cholesterol. Erythrocytes lyse quickly within the highly oxidative environment of atherosclerotic plaques, giving haem and iron the ability to modify lipids through oxidation and cause endothelial cytotoxicity [40]. Through this process, haem and iron amplify the oxidative capacity of the plaque and therefore participates in lipid deposition and necrotic core expansion upon intraplaque haemorrhage [41].

Research has also suggested erythrocytes contribute to the additional mechanism of foam cell formation. One study demonstrated haemoglobin, haem oxygenase-1, and iron in the cytoplasm of macrophages around microvessels in specific plaque regions rich in lipid [42]. This indicated microhaemorrhages and subsequent phagocytosis of platelets and erythrocytes. Another study injected erythrocytes into inactive aortic atherosclerotic plaques, which displayed excessive macrophage infiltration [43]. Collectively, these studies suggest that erythrophagocytosis leads to iron deposition within macrophages and macrophage activation, promotion of ceroid production, and accelerated foam cell formation by increasing the capacity of the macrophage to oxidise LDL [44][45].

Interest has been shown in glycophorin A, a characteristic protein of erythrocytes that facilitates anion exchange. Kolodgie et al. demonstrated that the degree of reactivity of glycophorin A and the amount of accumulated iron corresponded to the size of the necrotic core. This was achieved by grading stained specimens based on the percentage of necrotic core or lipid made up of glycophorin A and iron [43]. Colocalisation of glycophorin A and lipid in necrotic cores, paralleled with the increase in the density of macrophages, suggests cholesterol crystals within the plaques could originate from erythrocytes phagocytised by macrophages [39], with intraplaque haemorrhage serving as an inflammatory stimulus.

Quantification of iron in the presence of calcium

The ability to identify and quantify iron from calcium deposits in plaques relies heavily on the ability of the scanner to accurately discern materials. With iron and calcium not having a k-edge within the diagnostic energy range, single-energy x-ray alone cannot distinguish Fe and Ca. At the spatial resolution of interest, conventional CT scanners are limited by partial volume effects due to the large detector pixel size compared with the small haemorrhage deposits seen in human atherosclerotic plaque ($10\mu m^3$ to $100\mu m^3$) [46]. By implementing dual-energy computed tomography and synchrotron-based micro-CT, previous studies have been able to utilise the different x-ray photon energy-dependent attenuation coefficients in an attempt to

distinguish these materials.

The first study employed a clinical dual-energy CT (DECT) scanner to quantify iron in the presence of calcium in an ex vivo porcine arterial plaque model. Mixture solutions of known iron and calcium concentrations were prepared to calibrate the DECT-based algorithm [33]. Iron- and calcium- specific staining was carried out on histological sections to support the co-existence of iron and calcium in the simulated plaques, with a sensitivity of 83% and specificity of 92% demonstrated for iron detection using a threshold at an iron mass fraction of 0.25%. Some voxels of calcium-only plaque gave a positive iron signal, this being attributed to image noise and partial volume effect. The partial volume effect occurs when there is more than one material occupying a CT voxel, resulting in an attenuation coefficient proportional to the average value of these materials. Material boundaries are blurred to some extent due to the resolution limitations of CT, and so a material in any one voxel can affect the attenuation coefficient of surrounding voxels. This may lead to misclassification, as observed for the calcium-only plaque. The iron quantity calculated in plaques with only iron or iron and calcium mixture solutions however was notably higher ($p = 1.21 \times 10^{-4}$) [33].

With the co-existence of iron and calcium deposits in atherosclerotic plaque, finding the point at which there is enough iron present in a voxel that its signal predominates, and predominates over every other signal, has lead to studies quantifying the amount of iron and calcium per voxel, and evaluating the influence of voxel size in distinguishing iron and calcium deposits. For analysis of the spatial distribution of Fe and Ca, Langheinrich et al. used synchrotron-based micro-CT imaging, in addition to a synchrotron-based x-ray fluorescence microscopy, to localise, identify, and quantitate regions of intraplaque haemorrhage and its consequences relating to calcifications [46]. Images at $2\mu m$ voxel resolution of the descending aortic walls revealed local accumulations of punctate bright spots ($\sim 8\mu m$ diameter), corresponding to iron deposits. CT opacities were identified as haemorrhage-related clusters of multiple punctate deposits, containing both Fe (0.48×10^{-12} g/voxel) and Ca (3.18×10^{-2} g/voxel), or isolated accumulations of exclusively calcium. Based on the haemoglobin content of 1 erythrocyte, the iron content of 1 erythrocyte was estimated at 0.24×10^{-12}g [46]. A second study by Langheinrich et al. evaluated the influence voxel size had on discriminating calcium from iron deposits in ex vivo coronary arteries, using clinical CT and synchrotron micro-CT. An advantage micro-CT has over clinical CT is its ability to generate voxels small enough to essentially eliminate the partial volume effect. Using synchrotron micro-CT, images at $4\mu m$ voxel size revealed local accumulations of punctate bright spots, consistent with iron deposits from individual extravascular erythrocytes [10]. The bright spots were spatially separate from calcifications. Iron deposits were visualised using the greyscale values using synchrotron-based micro-CT up to $12\mu m$ voxel size. Images with voxels greater than $20\mu m$ resulted in sufficient blurring of the punctate bright spots [10], as a consequence of the partial volume effect. By virtue of the greyscale values the iron deposits

could not be distinguished from the calcifications.

3.3 Ferric Nitrate experiment (large concentrations)

3.3.1 Aim

The aim of this experiment was to investigate the material decomposition of a phantom containing samples corresponding to iron (ferric nitrate), calcium (hydroxyapatite), and iodine. The MARS spectral scanner currently has difficulty distinguishing iron and calcium, due to the materials similar spectral profiles. Neither material has a k-edge within the energy region of interest for diagnostic imaging, with Fe and Ca having an X-ray absorption edge of 7.11 keV and 4.01 keV, respectively. For this reason, it is hypothesized that the two materials will not be distinguishable. The significance of discriminating these materials would provide the MARS Spectral scanner with the ability to image and visualise iron and calcium simultaneously in atherosclerotic plaques, contributing to the long term goal of scanning patients who are more susceptible to a stroke or myocardial infarction.

3.3.2 Methods

A Biological Sciences PhD student prepared concentrations of ferric nitrate by making up a 1g/ml solution of ferric nitrate in water and then using that stock solution to produce each concentration in individual PCR tubes. The accuracy for the amount of ferric nitrate in each vial was provided from a rough error calculation based on pipetting and weighing out the ferric nitrate at $\sim 3\%$. The five samples prepared for the phantom were at concentrations of 25mg/ml, 50mg/ml, 100mg/ml, 200mg/ml, and 400mg/ml. Included in the phantom were standards for calcium at 104.3 mg HA/cm^3 (HA100), 402.3 mg HA/cm^3 (HA400), and 603.3 mg HA/cm^3 (HA600), standards for iodine at 9mg/ml and 18mg/ml (I9 and I18), lipid and water.

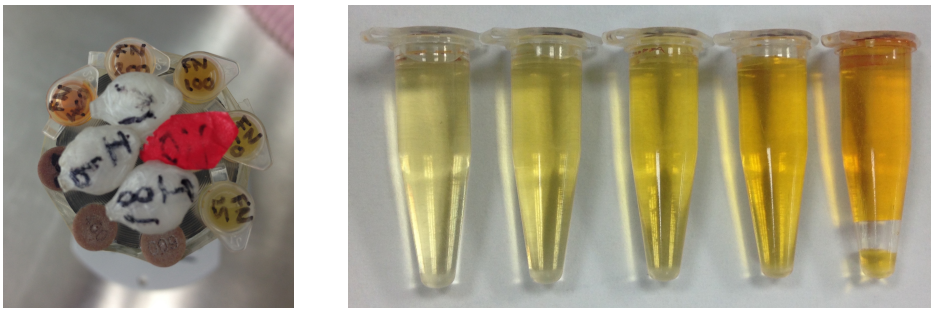

(a) Ferric nitrate phantom using large FN concentrations.

(b) Ferric nitrate samples (large concentrations).

Figure 3.2: Ferric nitrate phantom using large FN concentrations. In (a), a birdseye view of the phantom. In (b), the ferric nitrate concentrations (from left): 25mg/ml, 50mg/ml, 100mg/ml, 200mg/ml, and 400mg/ml.

A new protocol named FerricNitrate_Protocol@80kVp was developed for this scan and future ferric nitrate studies. The scan parameters were defined with a tube voltage of 80kVp, tube current of $55\mu A$, and an exposure time of 100ms. The filtration used was 2mm Al, with four energy bins specified as 20 – 27.9 keV, 27.9 – 35.9 keV, 35.9 – 43.9 keV, and 43.9 - 80.0 keV.

3.3.3 Results and Analysis

The MARS Vision material decomposition revealed indisputable misidentification between the FN400 sample and the standard for HA100. From this observation, further analysis was performed on these two samples, including a review of the materials' linearity and spectral plots, quantified MD analysis, material misidentification charts, and new methods implemented to utilize the energy information from the scan in the hope of demonstrating separation between the two samples in question.

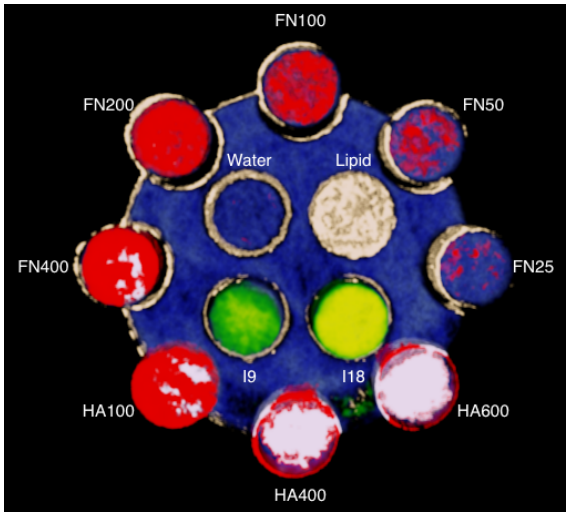

Figure 3.3: Material decomposition ferric nitrate phantom (large concentrations) using MARS Vision. Ferric nitrate signal is red, hydroxyapatite is white, iodine is green, water is blue, and lipid is a cream/beige colour.

Energy image analysis

The following linearity and spectral plots were produced for the ferric nitrate and hydroxyapatite concentrations. The linearity plot shows the linear trend of the four energy bins across the material concentrations. The linear attenuation values for each material concentration were converted in Hounsfield Units (HU) to allow the linear attenuation values to be normalized so water and air would yield the same value across the energy bins, and were separated into their corresponding energy bins. The data points for the four energy bin plots were each accompanied by a linear polynomial fitted to the data using Matlab's inbuilt `polyfit` function. The linearity plots are related to the spectral plots, which show the spectral profiles of the materials by displaying their linear attenuation across the energies. An increase in attenuation at a particular energy on the spectral plot, representing the k-edge of a material, would be expressed as a linear

line displaying this increased HU signal across the material concentrations on the linearity plot.

The spectral plot for the ferric nitrate concentrations revealed an increase in attenuation within the second energy bin, suggesting k-edge absorption of iron in the range 27.9 – 35.9 keV. This spike is depicted by the increased linear trend for the second energy bin in the linearity plot. The k-edge absorption of Fe is 7.11 keV, which contradicts the spectral profile of the ferric nitrate samples observed here. The same circumstance is displayed in the spectral and linearity plots for the hydroxyapatite concentrations. The k-edge absorption of Ca is 4.01 keV, so the spectral plot is expected to have its increased attenuation within the first energy bin in the range 20.0 – 27.9 keV, and then a gradual and continuous decrease in the HU signal across the energies. As a result, the linearity plot reveals an increased linear trend in HU for the second energy bin.

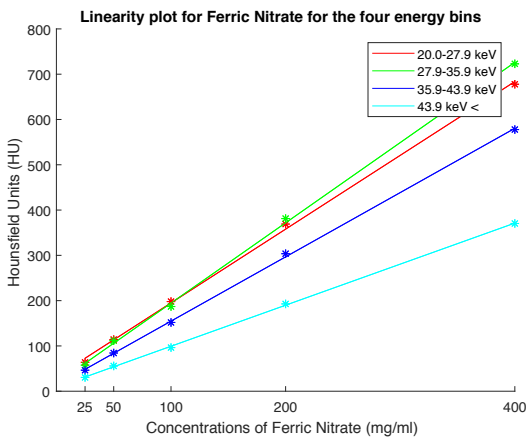

(a) Linearity plot for FN samples in the ferric nitrate phantom.

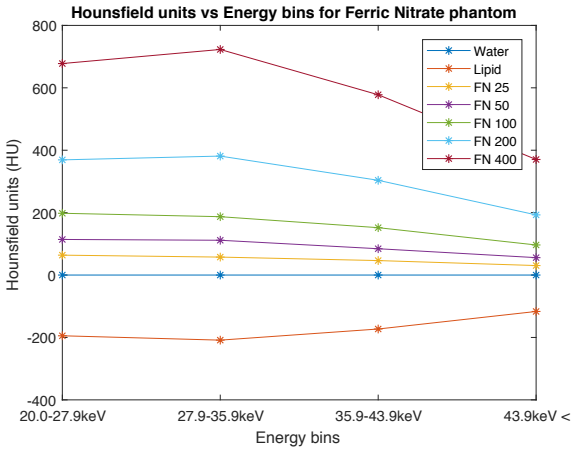

(b) Spectral plot for FN samples in the ferric nitrate phantom.

Figure 3.4: Linearity and spectral plot for the FN samples in the ferric nitrate phantom.

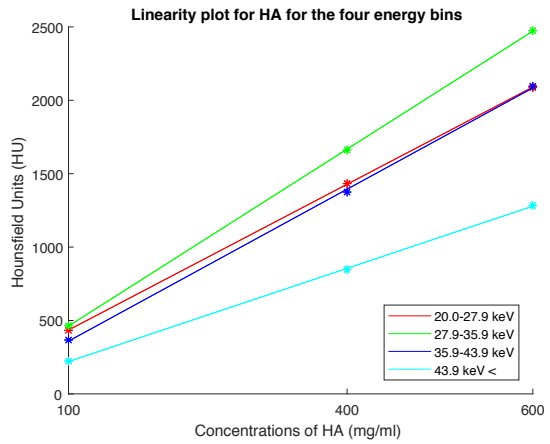

(a) Linearity plot for the HA standards in the ferric nitrate phantom.

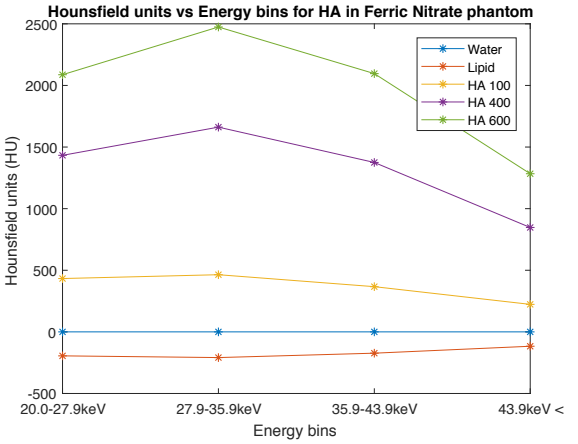

(b) Spectral plot for the HA standards in the ferric nitrate phantom.

Figure 3.5: Linearity and spectral plot for the HA standards in the ferric nitrate phantom.

Interpreting these plots, the issue could be a consequence of the energy intervals used for the energy bins. The intervals are below 10 keV in width, which may lead to low energy photons combining energy and being detected within the higher energy bin. It may also be a calibration issue in relation to the camera, as the MARS scanner underwent maintenance prior to this scan to update the single-chip camera to a three-chip camera.

Material decomposition results

The reconstructed dataset and the material folders generated from the MARS MD were inputted in the MARS Vision software to view the phantom and the material identification. To measure the quantity of material within a sample, a region of interest was created using the polygon tool. The average amount of material measured in the ROI and its standard deviation could be used to compare against the true concentrations of the materials, which are the known variables. For ferric nitrate and hydroxyapatite, these quantified MD results were plotted as shown. Both materials are in close correspondence to the true concentrations, which is represented by the linear line that follows the increase in material concentration for the measured concentrations and the known (given) concentrations. This result supports the calibration of the phantom, with the MD results giving an accurate quantification for the amount of material in the samples.

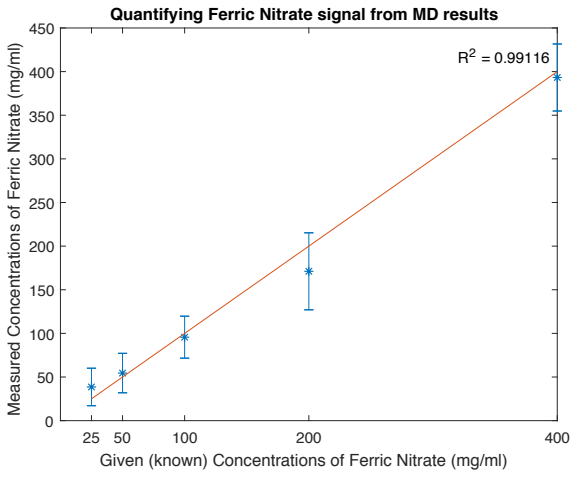

(a) Plot quantifying the ferric nitrate signal from MD results.

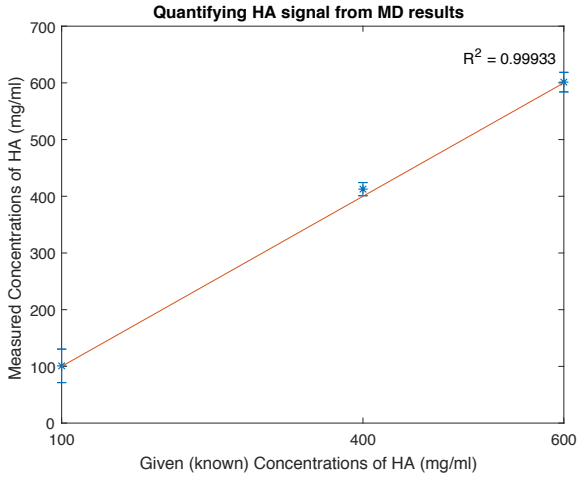

(b) Plot quantifying the hydroxyapatite signal from the MD results.

Figure 3.6: Quantification of the (a) ferric nitrate and (b) hydroxyapatite signal from the MD results. The diagonal line acts as a reference line to represent the linear trend the datapoints should follow for accurate MD quantification.

Misidentification charts were generated to identify what materials were being misclassified in other material samples, and to determine the quantity of this misclassification. If a material at a certain concentration has significant misidentification, the sample cannot be regarded as reliable for correctly identifying the material with accuracy acceptable for the imaging chain. As observed in Figure 3.7a, there is nearly 80% correct identification for the ferric nitrate concentration 100mg/ml. FN200 has correct ferric nitrate identification of $\sim$ 75%. The ferric

nitrate concentrations FN25 and FN50 exhibit less correct identification due to their reduced concentration and thus their susceptibility for other materials in the phantom to overwhelm the ferric nitrate sample with their signal. Also observed is a significant HA signal in the FN400 sample. The misidentification chart for the hydroxyapatite concentrations in Figure 3.7b shows an immense misclassification of ferric nitrate in the HA100 sample, with the ferric nitrate signal predominant over the hydroxyapatite signal. HA400 and HA600 have correct percentage identification of $\sim 93\%$ and $\sim 100\%$, respectively. From Figure 3.3 displaying the MD image, the misidentification established in these charts directly relates to the optimized MD image and the mismatch of colours seen across the various samples.

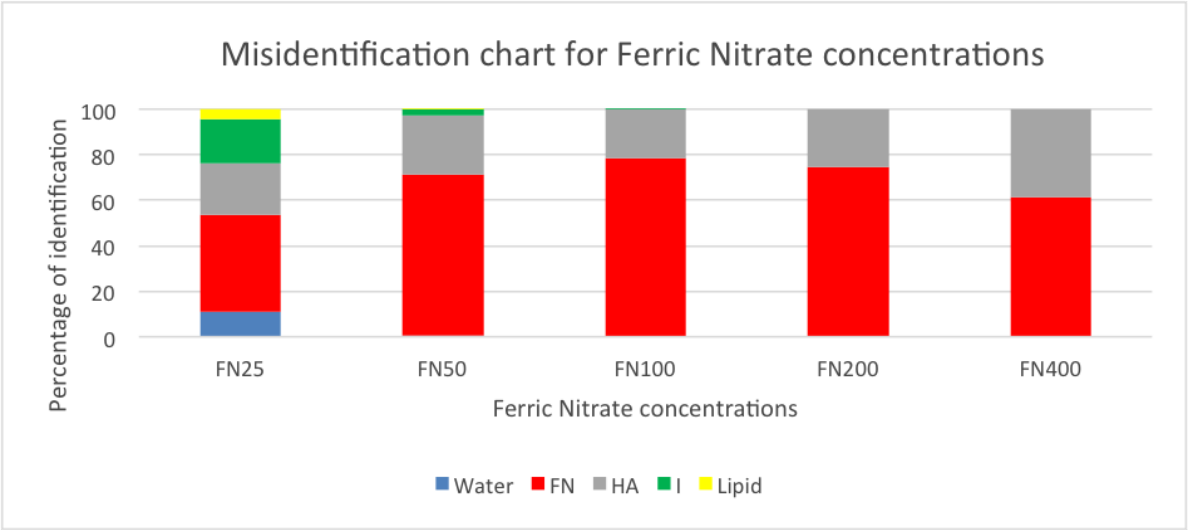

(a) Misidentification chart for the ferric nitrate concentrations in the ferric nitrate phantom.

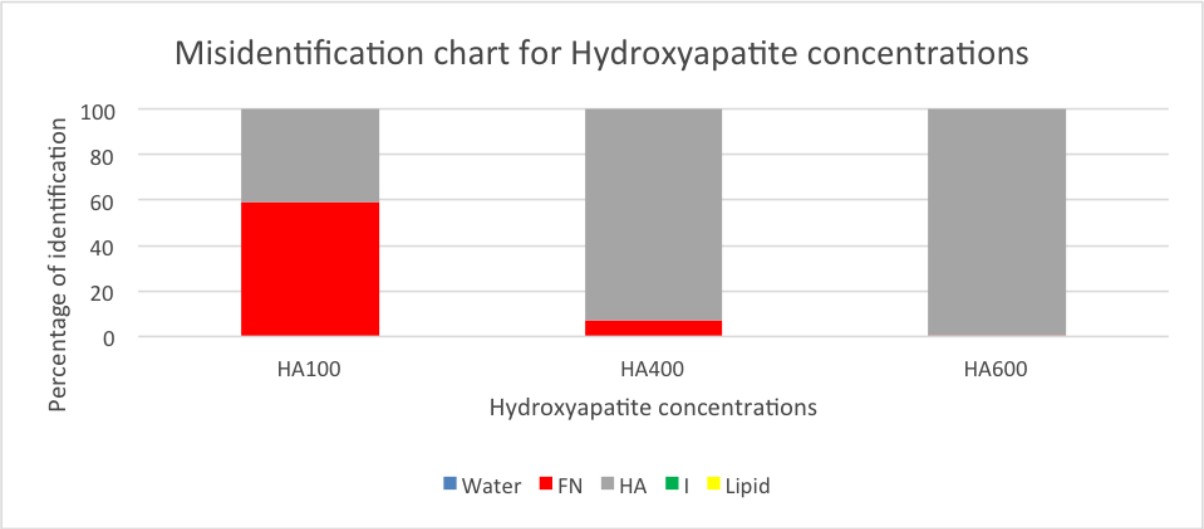

(b) Misidentification chart for the hydroxyapatite concentrations in the ferric nitrate phantom.

Figure 3.7: Misidentification charts for ferric nitrate (a) and hydroxyapatite (b) concentrations in the phantom.

New methods

The outcome of the ferric nitrate MD image from the visible misidentification between FN400 and HA100 instigated the implementation of new methods to assist in distinguishing these two samples. By using the spectral information from the attenuation coefficients measured from each energy bin, exploitation of the x-ray photons attenuation at different x-ray energies can allow materials to be differentiated through their differing spectral profiles. The new methods implemented were as follows:

- Histogram method
- ROC curves
- Percentage Correct (PC)
- Scatter plots with marginal histograms

Histogram method

Image processing was completed using ImageJ, which involved taking the average intensity across ten slices and selecting a ROI for FN400 and HA100. The coordinates of the ROI, and the associated attenuation coefficient of each pixel included within the ROI, were saved using the ImageJ commands Analyze – Tools – Save XY Coordinates. This was done for each energy image in ImageJ. By saving the coordinate information of the ROI in an excel spreadsheet for each material at each energy, and importing the data for both materials into Maltab, histograms comparing the attenuation coefficients of FN400 and HA100 across the four energy bins were generated. These are accompanied by corresponding ROC curves below.

ROC curves

A receiver operating characteristic curve, abbreviated to ROC curve, is a graphical plot that is a fundamental tool for diagnostic test evaluation. The four possible outcomes of a diagnostic test include:

- True positive = correctly identified
- False positive = incorrectly identified
- True negative = correctly rejected
- False negative = incorrectly rejected

To define the statistical measures of sensitivity and specificity that incorporates these possible outcomes:

- Sensitivity measures the proportion of true positives that are correctly identified as such by the test.

$$Sensitivity = \frac{\text{no. of true positives}}{\text{no. of true positives + no. of false negatives}}$$

- Specificity measures the proportion of true negatives that are correctly identified as such by the test.

$$Specificity = \frac{\text{no. of true negatives}}{\text{no. of true negatives + no. of false positives}}$$

The ROC curve is created by plotting the true positive rate (sensitivity) against the false positive rate (1-specificity) at various threshold settings across a diagnostic test. It is named as such because it is a comparison of two operating characteristics (the true positive rate and false positive rate) as the criterion changes. Each point on the ROC curve represents a sensitivity/specificity pair that corresponds to a particular decision threshold. As the threshold moves along the dataset for the first and second material, the sensitivity/specificity pairings are calculated and plotted against the two operating characteristics. The area under the ROC curve (AUC) determines how well a parameter can distinguish the two datasets. An area of 1 represents perfect discrimination, where there is no overlap in the two distributions of the datasets. This is depicted by the ROC curve passing through the upper left corner of the ROC space (100% sensitivity, 100% specificity). An area of 0.5 represents a worthless test, where there is complete overlap between the two distributions, leading to no suggestion of discrimination being observable. This is illustrated by the ROC curve making a 45-degree diagonal across the ROC space. Hence, the closer the curve traces the left hand border and the top border of the ROC space, the more accurate the test.

With the ROI datasets for FN400 and HA100 for the four energy bins imported into Matlab, the histograms and corresponding ROC curves were generated.

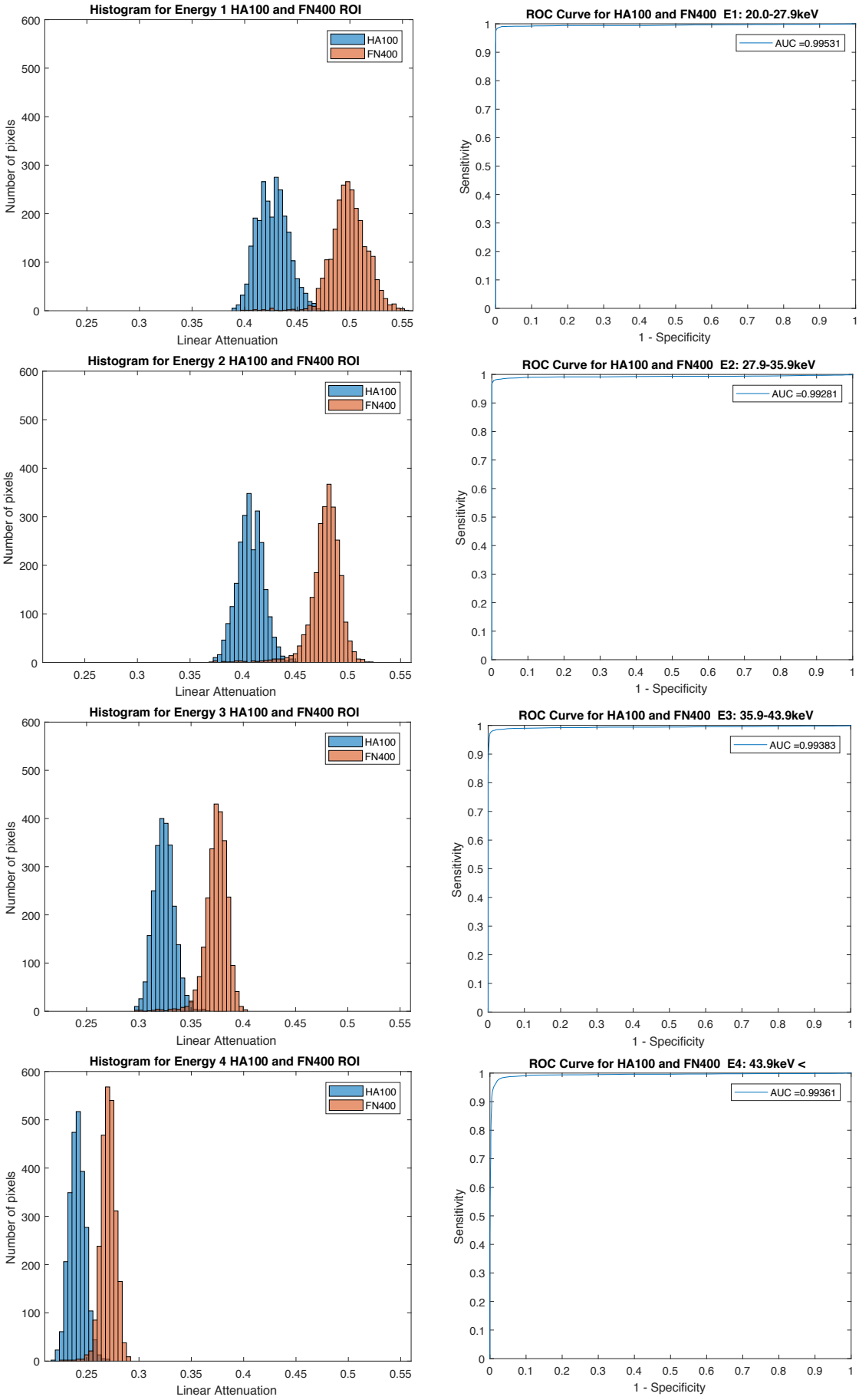

Figure 3.8: Histogram plots comparing HA100 and FN400 for the four energy bins. These are accompanied by corresponding ROC curves for each energy bin. See section 3.3.3 for an explanation of histogram plots and ROC curves.

The histogram plots and corresponding ROC curves for HA100 and FN400 show clear distinction between the material's linear attenuation values across the four energy bins. The ROC curves have an Area Under the Curve approximately equal to 1, demonstrating complete separation of HA100 and FN400 using the histogram method.

Percentage Correct (PC)

To further support the discrimination of the FN400 and HA100 datasets, the percentage of correct identification was calculated. This was achieved by taking a number of trials; in this case the number of trials was equivalent to the number of pixels with the ROI dataset at 2472 pixels. Knowing that the HA100 sample has lower attenuation values compared to FN400 in the histogram plots, the trials ran through datasets, comparing a random value from the HA100 dataset and FN400 dataset. If the selected value from HA100 was smaller then the FN400 value, a count was added to an empty array collecting all the instances of correct localization of the pixels attenuation. For the four energy bins, the following PC values were calculated. These values directly relate to the discrimination observed in the histograms and corresponding ROC curves.

	E1	**E2**	**E3**	**E4**
Percentage Correct	0.9972	0.9956	0.9915	0.9968

Table 3.1: Calculated PC values for the four energy bins.

Scatter plots with marginal histograms

Scatterplots were generated to visualize the relationship of the attenuation coefficients between the energies. By comparing Energy bin 1 vs. Energy bin 2, Energy bin 2 vs. Energy bin 3, and Energy bin 3 vs. Energy bin 4, a positive correlation is observed for the energies. Included in these scatterplots are the marginal distributions of the energy bin on the x-axis and energy bin on the y-axis as univariate histograms.

3.3.4 Conclusion

The material decomposition in Figure 3.3 revealed misclassification between FN400 and HA100. By implementing new methods for analysis, such as the histogram method (which is basically 'visual PCA' - see chapter 4), ROC curves, PC, and scatter plots, the energy information from the attenuation coefficients of FN400 and HA100 enabled the two material concentrations to be separated. In the ferric nitrate samples 25mg/ml - 200mg/ml, a clear FN signal is observed, with HA400 and HA600 showing a strong HA signal. The success of this experiment lead to further ferric nitrate phantom experiments, trialing different concentrations of ferric nitrate and hydroxyapatite in order to optimise the phantom for continued use in future phantom studies.

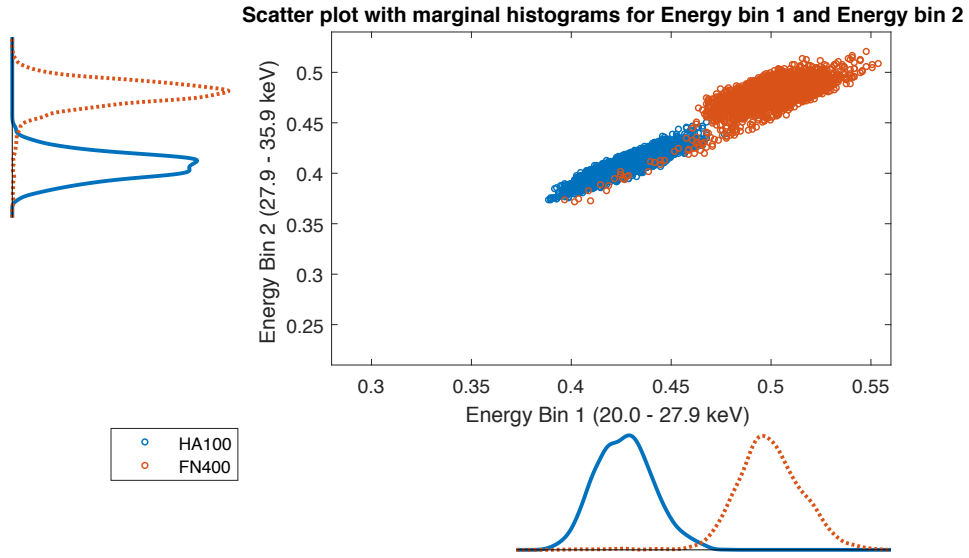

(a) Scatter plot comparing Energy 1 and Energy 2 attenuation coefficients.

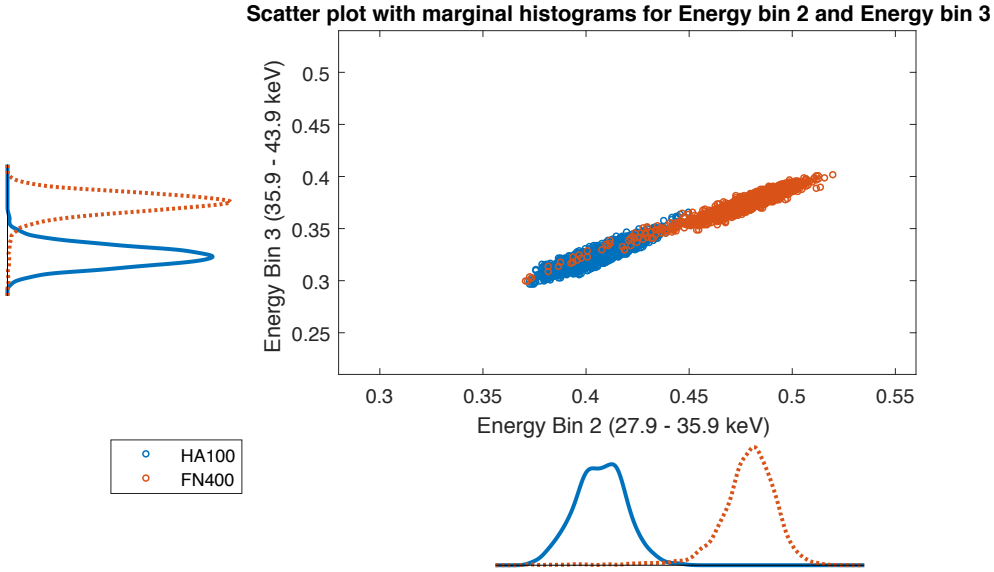

(b) Scatter plot comparing Energy 2 and Energy 3 attenuation coefficients.

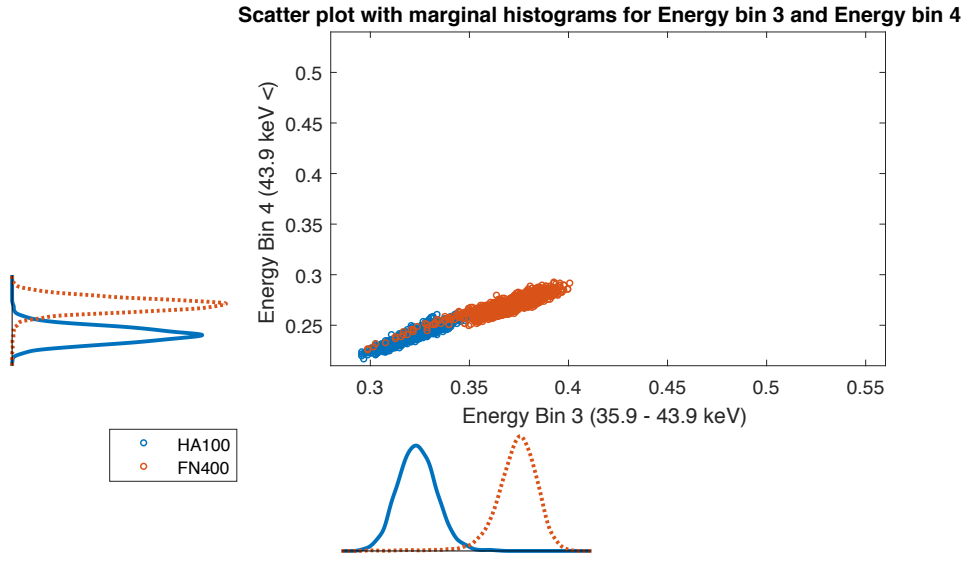

(c) Scatter plot comparing Energy 3 and Energy 4 attenuation coefficients.

Figure 3.9: Scatter plots with marginal histograms for E1 vs. E2, E2 vs. E3, and E3 vs. E4. See an explanation on the previous page in section 3.3.3.

3.4 Ferric Nitrate experiment (small concentrations)

3.4.1 Aim

The aim of this experiment was to investigate the material decomposition of a phantom containing samples of ferric nitrate to represent iron, and standards of hydroxyapatite to represent calcium. This experiment employed small ferric nitrate concentrations compared to the experiment in Section 3.3. The significance of this is to use concentrations that more closely represent concentrations of iron found in the human body. The small concentrations will test the MARS scanner resolution and ability to accurately detect such low concentrations.

3.4.2 Methods

Following the results from the first experiment, smaller ferric nitrate concentrations were produced using the same methodology as in Section 3.3.2. Six samples were prepared at concentrations of 1mg/ml, 2mg/ml, 4mg/ml, 6mg/ml, 8mg/ml, and 10mg/ml, with the intent of more closely representing anatomically relevant concentrations of blood in the body. The phantom included standards for calcium at 104.3mg HA/cm^3 (HA100), 211.7mg HA/cm^3 (HA200), 402.3mg HA/cm^3 (HA400), and 603.3mg HA/cm^3 (HA600), lipid and water.

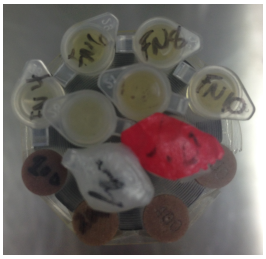

(a) Ferric nitrate phantom using small FN concentrations.

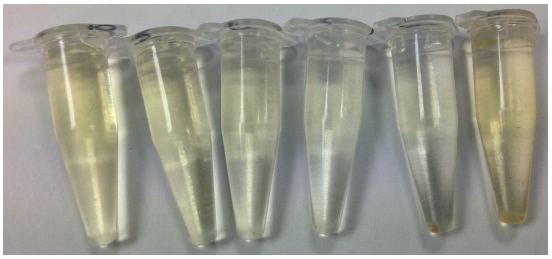

(b) Ferric nitrate samples (small concentrations).

Figure 3.10: Ferric nitrate phantom using small FN concentrations. In (a), a birdseye view of the phantom. In (b), the ferric nitrate concentrations (from left): 10mg/ml, 8mg/ml, 6mg/ml, 4mg/ml, 2mg/ml, and 1mg/ml.

The scan was run twice, first with the FerricNitrate_Protocol@80kVp protocol and then with the UOC_Protocol_Aluminium protocol, which is implemented in Chapter 6 for plaque scanning. The purpose of scanning using both protocols was to attempt to merge the two together, in a way that would allow future iron studies for intraplaque haemorrhage and calcium deposits in plaque specimens to be investigated.

The FerricNitrate_Protocol@80kVp protocol had equivalent scan parameters as in Section 3.3, although the four energy bins were specified in 10 keV intervals, at 20.0 – 30.2 keV, 30.2 – 40.1 keV, 40.1 – 49.8 keV, and 49.8 keV - 80.0 keV. This was especially important for the first energy bin, to resolve the issue with the spectral plot of HA showing an increase in attenuation at the second energy bin. The UOC_Protocol_Aluminium protocol had scan parameters including

a tube voltage of 118 kVp, tube current of $23\mu A$, exposure time of 100ms, and a 2mm Al filtration. The four energy bins were in the range 30.0 – 39.9 keV, 39.9 – 50.0 keV, 50.0 – 60.0 keV, and 60.0 keV - 118.0 keV.

3.4.3 Results and Analysis

The reconstructed datasets for both protocol scans were loaded from MARS Transfer, and image processing was completed to produced rescaled, 32-bit images. The attenuation coefficients were recorded for each sample in the phantom by taking the average intensity over 10 slices. The 10 slices chosen for measurement were identical for both protocol scans. These values were inputted into Matlab code to calculate the bases, which were then saved to a config file and used to run the material decomposition with the reconstructed datasets. The FerricNitrate_Protocol@80kVp protocol MD ran successfully, however the MD for the UOC_Protocol_Aluminium protocol had issues relating to its bases calculation. When the material bases were calculated, the ferric nitrate bases for energy bin 2 (39.9 - 50.0 keV) and energy bin 3 (50.0 - 60.0 keV) were zero, and when the linear attenuation values were converted to Hounsfield Units, all the HU were negative values, indicating that the ferric nitrate signal was presenting less than that of water (HU = 0). Although the MD ran successfully for the UOC_Protocol_Aluminium protocol, the results from the MD were unproductive and did not display ferric nitrate signal in the FN samples. Consequently, the following analysis is only from the ferric nitrate phantom run with the FerricNitrate_Protocol@80kVp protocol.

The following MD image was produced in MARS Vision. The minimum threshold of hydroxyapatite in the LUT setting was selected as 0.05 to coincide with correct material identification of HA at $\sim 80\%$ for HA50. By doing this, any HA signal <50mg/ml showing up elsewhere in the phantom was eliminated, as it could be considered a misidentification.

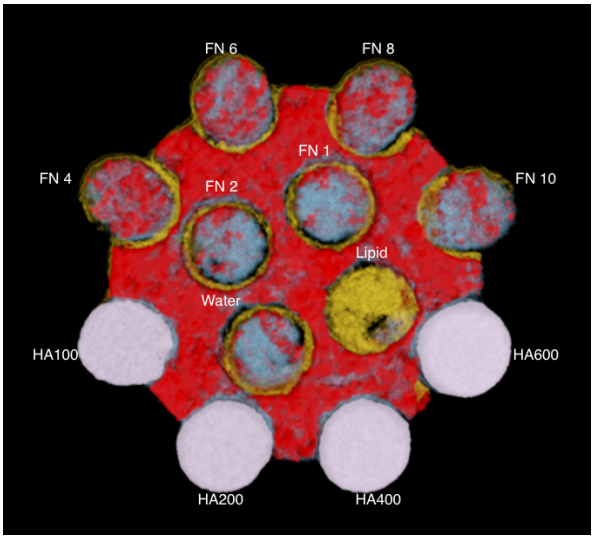

Figure 3.11: Material decomposition ferric nitrate phantom (small concentrations) using MARS Vision. Ferric nitrate signal is red, hydroxyapatite is white, water is blue, and lipid is yellow.

Energy image analysis

The following linearity and spectral plots were produced for the ferric nitrate and hydroxyapatite concentrations from the FerricNitrate_Protocol@80kVp protocol scan. It is observed that the ferric nitrate concentrations (1mg/ml - 8mg/ml) show a spectral profile similar to water, with FN10 having HU signal above water for all energy bins. The linearity plot is disorderly, with the datapoints measuring HU across the concentrations for each energy not being consistent with the linear polynomial fitted to the data. Another observation is the increased HU signal for the ferric nitrate concentrations in energy bin 4 (49.8 - 80.0 keV). The k-edge of Fe = 7.11 keV, so an increased HU signal should be observed in the first energy bin (20.0 - 30.2keV), with a gradual but continuous decrease in this signal across the other energy ranges. It is still observed in the HA spectral plot the increase in attenuation within the second energy bin. This should be expressed in the first energy bin to represent the calcium k-edge at 4.01 keV.

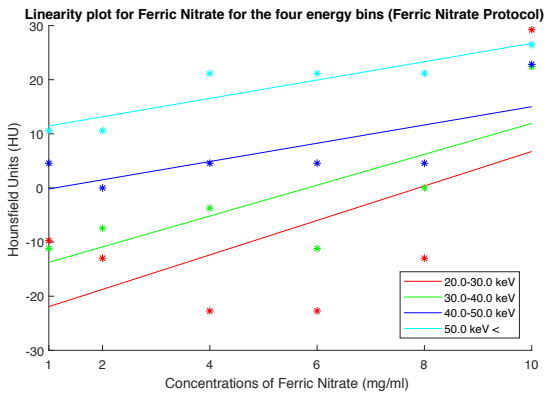

(a) Linearity plot for FN samples in the ferric nitrate phantom (small concentrations).

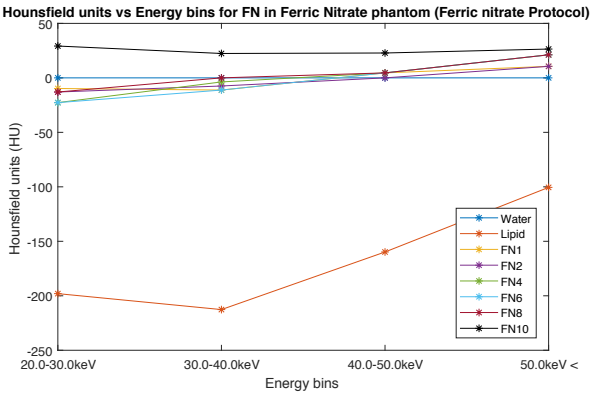

(b) Spectral plot for FN samples in the ferric nitrate phantom (small concentrations).

Figure 3.12: Linearity and spectral plot for the FN samples in the ferric nitrate phantom (small concentrations).

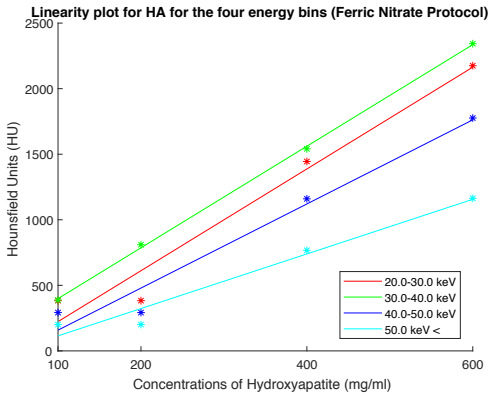

(a) Linearity plot for the HA standards in the ferric nitrate phantom (small concentrations).

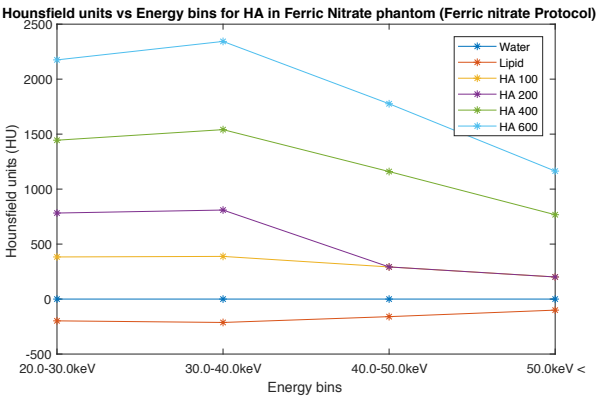

(b) Spectral plot for the HA standards in the ferric nitrate phantom (small concentrations).

Figure 3.13: Linearity and spectral plot for the HA standards in the ferric nitrate phantom (small concentrations).

Material decomposition results

To establish the quantity of material within the ferric nitrate and hydroxyapatite samples, measurements of the average quantity and its standard deviation were taken from a ROI for each sample. The measurements were compared to the true material concentrations in the following plots.

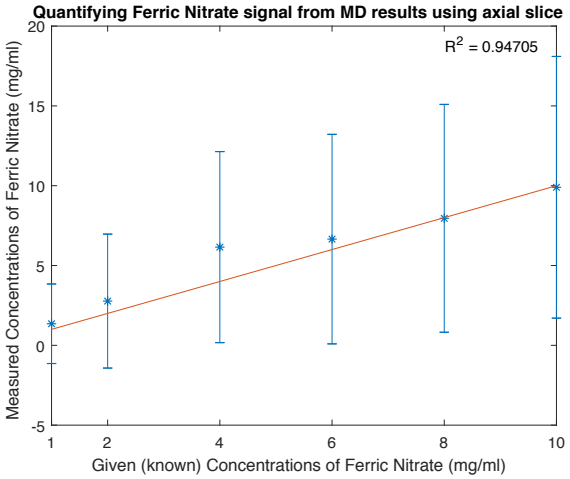

(a) Plot quantifying the ferric nitrate signal from MD results.

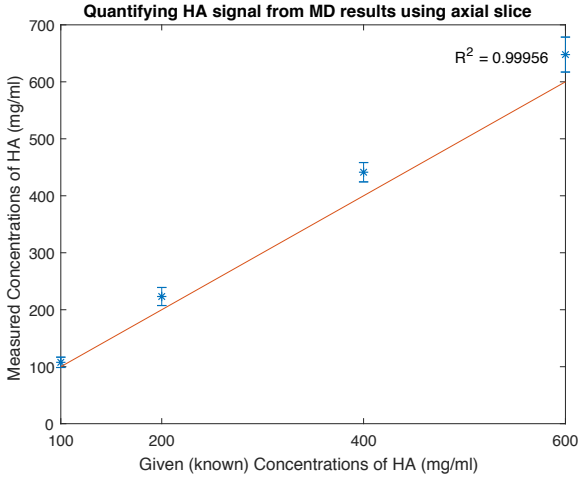

(b) Plot quantifying the hydroxyapatite signal from the MD results.

Figure 3.14: Quantification of the (a) ferric nitrate and (b) hydroxyapatite signal from the MD results. The diagonal line acts as a reference line to represent the linear trend the datapoints should follow for accurate MD quantification.

The errorbars spanning each ferric nitrate concentration show large deviation from the measured quantified values. The small concentrations used indicate a large error associated with MARS Visions' capability to accurately calculate the correct quantification of each sample. The quantification of the hydroxyapatite standards follows closely to the linear reference line for accurate MD quantification, with small associated deviations. This is because the hydroxyapatite standards are a factory manufactured product made specifically for calibration purposes.

Misidentification charts were produced to indicate what materials were being identified in other material samples, and to determine the percentage of misidentification. In Figure 3.15a, there is significant misidentification from HA, lipid and water across all ferric nitrate samples. The highest ferric nitrate identification comes from FN4, however, this identification is only $\sim 50\%$. In contrast, the hydroxyapatite samples possess 100% correct identification across all concentrations (Figure 3.15b). In comparison to the first ferric nitrate experiment in Section 3.3, four HA standards were used in this phantom, rather than three. This may have helped the 100% HA identification, together with the lower FN concentrations not having a similar spectral signal as the HA concentrations. The misidentification charts measure the signal from each material within the material samples without any preset threshold on the minimum or maximum concentration, unlike the MD image, which has a minimum threshold set for ferric

nitrate and hydroxyapatite to eliminate any small concentrations which can be classified as a misidentification. Therefore, the misidentification charts are showing the complete signal response for materials in the MD.

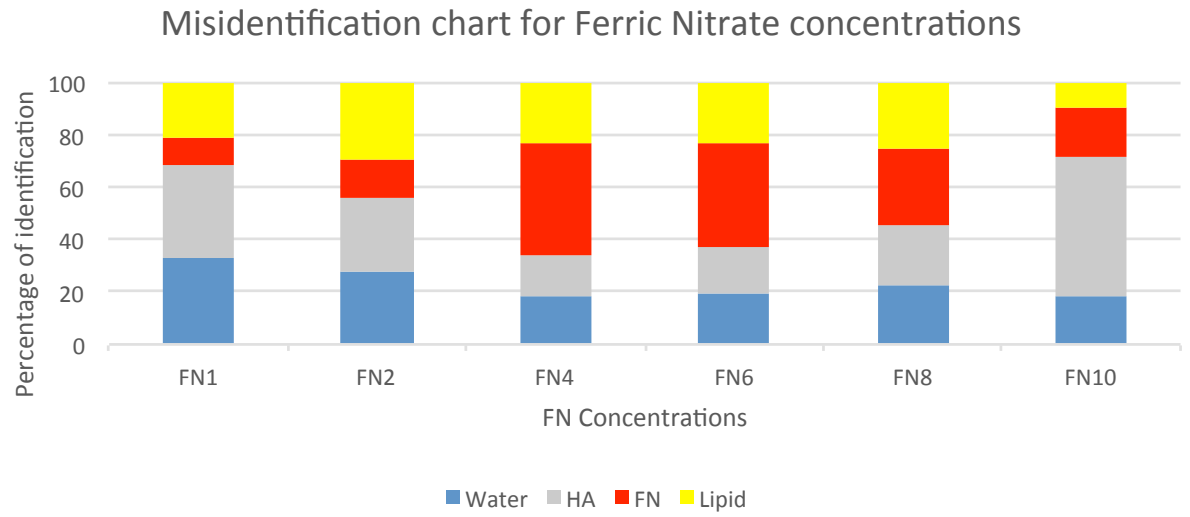

(a) Misidentification chart for the ferric nitrate concentrations in the ferric nitrate phantom (small concentrations).

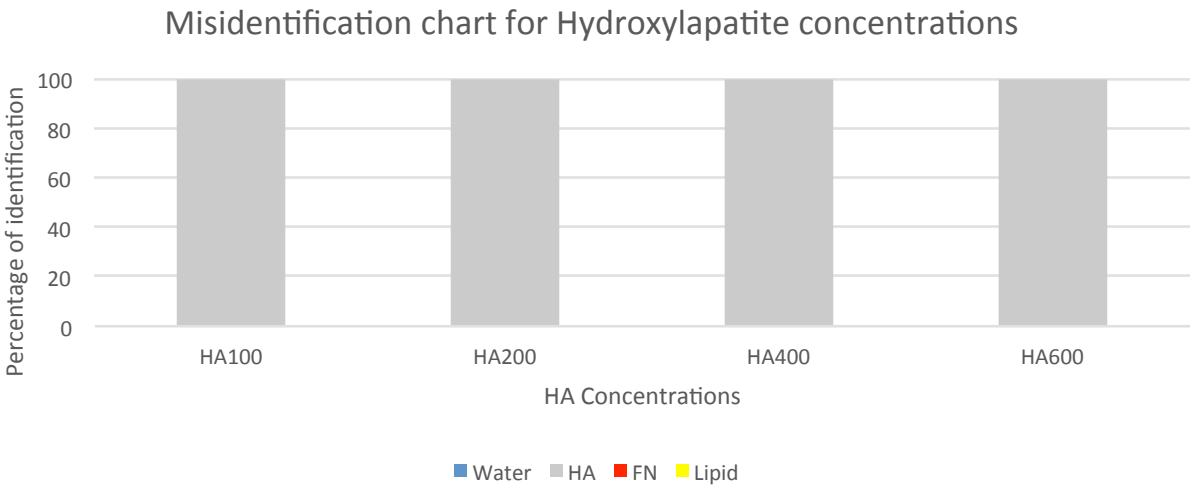

(b) Misidentification chart for the hydroxyapatite concentrations in the ferric nitrate phantom (small concentrations).

Figure 3.15: Misidentification charts for (a) ferric nitrate and (b) hydroxyapatite concentrations in the phantom.

3.4.4 Conclusion

There is no obvious misidentification between specific hydroxyapatite standards and the ferric nitrate samples using the normal MARS MD (as seen in Figure 3.11), so the new methods were not implemented in the analysis. Even so, the small ferric nitrate concentrations could not be sufficiently identified with the MARS Vision material decomposition as containing ferric nitrate. This is evident in the misidentification charts in Figure 3.15a, where the FN signal across all ferric nitrate concentrations is <50%. On account of this, the large ferric nitrate concentrations were reverted back to for further scans.

3.5 Ferric Nitrate experiment (large concentrations with two protocols)

3.5.1 Aim

The aim of this experiment was to investigate the material decomposition of a phantom containing samples of ferric nitrate to represent iron, and standards of hydroxyapatite to represent calcium. The large FN concentrations were employed again, based on the results of the small concentrations in Section 3.4. This experiment was completed using two protocols: one which is specifically used for plaque scans, and the other being the protocol implemented in the ferric nitrate experiments. This was performed with the goal of combining the protocols by some means for investigating intraplaque haemorrhage in future vulnerable plaque scans. The significance is that success with this work would allow development of a protocol for imaging plaque samples for intraplaque haemorrhage.

3.5.2 Methods

Using both the FerricNitrate_Protocol@80kVp and UOC_Protocol_Aluminium protocols, the scans were run with their respective scan parameters. The phantom contained the ferric nitrate concentrations 10mg/ml, 25mg/ml, 50mg/ml, 100mg/ml, 200mg/ml and 400mg/ml. The HA concentrations used were HA100, HA200, HA400, and HA600. Also included were lipid and water.

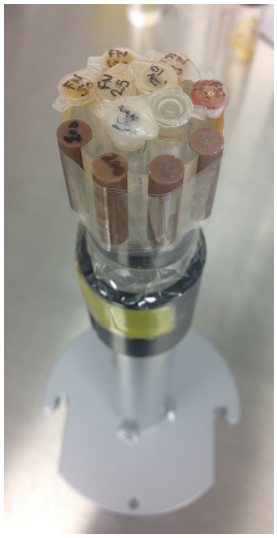

Figure 3.16: Ferric nitrate phantom using large FN concentrations.

In a previous unsuccessful scan replicating this experiment, the phantom instead contained HA concentrations of HA50, HA100, HA200, and HA400. When the datasets were downloaded and processed to run the MD, an error message appeared stating 'Poorly formed basis vectors!' This was because the angle of separation between two materials spectral profiles was too simi-

lar, and hence the separation of the basis vectors between materials was too small for the MD software to distinguish them. HA600 was not used in the phantom in this instance, which may have given rise to the failure of the MD. HA600 has a high attenuation associated with it, and in the energy images appears as a bright white signal. As a consequence of HA600 not being present in the phantom, the energy images lacked this large attenuating concentrated material, and thus showed little variation in the greyscale. This alone can give one reason to anticipate difficulty separating the basis vectors and issues running the MD.

Initiating the MD was successful for the scan using the FerricNitrate_Protocol@80kVp protocol, but the same error message was generated for the scan using the UOC_Protocol_Aluminium protocol. Attempts to manipulate the data, by recalculating the attenuation coefficients and/or ignoring a material concentration in the basis calculation did not resolve the issue, with the basis vectors still not well defined for the system to distinguish materials. As a result, the following results are only from the scan using the FerricNitrate_Protocol@80kVp protocol.

3.5.3 Results and Analysis

The same image processing was completed as in previous experiments, and by setting LUT thresholds for the materials the following optimised MD image was produced in MARS Vision.

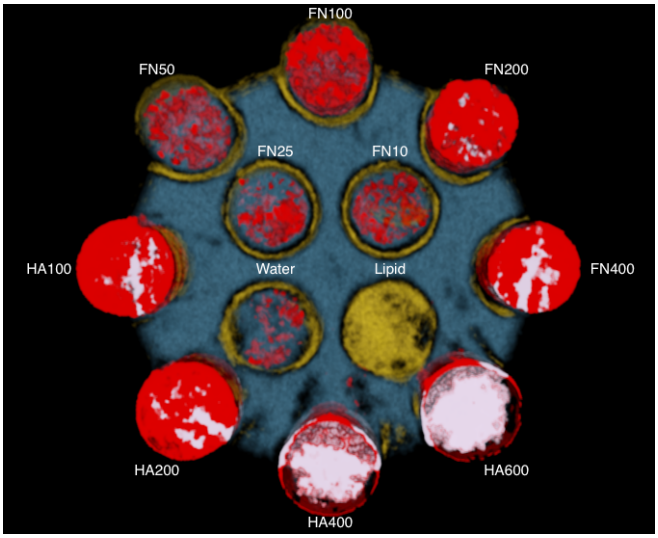

Figure 3.17: Material decomposition of the ferric nitrate phantom on MARS Vision using large FN concentrations. Ferric nitrate signal is red, hydroxyapatite is white, water is blue, and lipid is yellow.

Energy image analysis

Linearity and spectral plots were produced for the ferric nitrate and hydroxyapatite concentrations from the FerricNitrate_Protocol@80kVp protocol scan. Noteworthy is the similar Hounsfield Unit signal in the spectral plots for the ferric nitrate samples FN200 and FN400, and the hydroxyapatite samples HA100 and HA200. Consequently, there is evident misidentification

in the optimised MD image between these samples, as seen in Figure 3.17. Both spectral plots for FN and HA observe an increase in attenuation within the second energy bin, which does not accord with the absorption edges of Fe and Ca that should occur within the first energy bin.

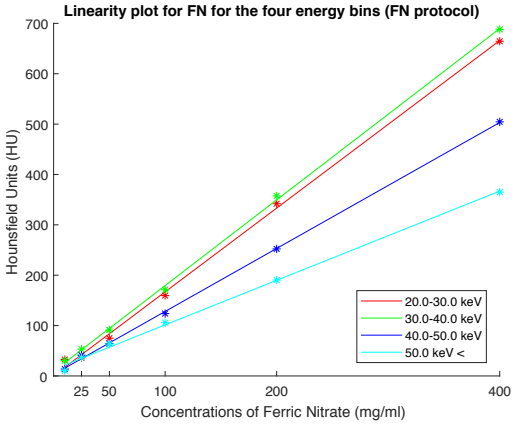

(a) Linearity plot for FN samples in the ferric nitrate phantom.

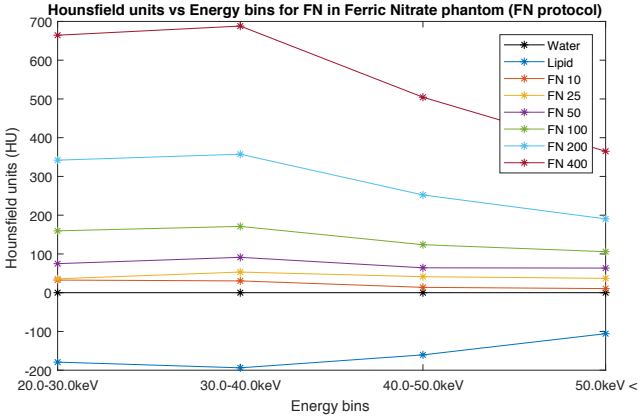

(b) Spectral plot for FN samples in the ferric nitrate phantom.

Figure 3.18: Linearity and spectral plot for the FN samples in the ferric nitrate phantom using the large FN concentrations.

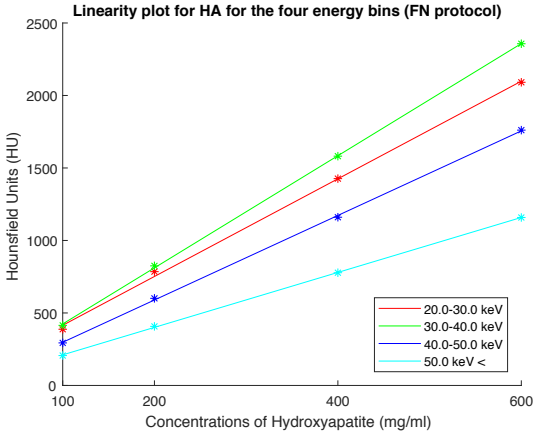

(a) Linearity plot for HA samples in the ferric nitrate phantom.

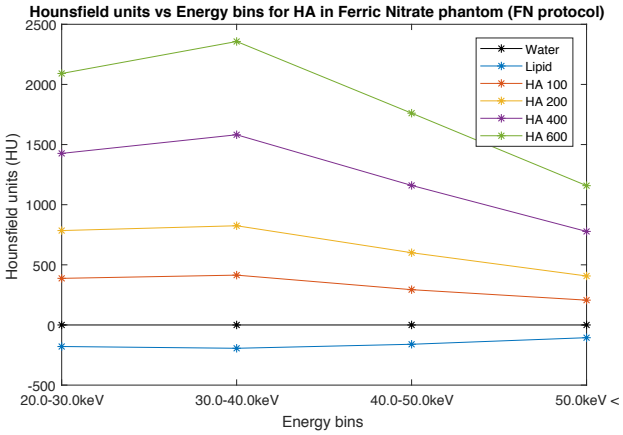

(b) Spectral plot for HA samples in the ferric nitrate phantom.

Figure 3.19: Linearity and spectral plot for the HA samples in the ferric nitrate phantom using the large FN concentrations.

Material decomposition results

Quantifying the ferric nitrate and hydroxyapatite signal measureable in MARS Vision revealed concentration measurements that were significantly lower than the given (known) concentrations. This is seen in the drop in the datapoint denoting the measured quantity, compared to the reference line representing the slope of perfect quantification of the material concentrations (Figure 3.20). When this analysis was carried out, this issue was noted and other datasets were tested to evaluate their measured quantification of the samples. These too had notable underestimations of the measured values. It was determined to be a calibration issue, with the

MARS scanner undergoing tests to resolve the under reading of material concentrations.

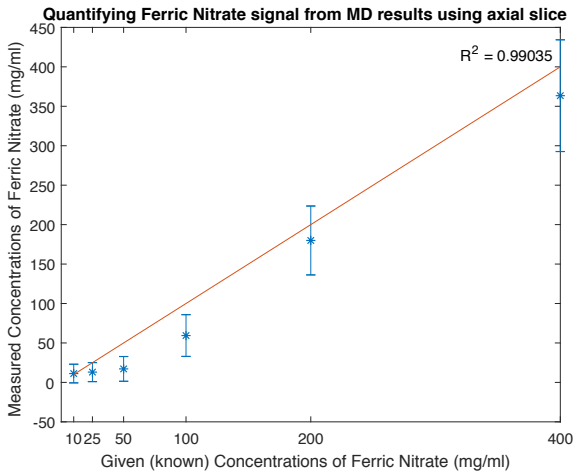

(a) Plot quantifying the ferric nitrate signal from MD results.

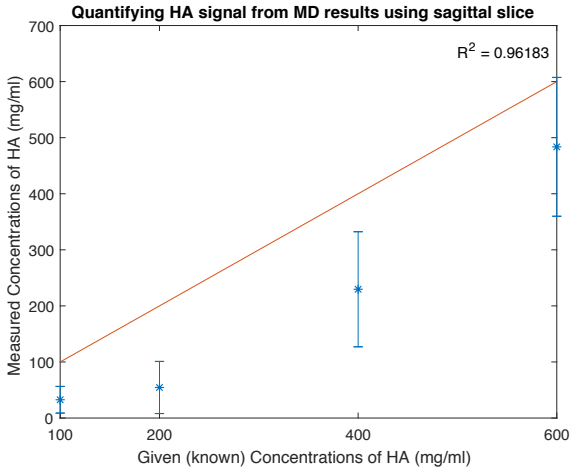

(b) Plot quantifying the hydroxyapatite signal from the MD results.

Figure 3.20: Quantification of the ferric nitrate (a) and hydroxyapatite (b) signal from the MD results. The diagonal line acts as a reference line to represent the linear trend the datapoints should follow for accurate MD quantification.

The hydroxyapatite signal has a considerable error associated with the datapoints in Figure 3.20b, which is unusual seeming the hydroxyapatite standards are factory manufactured specifically for calibrations. This could be a result of the inaccuracy of MARS Vision in measuring the material concentrations.

The following misidentification charts support the misclassification of ferric nitrate and hydroxyapatite in FN200, FN400, HA100, and HA200, which is evident in Figure 3.17.

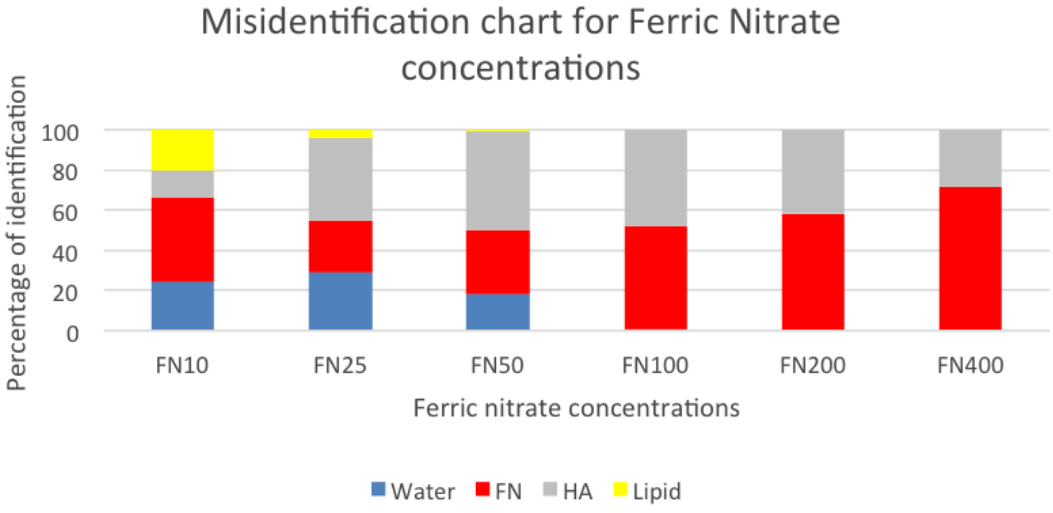

Figure 3.21: Misidentification charts for ferric nitrate in the FN phantom.

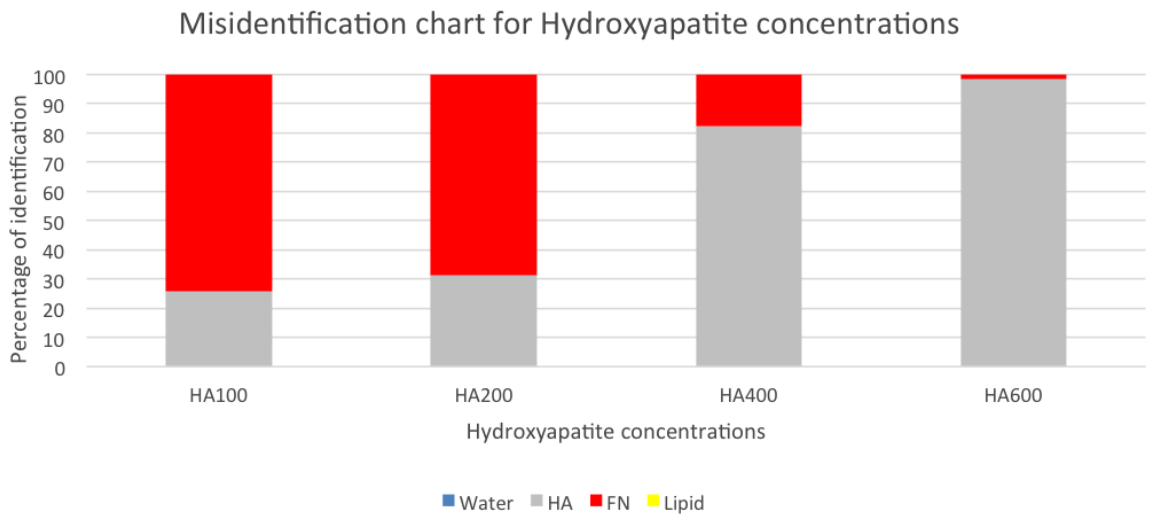

Figure 3.22: Misidentification charts hydroxyapatite concentrations in the phantom.

New methods

The misidentification between ferric nitrate and hydroxyapatite in samples FN200, FN400, HA100, and HA200 led to the implementation of new methods including the histogram method and their corresponding ROC curves, percentage correct, and scatter plots with marginal histograms.

Histogram method and ROC curves

The following histograms and ROC curves were produced using the coordinate information from ROIs' selected for the samples with misidentifications. The attenuation coefficients within the ROIs' were plotted in the following way for each energy bin to show the separation between the samples and the trend of the attenuation across the energies.

The comparison of HA100 and FN400, and FN200 and HA200 shows almost perfect distinction between the materials, with an AUC value representing complete separation across most energies. The separation between FN200 and HA100 is problematic, with the histograms containing each materials attenuation coefficients bearing significant overlap across the energies. This is especially apparent in the histogram for energy 4, which for FN200 and HA100 has a corresponding AUC = 0.5982, thus providing an inadequate result for distinguishing these two concentrations.

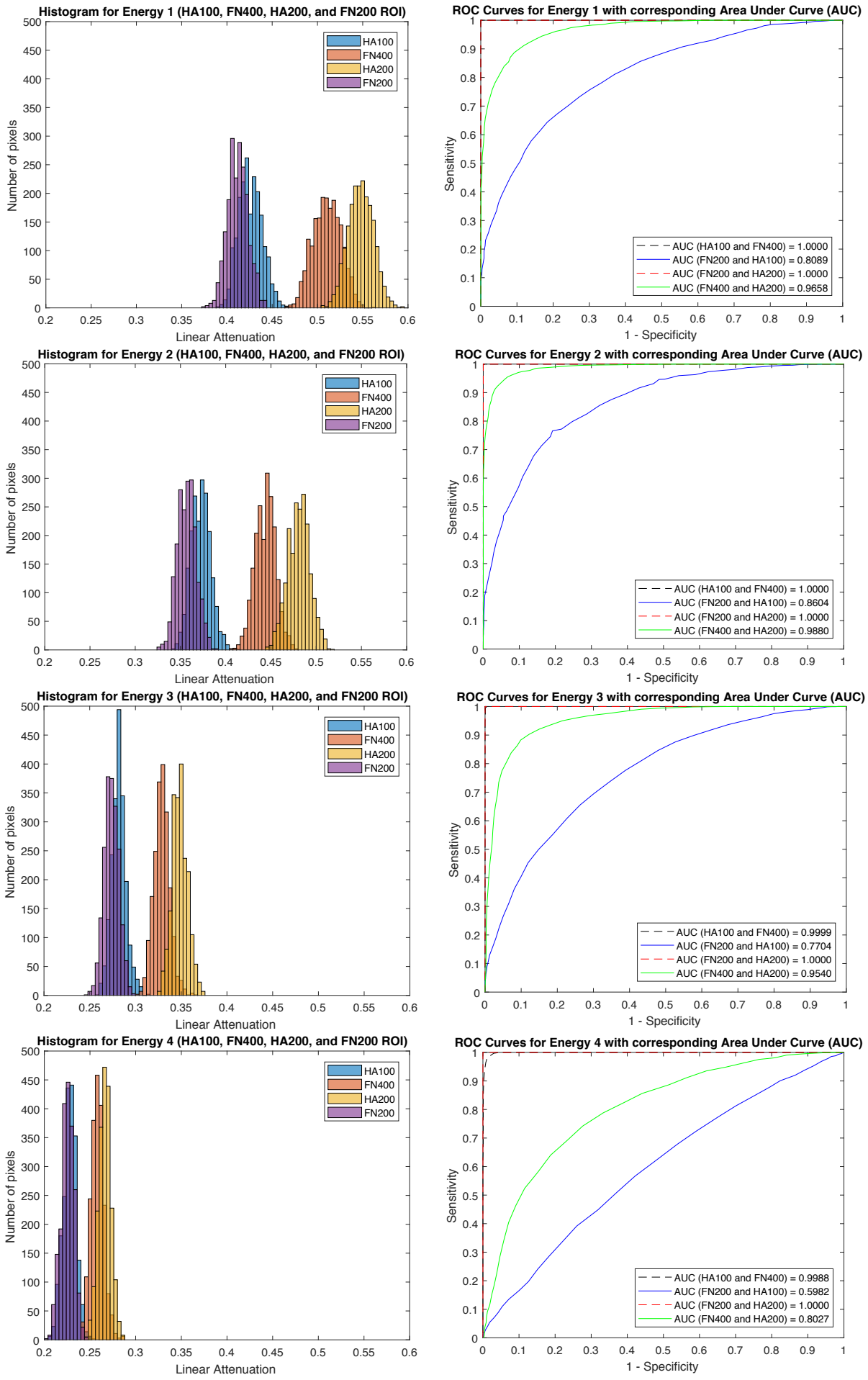

Figure 3.23: Histogram plots comparing HA100, FN400, HA200, and FN200 across the four energy bins. These are accompanied by ROC curves for each energy bin.

Percentage Correct (PC)

For the four energy bins, the following PC values were calculated. These values directly relate to the discrimination observed in the histograms and corresponding ROC curves. 2004 trials were used to calculate the PC values, this being equivalent to the number of pixels within each material ROI.

Percentage Correct	E1	E2	E3	E4
HA100 and FN400	1.0000	1.0000	1.0000	0.9990
FN200 and HA100	0.7929	0.8503	0.7445	0.5664
FN200 and HA200	1.0000	1.0000	1.0000	1.0000
FN400 and HA200	0.9631	0.9860	0.9471	0.7944

Table 3.2: Calculated PC values for HA100, FN400, HA200, and FN200, for the four energy bins.

Scatter plots with marginal histograms

Scatterplots were generated to visualize the relationship of the attenuation coefficients between the energies. By comparing Energy bin 1 vs. Energy bin 2, Energy bin 2 vs. Energy bin 3, and Energy bin 3 vs. Energy bin 4, a positive correlation was observed for the energies. Included in these scatterplots are the marginal distributions of the energy bin on the x-axis and energy bin on the y-axis as univariate histograms.

3.5.4 Conclusion

Only the FerricNitrate_Protocol@80kVp protocol successfully completed the material decomposition of the phantom. This still leaves the matter of whether the FerricNitrate_Protocol@80kVp and plaque UOC_Protocol_Aluminium protocol can be merged into a protocol that can have optimised parameters for scanning plaque specimens for intraplaque haemorrhage. Although the large ferric nitrate concentrations were implemented, there was significant misidentification of ferric nitrate and hydroxyapatite signal in the samples FN200, FN400, HA100, and HA200. Comparing these samples with one another, HA100 and FN400, and FN200 and HA200 showed almost perfect distinction across the four energy bins. Further scans would need to be run optimise this phantom.

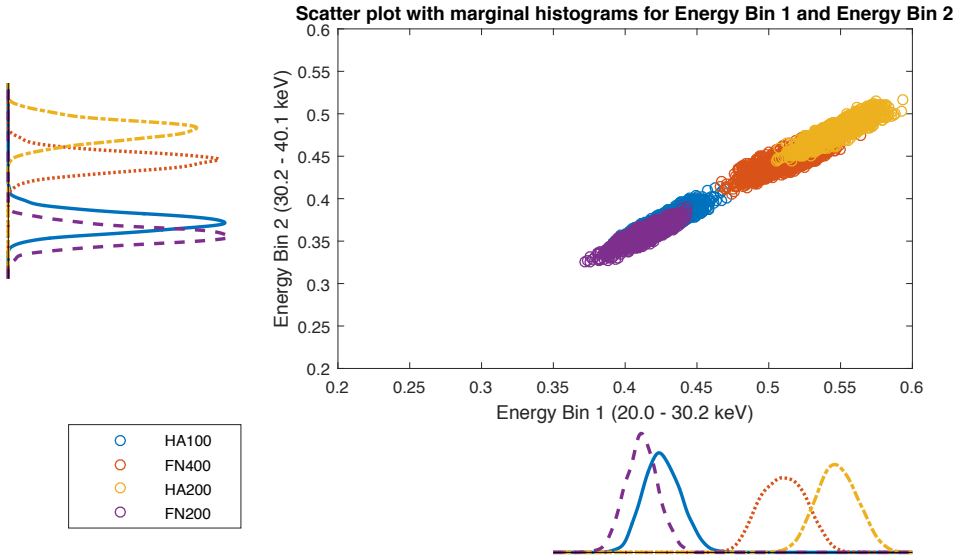

(a) Scatter plot comparing Energy 1 and Energy 2 attenuation coefficients.

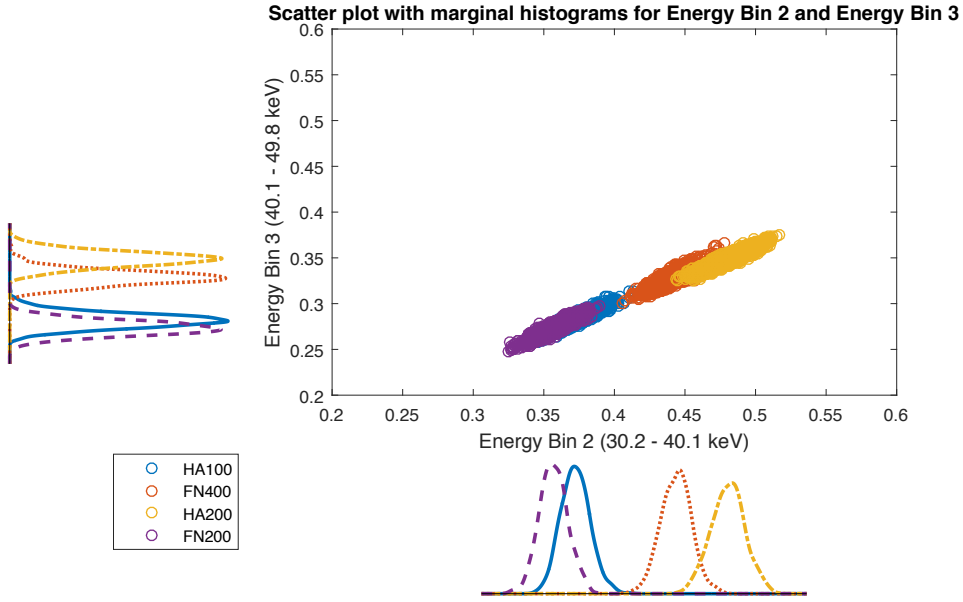

(b) Scatter plot comparing Energy 2 and Energy 3 attenuation coefficients.

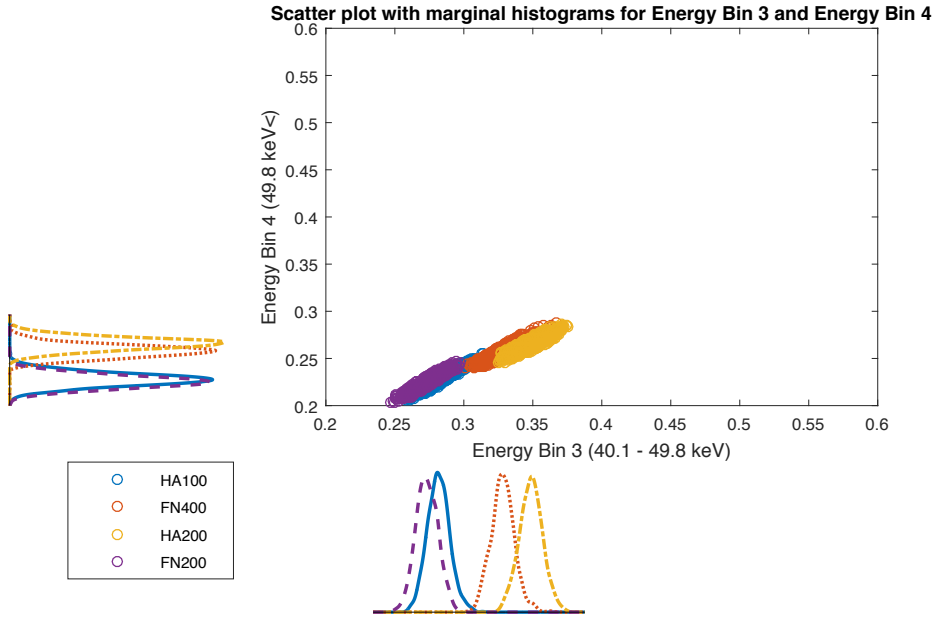

(c) Scatter plot comparing Energy 3 and Energy 4 attenuation coefficients.

Figure 3.24: Scatter plots with marginal histograms for E1 vs. E2, E2 vs. E3, and E3 vs. E4. See an explanation on the previous page in section 3.5.3.

3.6 FeCl and CaCl experiment

3.6.1 Aim

Following the results of the ferric nitrate phantom using large concentrations, a new experiment was launched, with the aim of distinguishing iron and calcium using the ferric nitrate phantom as a calibration phantom. To attempt to answer the questions surrounding material discernment of iron and calcium, a mixed solution was produced to try to determine the point at which there is enough iron in the voxel for the iron signal to predominate, and predominate over every other signal. Also in question is whether the dominant iron signal is different to the same concentration of calcium in a separate voxel. The significance of this experiment is that, when more than one material occupies part of a voxel, the material that is identified by the voxel will, in this case, determine whether there is iron or calcium present. This is important for accurately determining features of vulnerable plaque, such as intraplaque haemorrhage or microcalcifications.

3.6.2 Methods

A phantom was made up of three concentrations of FeCl (FeCl100, FeCl200, and FeCl400), three concentrations of CaCl (CaCl100, CaCl200, and CaCl400), a 50/50 mixture of FeCl200 and CaCl200, lipid, and water. The chloride in the FeCl and CaCl samples should effectively cancel out. The samples were made in moles, as 1g of Ca will have at least half the atoms of 1g of Fe. The scan was run using the FerricNitrate_Protocol@80kVp protocol on the same day as the ferric nitrate experiment in Section 3.5.

The concentrations used were 100, 200, and 400mM. In grams per ml that is:

- CaCl100: 14.7 mg/ml, CaCl200: 29.4 mg/ml, CaCl400: 58.8 mg/ml
- FeCl100: 23.05 mg/ml, FeCl200: 46.1mg/ml, FeCl400: 92.2 mg/ml

Figure 3.25: FeCl CaCl phantom.

3.6.3 Results and Analysis

The following MD image was optimised by presetting the LUT thresholds for the iron, calcium, and lipid channels. The minimum LUT thresholds were set as 0.1 for iron to represent a FN100 (100mg/ml) concentration, and 0.05 for calcium for HA50, with the maximum LUT threshold set as the maximum signal for each material. The minimum threshold for lipid was set to 0.8, with a maximum threshold at 1.0 to coincide with the fat density as approximately 0.9g/ml.

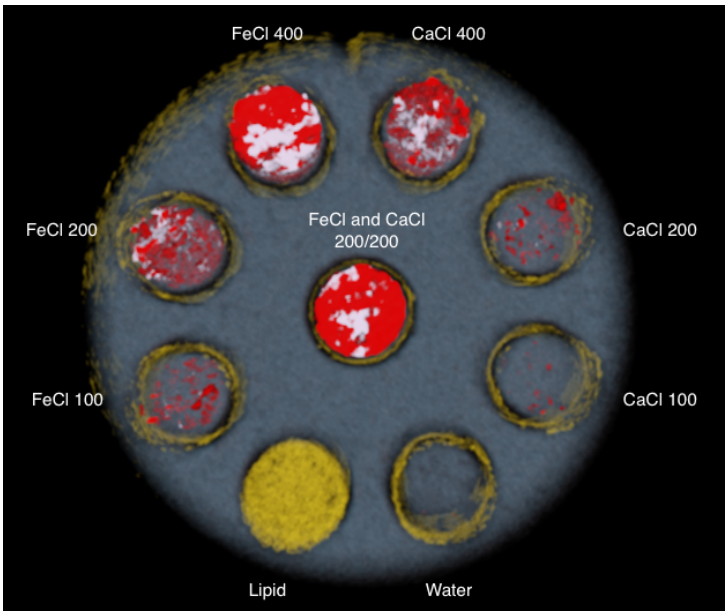

Figure 3.26: Optimised MD image of FeCl CaCl phantom. FN is shown as red, HA as white, water as blue, and lipid as yellow.

The analysis of the FeCl and CaCl samples was done using the ferric nitrate phantom in Section 3.5 as the calibration phantom. More suitable would be to use the three concentrations of FeCl and CaCl as the calibration materials. This was trialled, by running the MD using attenuation values from the FeCl and CaCl samples, however, the error stating 'Poorly formed basis vectors!' lead to the MD not running. As a result, the analysis here is based on the ferric nitrate phantom as the calibration phantom.

The following misidentification chart was produced. Most notable it the significant ferric nitrate signal observed in the mixed FeCl200/CaCl200 solution. In the CaCl solutions there is more misidentification from other materials such as water.

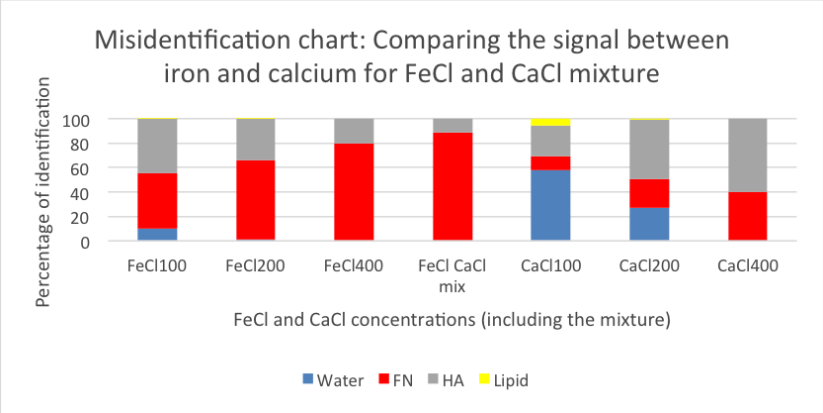

Figure 3.27: Misidentification chart comparing the ferric nitrate and hydroxyapatite signal in the FeCl, CaCl, and FeCl200/CaCl200 mixture solution.

By visualising the MD in MARS Vision, the quantity of ferric nitrate and hydroxyapatite (mg/ml) could be measured in the samples. This was done using an axial, coronal, and sagittal slice (only coronal slice data is shown in the following graph). FeCl100 and FeCl200 showed close quantification to their concentrations in mg/ml, with FeCl400 (92.2mg/ml) having a FN quantification of 146.24mg/ml in the MARS Vision MD. A significant undereading was observed across the CaCl samples, remembering these are made up in mg/ml. In the FeCl200/CaCl200 mixture, the ferric nitrate signal measured at 168.43mg/ml, while the hydroxyapatite signal measured at 9.39mg/ml.

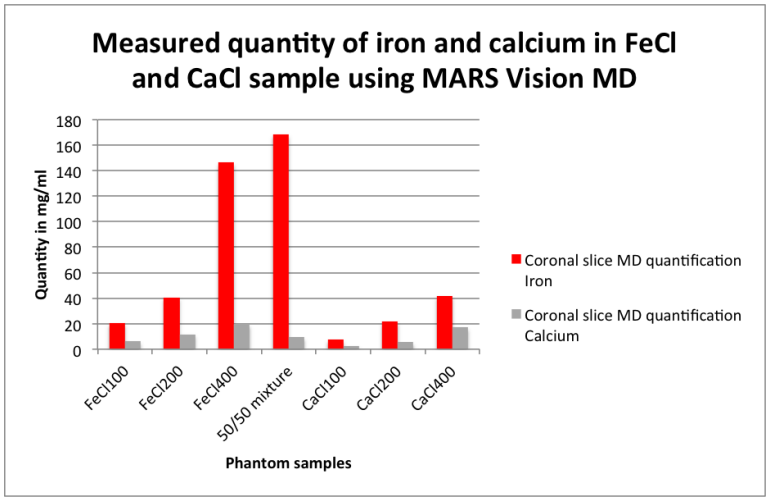

Figure 3.28: Quantification of ferric nitrate and hydroxyapatite in FeCl, CaCl, and FeCl200/CaCl200 mixture solution.

The reason behind the undereading of the samples is still unclear although testing of the scanner was performed. Possible causes include phantom design and beam hardening effects. Beam hardening is seen when an X-ray beam consisting of polychromatic energies passes through an object. Low energy X-ray photons are preferentially absorbed, with the remaining high energy photons not as easily attenuated. This leads to beam 'hardening'. This is an issue for high atomic number materials, which acquire increased attenuation at lower energies. The

design of the phantom and the placement of materials within the phantom may play a role in the observed undereadings, as high atomic materials such as hydroxyapatite may affect the attenuation coefficients measured from the ferric nitrate samples. Consequently, the ferric nitrate calibration phantom will effect the quantification FeCl, CaCl, and FeCl200/CaCl200 in the material decomposition.

3.6.4 Conclusion

In an attempt to answer the questions surrounding material discernment of iron and calcium the FeCl200/CaCl200 mixed solution showed a predominate iron signal over calcium, with a measured quantity of 168.04mg/ml over the calcium signal at 9.39mg/ml. Future work can further the progress of this experiment, by trialing different concentrations within the mixture solution, to determine what concentrations of iron and calcium create the turning point at which iron is distinguished over calcium. In this experiment, FeCl200 and CaCl200 were used in the mixture. It may be possible to reduce the FeCl concentration in the mixture, while keeping CaCl at 200mg/ml. This would be a practical next step to take. Continued investigations into the undereadings in the material quantification measurements should be undertaken to solve the issue for future scans.

3.7 Blood clots

3.7.1 Aim

Blood has various components, comprising erythrocytes, white blood cells, and platelets. These occupy 45% of blood volume. Platelets role is to interact with clotting proteins to prevent bleeding. Plasma is the liquid component of blood in which these components are suspended, occupying $\sim 55\%$ of blood volume. The aim of this experiment was to quantify how much ferric nitrate signal would be contained within the prepared blood clots. There should only be a ferric nitrate signal detected in the clots, as blood does not contain any calcium/hydroxyapatite.

3.7.2 Method

To conclude the ferric nitrate work, four blood clots were produced by my associate supervisor. The vials containing the clots were carefully stabilised to the phantom holder and scanned with parameters including a tube voltage of 80kVp, tube current of $55\mu A$, 100ms exposure time and 2mm Al filtration. The protocol energy bins were preset at 20.0 - 30.2 keV, 30.2 - 40.1 keV, 40.1 - 49.8 keV, and 49.8 - 80.0 keV. This scan was run after the FeCl and CaCl experiment, using the FerricNitrate_Protocol@80kVp protocol which was implemented in the ferric nitrate experiment in Section 3.5.

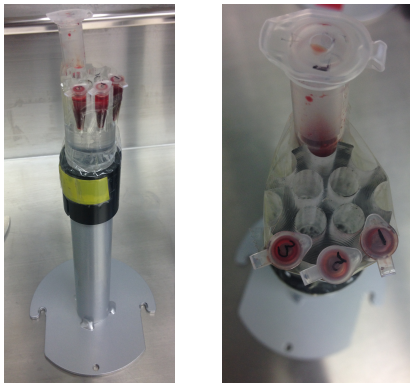

Figure 3.29: Blood clot phantom images.

3.7.3 Results and Analysis

The following spectral plot compares the Hounsfield Unit signal of the four clots against the ferric nitrate calibration phantom. As observed, the blood clots maintain an HU signal between FN25 and FN50, with an increase in signal seen in the fourth energy bin, reaching HU values between FN50 and FN100.

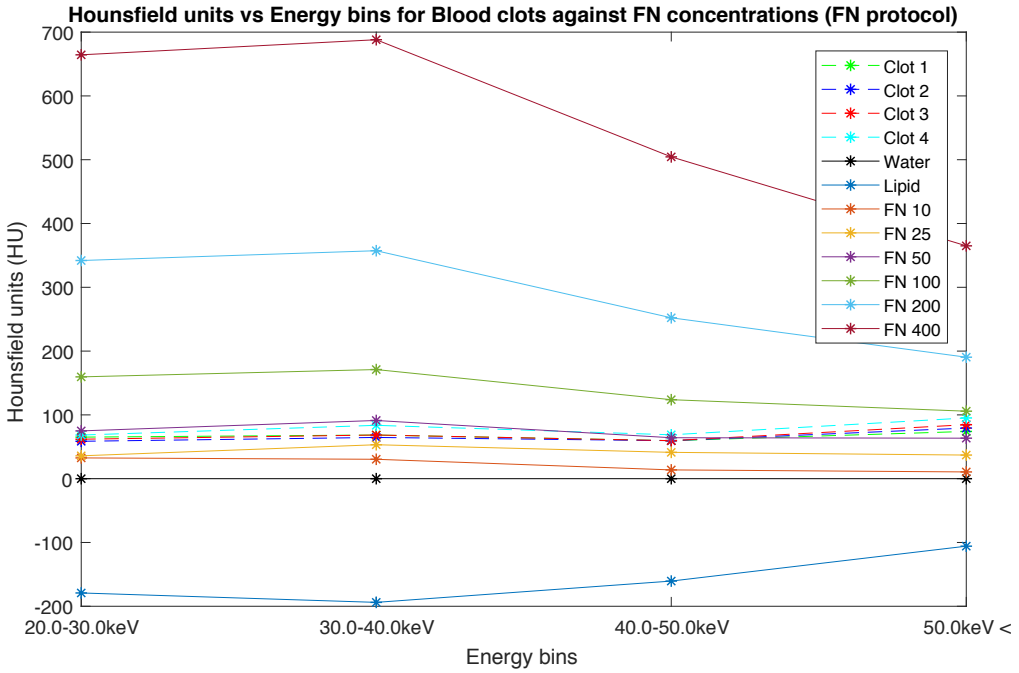

Figure 3.30: Spectral plot for the blood clots against the ferric nitrate calibration concentrations.

Using the calibration phantom with the large ferric nitrate concentrations, the MD was run for the blood clot scan. Visualising the result in MARS Vision, and setting the LUT minimum thresholds to eliminate misidentifications, the following optimised image was produced. There was HA signal observed in the MD image, however setting the HA LUT minimum threshold to 0.05 (equivalent to HA50) eliminated all HA signal in the image. This would be categorised as misclassified HA, as no calcium-like signal should be expected in the blood clots.

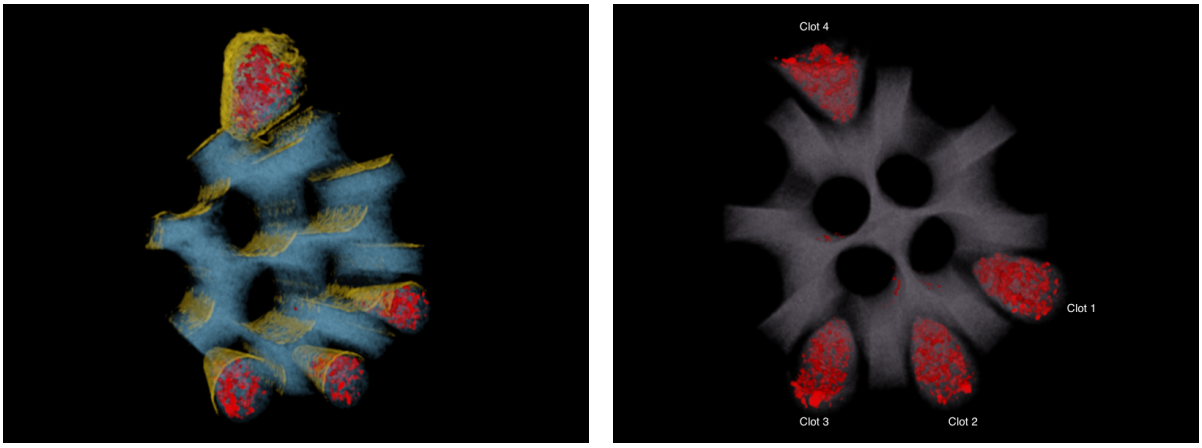

(a) Side on view of blood clot phantom with all materials present.

(b) Birdseye view of phantom, with FN, HA and energy signal shown.

Figure 3.31: Optimised MD images of blood clots. FN is red, HA is white (no signal observed), lipid is yellow, and water is blue.

Quantifying the amount of ferric nitrate within the blood clots was achieved in MARS Vision by taking a ROI in an axial, coronal, and sagittal slice, and measuring the average signal (mg/ml) and the standard deviation.

Clot 1	**Mean (mg/ml)**	**Standard deviation**
Axial	9.28348	17.6322
Coronal	8.65799	18.3771
Sagittal	8.62956	17.2479
Clot 2	**Mean (mg/ml)**	**Standard deviation**
Axial	5.51907	14.058
Coronal	7.94089	17.573
Sagittal	5.07026	13.0611
Clot 3	**Mean (mg/ml)**	**Standard deviation**
Axial	9.25611	19.6671
Coronal	10.4422	19.0955
Sagittal	6.63756	16.3017
Clot 4	**Mean (mg/ml)**	**Standard deviation**
Axial	6.72738	15.6001
Coronal	7.91244	17.4481
Sagittal	8.50159	17.1584

Table 3.3: Quantity of ferric nitrate in the four blood clots measured in an axial, coronal, and sagittal slice.

3.7.4 Conclusion

Using the calibration phantom with the large ferric nitrate concentrations, the MD was run for the blood clot scan. A ferric nitrate signal was successfully observed throughout all four blood clots, with no hydroxyapatite present.

3.8 Summary

To summarise the key points of this chapter:

- Intraplaque haemorrhage is a common identifying feature of complex lesions leading to acute ischaemic events, which arises from a disruption of thin-walled microvessels, resulting in erythrocytes leaking into the plaque.
- Calcification regions in atherosclerotic plaques defend against plaque destabilisation, while microcalcifications contribute to plaque instability by promoting stress accumulation within the ECM.
- There is a strong relationship between intraplaque haemorrhage and lipid, with intraplaque haemorrhage contributing to local lipid deposition, acting as a source for proinflammatory responses. The cholesterol content in erythrocytes could be an indicator of plaque progression to vulnerability.
- Misidentification was observed between samples of ferric nitrate and hydroxyapatite in the material decomposition. By implementing new methods, the energy information from the samples enabled separation of the material concentrations.
- The large ferric nitrate concentrations were more reliable at accurately identifying the presence of ferric nitrate. Although the small ferric nitrate concentrations more closely represent concentrations of iron found in the human body, significant misidentification was seen throughout the samples.
- The iron signal in the FeCl200/CaCl200 mixed solution predominated. Substantial underreadings of material quantifications were recorded, which may be a consequence of phantom design and beam hardening effects.

Chapter 4

Principal Component Analysis

4.1 Overview

This chapter introduces the technique of PCA, and its ability to evaluate spectral information in a dataset. The aim of using PCA is to analyse the ferric nitrate phantom datasets, and see whether PCA can be effectively implemented as a new method for distinguishing materials of similar spectral profiles such as iron and calcium. Significant advantages of using PCA include it not requiring prior knowledge of the materials being imaged, and that it can be applied to large datasets.

An introduction into PCA is given in section 4.2, with the methodology of how PCA was achieved on the datasets and the results detailed in sections 4.3 and 4.4, respectively. Section 4.5 gives conclusions to the use and effectiveness of PCA, and a chapter summary is described in section 4.6.

4.2 Principal Component Analysis (PCA)

What is PCA?

Principal Component Analysis (PCA) is a technique often used to make data easier to visualise and interpret. It is a mathematical algorithm that reduces the dimensionality of the data, while retaining most of the variation in the dataset [47] and reducing noise. The technique is very universal, as it can be applied to image data of any dimensionality, and requires no prior knowledge of the materials being analysed in the dataset (how the spectral information varies within the data) [48]. PCA is able to reduce the data dimensionality be identifying directions, called principal components, along which the variation in the dataset is maximal. The direction of the first principal component is along the path of the dataset that shows the largest variation and highest contrast. The second principal component is the direction uncorrelated to the first component along which the data shows the largest variation [49]. Remaining principal components continue in this manner until all data is represented [50]. Although the first principal component is generally viewed as containing most of the information

in the system, with the last principal components regarded as noise, principal components with small variances will elevate the subtle contrast between two very similar materials [51]. Along these directional axes in the new coordinate system, the dataset variances are uncorrelated - in other words, if two materials in a dataset have similar absorption spectra that are only slightly distinguishable, the PCA algorithm will emphasise the contrast between the two materials [52]. As a result, strong patterns in the data are accentuated, with the processed images having enhanced contrast and improved signal-to-noise ratio compared to the datasets original images.

PCA behind the scenes: The application of PCA to multi-energy data

The intent of PCA is to identify linearly independent patterns of variance within datasets, creating an image that has maximal contrast between materials. The following mathematical notations demonstrate this concept.

Let x represent K different energies. The aim is to find linear transformations $\alpha_i^T x$ that possesses maximum variance in contrast between materials [53]. α^T is the transpose of α, with the subscript i representing the ith principal component [52]. The linear transformation has the form:

$$\alpha_i^T x = \sum_{j=1}^{K} a_{ij} x_j \tag{4.1}$$

where α_{ij} are constants and x_j are elements of x. In the PCA solution the intensity value of each pixel is thus a weighted sum of the intensity values for corresponding pixels in the images for the multiple energies [52]. Lagrange multipliers are applied in the derivation of the PCA method, which maximise the variance of the dataset. This results in the following equation,

$$|\Sigma_x - \lambda I_K|\alpha_i = 0 \tag{4.2}$$

where Σ_x is a covariance matrix that describes the spread of intensity values across the vector space of x, λ represents the eigenvalue of Σ_x, and λI_K is a (K $\times$ K) identity matrix.

To carry out PCA, the following is performed for each voxel: Firstly, the covariance matrix is calculated. Σ_x is defined by

$$\Sigma_x = E\{(x - m)(x - m)^T\} \tag{4.3}$$

$$\Sigma_x = \frac{1}{K-1} \sum_{i=1}^{K} (x_i - m)(x_i - m)^T \tag{4.4}$$

where E is the expectation operator and m is the mean of x.

Following this, the characteristic equation for the eigenvalues λ is solved. The eigenvalues are then sorted in order of decreasing value.

$$\Sigma_x - \lambda I = 0 \tag{4.5}$$

With the sorted eigenvalues, the PCA images for each principal component of interest are generated. The eigenvectors of the algorithm detail the remapping of the brightness values of each pixel, with the eigenvectors filling the α_{ij} terms in equation 4.1. Each pixel is given a new brightness value by a weighted sum of the corresponding pixels in each of the spectral bands [52].

4.3 Method

PCA was completed using Matlab functions created by a past MARS PhD student. The main code reads in four `.tif` files (one for each energy bin) as a 480×480 single, then converts the four images to a `double`. The four `.tif` files used were from one slice chosen from each energy, which is not optimal for analysis. A new Matlab script was created, which loaded all `.tif` files from a scan as a stack in the Workstation. This was done for the four energies, resulting in four stacked folders for E1, E2, E3, and E4.

Next, the code prompts the user to input a start slice and a finish slice from which to analyse the `.tif` files within each stack. The number of files selected are calculated by taking the difference between the start and finish slices. From the start slice indicated, the number of files chosen, say 10, are taken and stored in a separate stack. These 10 `.tif` files are averaged by taking the mean, resulting in a single `.tif` file representing the averaged image over the 10 slices chosen between the start and finish slices. This was completed for the four energy folders. At this point, the averaged `.tif` files were converted to Hounsfield Units using the Hounsfield Unit equation, in order to increase the signal from the attenuation coefficients.

Using the new averaged `.tif` files in the main PCA code, the code specified the number of images as four (relating to the number of energy bins), and prompted the user for the number of materials. Air is included as a material, otherwise it is assigned to other materials. Through a `for` loop, a region of interest (ROI) was selected by the user for each material. This was generated by the inbuilt Matlab function `roipoly`. In a phantom with multiple concentrations of one material, only one material concentration can be selected to represent that material with the ROI. The code implemented two functions. The first function takes the matrix containing the ROI information and transforms into eigenspace. This is done by computing the singular-value decomposition (SVD)/PCA of the input matrix. Outputs of this function include the transformation matrix and transformed input. The second function measures the Euclidean distance in eigenspace. The PCA code generates binary images for the material channels, and maps the HU from each energy bin image onto the material bins, creating the PCA images of each material.

4.4 Results and Analysis

PCA was completed on the ferric nitrate phantoms using the large and small concentrations. This was implemented as one of the new methods to try and distinguish iron and calcium. The PCA code was run multiple times, performing trial and error with different material concentrations for the chosen ROI.

The following results are two best outcomes for the ferric nitrate phantom (large concentrations). The two outcomes that showed the most correct material identification used material concentrations HA600, FN50, and I9, and HA600, FN100, and I9.

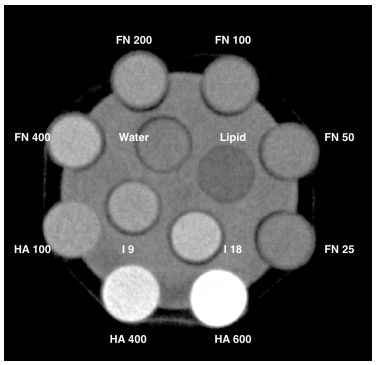

(a) Ferric nitrate phantom (large concentrations) for reference.

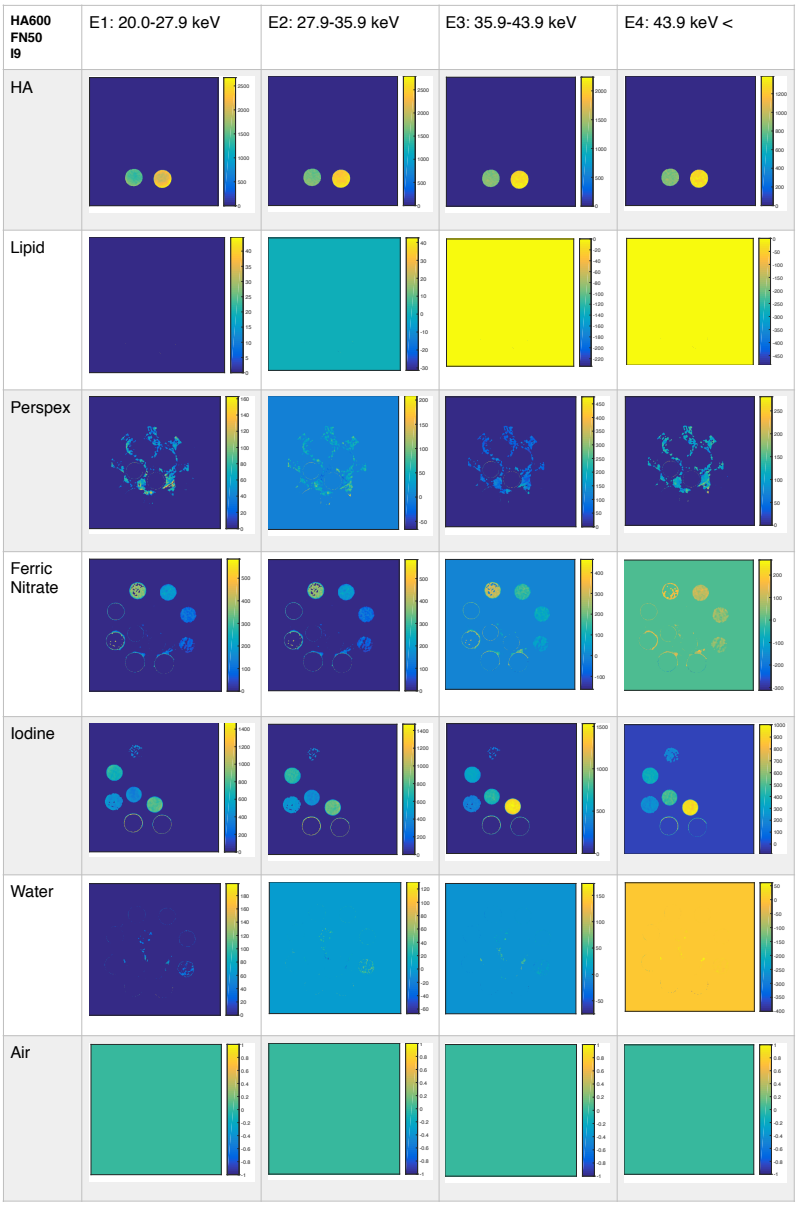

(b) PCA for ferric nitrate phantom (HA600, FN50, I9).

Figure 4.1: PCA for ferric nitrate phantom (large concentrations) using HA600, FN50, and I9 as the material ROI.

The hydroxyapatite channel recognised HA400 and HA600, while HA100 was identified in the iodine channel, along with FN400. Due to iodine's strong greyscale signal, PCA perceived the HU signal of HA100 and FN400 to more closely resemble the greyscale for I9 and I18 in the iodine channel. The k-edge of iodine is observed in E3 with an increased HU signal in the iodine channel. The ferric nitrate concentrations were correctly observed in the ferric nitrate channel, except for FN400. Lipid, water, and air did not have a significant HU signal, and hence their PCA images have a colour representing a signal at 0 HU, as seen on the colour scale alongside each PCA image. The following is the PCA results for HA600, FN100, and I9.

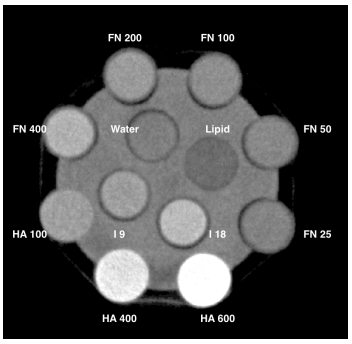

(a) Ferric nitrate phantom (large concentrations) for reference.

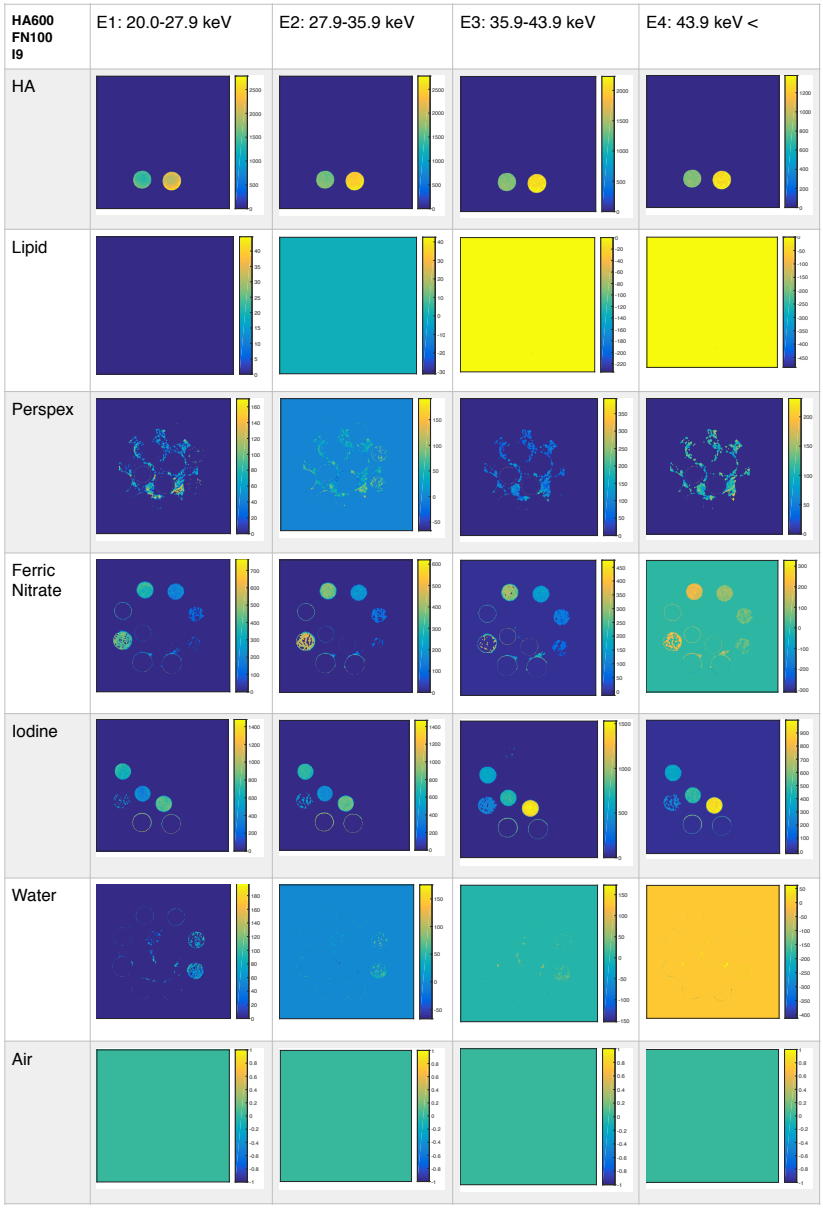

(b) PCA for ferric nitrate phantom (HA600, FN100, I9).

Figure 4.2: PCA for ferric nitrate phantom (large concentrations) using HA600, FN100, and I9 as the material ROI.

The hydroxyapatite channel recognised HA400 and HA600, while HA100 was identified in the ferric nitrate channel. Across the energies in the iodine channel, I9 and I18 were clearly identified, along with FN400 and speckled regions of HA100. In the water channel there are speckled regions of FN25 detected. As in Figure 4.1, lipid, water, and air have a small HU signal, resulting in 0 HU across the energies.

The following PCA result is the best outcome using the ferric nitrate phantom with small FN concentrations. The best material concentration combination was HA100 and FN10 as the material ROI.

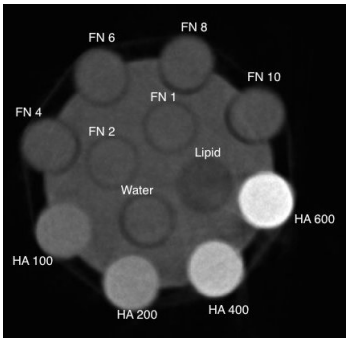

(a) Ferric nitrate phantom (small concentrations) for reference.

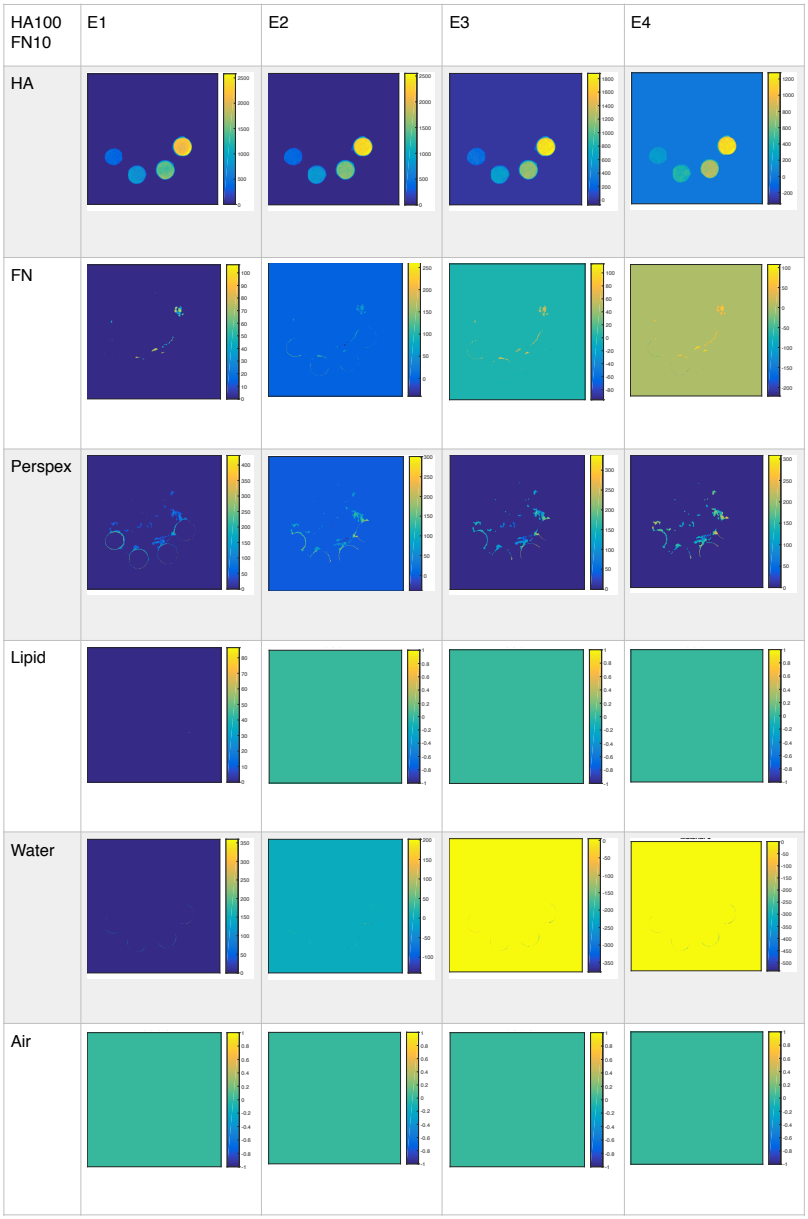

(b) PCA for ferric nitrate phantom (HA100, FN10).

Figure 4.3: PCA for ferric nitrate phantom (small concentrations) using HA100 and FN10 as the material ROI.

The hydroxyapatite concentrations have such a dissimilar HU signal compared to the small ferric nitrate concentrations, causing all the HA concentrations to be correctly identified in the HA channel. In the ferric nitrate channel, only FN10 shows some speckled signal across the energies. Due to the low HU signal for the lower concentrations of ferric nitrate, and of lipid, water, and air, the rest of the PCA images observe a signal of 0 HU.

An improvement that should be considered for future use of PCA is incorporating more than one material concentration into the ROI selection. In this analysis, one concentration of each material was chosen in any given run of the PCA code. Trial and error was used to determine what material concentration combinations gave the most accurate outcome of material identification. By creating some additional Matlab code that could take on more than one concentration, and use this ROI information in a way to create a basis for each material, a more accurate PCA outcome may result.

Currently, the PCA outcomes depend entirely on the material concentration combination chosen. For the ferric nitrate phantom using large FN concentrations, if FN400 was chosen to represent the ferric nitrate channel, any material that showed a similar HU/greyscale signal to FN400, such as HA400 and HA600, were misidentified as ferric nitrate. If a low HA concentration was chosen, say HA100, any HU/greyscale signal above HA100 may fall into a different channel, such as HA400 and HA600 identifying in the iodine channel. This was due to iodine's strong HU signal. An attempt was made to produce some Matlab code to improve the outcome of PCA, but was not completed in the timeframe of this thesis.

4.5 Conclusion

PCA performs moderately for analysing HU/greyscale and its ability to distinguish materials. For the ferric nitrate phantom with large FN concentrations, two optimal outcomes were presented, although there were still some material concentration misclassifications. The ferric nitrate phantom with small FN concentrations had strong identification of all four hydroxyapatite concentrations. FN10, the highest ferric nitrate concentration in the phantom, was the only FN sample to show any signal in the ferric nitrate channel. This was due to the other FN samples having too smaller concentration.

Comparing PCA to the MD results for the ferric nitrate phantoms, accurate HU quantification is recorded with PCA. Looking at Figure 3.4b and Figure 3.5b, the ferric nitrate phantom spectral plots (large concentrations), the Hounsfield Units recorded match the HU displayed in the FN and HA channel of the PCA chart in Figure 4.1b and Figure 4.2b. This is also represented in the ferric nitrate phantom using small FN concentrations. It was noted in the PCA chart that only FN10 showed any FN signal in the FN channel (Figure 4.3b). This is supported by the spectral plot (Figure 3.12b) in the Iron vs. Calcium chapter, where FN10 is the only

ferric nitrate sample to have positive HU across all energies. The other ferric nitrate samples were too low in concentration for an accurate HU reading, hence they have shown no signal in PCA. The four HA standards in the phantom show accurate HU measurements in energy image analysis and with PCA.

Although PCA is not a perfect technique and does not yet possess 100% correct identification of all materials, it is a worthwhile technique to understand and develop. The phantom used would need to be optimised and trialled, to see how the PCA code behaves with different material concentrations. By extending the code to hold more than one concentration per material, the ability of PCA to distinguish materials could be improved.

4.6 Summary

- PCA is a mathematical algorithm that uses a linear transformation to rotate the data into a new coordinate system. This reduces the dimensionality of the data while maximising the variances of the dataset.
- It is a very applicable technique, which can make features in the original data visible that were previously not discernible. PCA requires no prior knowledge of the materials being analysed in the dataset, with resultant images often having improved contrast and signal-to-noise ratio.
- PCA was performed on two phantoms, the ferric nitrate phantom with large FN concentrations, and the ferric nitrate phantom using small FN concentrations. The best outcomes from PCA were presented. For the ferric nitrate phantom (large concentrations), the best material concentration combinations were HA600, FN50, and I9, and HA600, FN100, and I9. The ferric nitrate phantom (small concentrations) had the best material identification using the samples HA100 and FN10.
- Comparing PCA to MD results, accurate Hounsfield Units were recorded between the spectral plots of the ferric nitrate phantoms and PCA.
- PCA correctly identified some materials, with the odd misclassification. Further improvements to the PCA code to incorporate more than one material concentration into the ROI selection could improve the ability of PCA to distinguish materials.
- PCA was included in the 1st version of MARS Vision for material decomposition, but has since been removed. Although PCA does not yet possess 100% correct identification of all materials, PCA should be implemented into MARS Vision again alongside current material decomposition techniques. With further improvements, PCA would provide team members with an additional method to compare results with MD analysis.

Chapter 5

Plaque and ApoE mice studies

5.1 Overview

This chapter displays the results of multiple atherosclerotic plaque scans and apoE-deficient mouse scans. The significance of scanning carotid plaque specimens relates to the identification of calcifications for interpreting plaque stability, and visualising necrotic lipid cores, which are a known feature of vulnerability. Studying atheromas is linked with the apoE mouse model, which is well established for human atherosclerosis research.

Section 5.2 looks into atheroma research, showing the capability of the MARS spectral scanner for plaque scanning and material decomposition. Section 5.3 describes the use of apoE-deficient mice on atherosclerosis research, displaying MD results from scans performed on apoE mice. A summary of this chapter is given in Section 5.4.

5.2 Atherosclerotic plaques

5.2.1 Atheroma research

The identification of vulnerable atherosclerotic plaque features in spectral CT has increased the amount of information that can be visualised and interpreted. To verify what has been identified in CT images, histology is a useful technique for studying the microscopic composition of tissues in an atheroma. Histological classification of plaques is often used to denote a plaques progression and stabilisation.

The atherosclerotic plaques studied here are from the carotid artery. These are surgically excised after the patient has suffered a stroke. Most strokes are associated with carotid bifurcation disease, with the majority thromboembolic in origin. The carotid bifurcation is the intersection between the common carotid and the internal and external carotid arteries, which supply blood to the brain, and the face and scalp, respectively. The formation of a clot (thrombus) in a blood vessel breaks loose and travels in the blood stream to plug another vessel, causing a blockage

in the carotid artery and a subsequent stroke.

Histological examination of plaque specimens is achieved through lipid staining, which highlights lipid structures in biological tissues for microscopic viewing. The technique of lipid staining has become a valuable tool in detecting and differentiating components of lipid within tissues. Cholesterol is the major lipid variety in atherosclerotic lesions and accumulates in unesterified and esterified forms [54]. Neutral lipids are hydrophobic molecules that lack charged groups and act as storage lipids for cells. They include glyceryl lipids such as triacylglycerols and cholesterol esters. When there are excess nutrients present in the cells the storage lipids accumulate, and when the amount of neutral lipids incorporated into biomembranes reaches capacity, they are sequestered from the cytosolic environment in the form of lipid droplets [55]. Upon requirement, the storage lipids are mobilized by triacylglycerol lipases and steryl ester hydrolases.

Studies into lipid deposition in atherosclerosis have highlighted cholesterol's role in plaque progression. Rapp et al. established that an increased percentage of free cholesterol (in relation to total cholesterol) was associated with evolution of the atherosclerotic process [56]. It was demonstrated by Klemp et al. that lesion cores exhibited an increase in the percentage of free cholesterol, whereas lesion caps had an enrichment of cholesteryl esters [57]. These studies give momentum to the technique of lipid staining, and for uncovering what progressive role lipid deposition plays in atherosclerosis.

There are a handful of dyes used for lipid staining. The lipid-soluble dye oil-red O only stains neutral (hydrophobic) lipids such as esterified cholesterol and triglyceride, because their solubility in liquid deposits in these lipids [58]. Oil-red O staining has been implemented alongside fluorescent-labeled oxLDL uptake to optimize the method for assessing foam cell formation through the intracellular lipid accumulation of macrophages [59]. It has been shown that most plaques, particularly advanced lesions, contain lots of non-neutral lipids such as unesterified (free) cholesterol and cholesterol crystals, so oil-red O would not stain significant portions of the lipids present.

In contrast, the fluorescent probe filipin stains non-neutral lipids, specifically binding to 3-B-hydroxysterols [60]. One study looking into the localization of unesterified cholesterol in human atherosclerotic plaques suggested that unesterified cholesterol could be associated with calcium-containing deposits [61]. The use of filipin and oil-red O simultaneously allows for differentiation between unesterified and esterified cholesterol, respectively, with generally no overlap in accumulation in the same cells or in the same extracellular loci [58].

Nile red is a dye that stains both neutral and non-neutral lipids. It acts as a fluorescent hydrophobic probe, as it is only strongly fluorescent in the presence of a hydrophobic environment. The dye is very soluble in the lipids it is intended to show, and does not interact with any tissue constituent except by solution [62]. An additional feature of Nile red is its ability to stain in slightly different colours. When it is dissolved in neutral lipids such as triacylglycerol and cholesterol ester droplets, Nile red fluoresces yellow-gold. However, when Nile red dissolves in more polar solvents or phospholipids, the dye fluoresces red [63]. The ability of Nile red to stain neutral and non-neutral lipids with varied colouring may be advantageous over oil-red O and filipin for assessing lipid deposition in atherosclerotic lesions.

Throughout the timeframe of this thesis, carotid plaque specimens donated by patients from Christchurch hospital were collected and stored to await scanning. The aim of scanning these plaques was to see how well the scanner could determine calcifications, among regions of lipid and the tissue/water signal. Ideally, lipid staining would have been performed to verify the composition of the plaques, however the timeframe of the thesis could not accommodate this.

5.2.2 Method

Plaque specimens were collected from surgery and immediately stored in an -80 or -20 freezer, depending on the time at which the plaques intended to be scanned. The plaques were defrosted for the scan. A HA calibration phantom containing concentrations of hydroxyapatite, lipid, and water was scanned before (or after) the plaque scan, but more importantly on the same day, to ensure an accurate material decomposition. The plaques were then individually positioned into a PCR tube and secured to the phantom holder. For the HA calibration scan and the plaque scans, the UOC_Protocol_Aluminium protocol was used, with a tube voltage of 118kVp, tube current at 23μA, exposure time of 100ms, and a 2mm Al filtration. The four energy bins used were in the range 30.0 - 39.9 keV, 39.9 - 50.0 keV, 50.0 - 60.0 keV, and 60.0 - 118.0 keV.

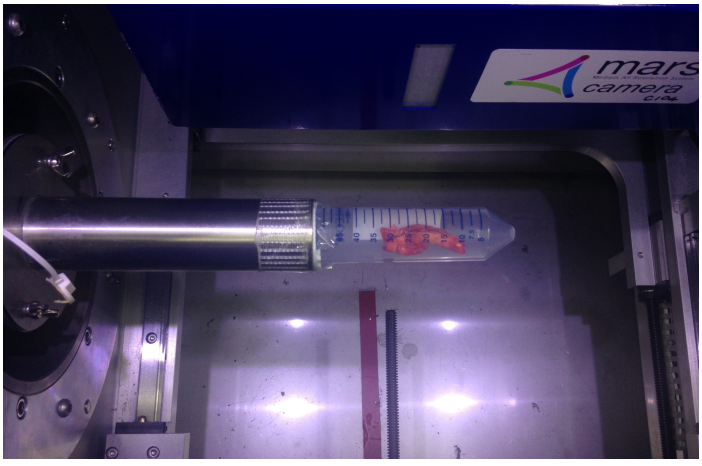

Figure 5.1: Picture of a carotid plaque specimen in the MARS Spectral scanner.

5.2.3 MD plaque images

The following plaques were scanned in one day with the HA calibration phantom. The plaques were cut longitudinally through the bifurcation and photographed by a UC Biological Sciences PhD student. The midsections of each plaque are positioned alongside their MD image. The results suggest a partial volume effect from the lipid channel. There is no strong lipid signal within the plaque to represent a lipid core, these suspected areas identifying as a water/tissue equivalent. Lipid is only observed around the surface of the plaque, which is seen as a partial volume effect. We expect to see a necrotic lipid core in some of these plaques.

Interpreting these results in regards to calcium, lipid, and iron content, these are culprit lesions in patients that have recently had a stroke, and hence the rupture has begun to heal before endarterectomy surgery has excised the plaque. As a result, some lipid core has potentially spilled out, and a blood clot in the repair phase indicates the presence of concentrated iron in the plaque region. Microcalcifications are common in plaques, and may be detectable in the MARS scanner through sub-voxel sized HA deposits giving a calcium signal spectrally for the voxel. There may be more calcium and iron present in the carotid plaque specimens rather than lipid, which may have escaped in the rupture, hence the importance of creating a phantom capable of measuring iron in plaque specimens.

In regards to the scanning of the plaques, the ability to identify lipid may be a result of the protocol used. The Al protocol may identify more voxels as calcium (with no set thresholds), and hence the MD cannot give an accurate lipid content. If the Al protocol is much more sensitive to calcium, a future experiment would be to scan the same plaque specimens with the brass protocol, which may give significantly less calcified voxels and measurable lipid content. The use of a brass filter in a brass protocol should provide more reliable microcalcification assessment. Notable also is the update in camera from a one-chip camera to a three-chip camera partway through the year. This may have played a role in the plaque scanning, with the detection of lipid when calcium is present in the phantom. Relating to the phantom work throughout this thesis, an aluminium filter protocol was used. For plaque scanning, the Al protocol was recommended as it was used for all phantom experiments, and its ability to image plaque specimens in previous theses makes it an established protocol. Further experiments to determine why the lipid signal is not represented correctly are needed, with histology being performed on plaque specimens to confirm the composition. Another experiment involving plaque specimens and the ferric nitrate phantom work includes using the ferric nitrate samples as the calibration phantom, in order to investigate possible intraplaque haemorrhage within the specimens. The phantom and protocol need continued work to be optimised.

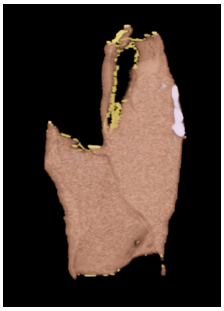

(a) Plaque 82 LHS.

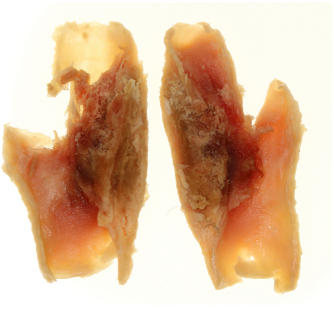

(b) Plaque 82 photograph.

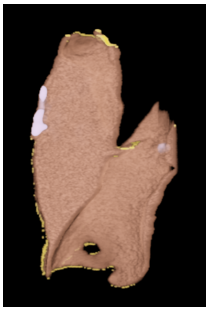

(c) Plaque 82 RHS.

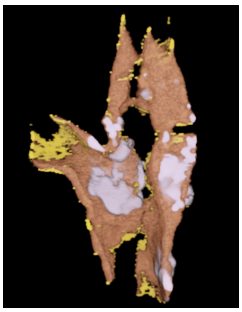

(d) Plaque 94 LHS.

(e) Plaque 94 photograph.

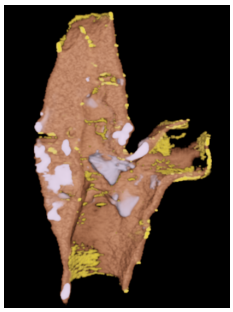

(f) Plaque 94 RHS.

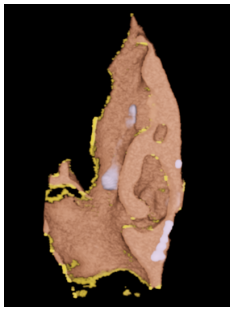

(g) Plaque 115 LHS.

(h) Plaque 115 photograph.

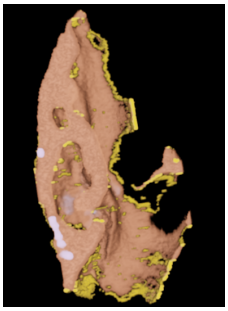

(i) Plaque 115 RHS.

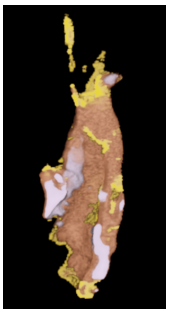

(j) Plaque 118 LHS.

(k) Plaque 118 photograph.

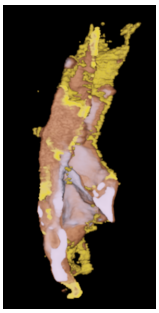

(l) Plaque 118 RHS.

(m) Plaque 136 LHS.

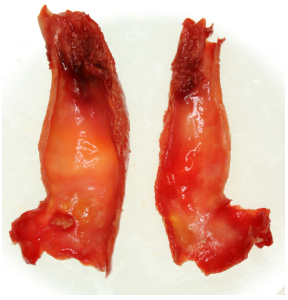

(n) Plaque 136 photograph.

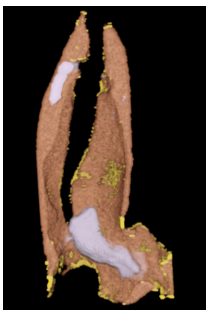

(o) Plaque 136 RHS.

Figure 5.2: Plaques 82, 94, 115, 118, and 136 photographs and MD results.

5.3 Apolipoprotein E-deficient mouse model

5.3.1 ApoE mouse model

To model atherosclerosis in research, the apolipoprotein E-deficient (apoE-/-) mouse was created for the purpose of studying atherosclerotic lesions resembling those observed in humans. The purpose for using this mouse model relates to the long term goal of visualising atherosclerosis in humans. By being able to see atheroma progression in apoE mice, the next step is to see this in live mice using the MARS scanner, progressing towards scanning patients susceptible to atherosclerosis. Apolipoprotein E is a glycoprotein synthesised mainly in the liver and brain, and is a component of all lipoproteins except low-density lipoproteins [64]. ApoE functions as a ligand for lipoprotein receptors, mediating the clearance of chylomicrons and very low-density lipoprotein remnants. ApoE is also synthesised by monocytes and macrophages in vessels, and is suggested to have local effects on cholesterol homeostasis and inflammatory reactions in atherosclerotic vessels [65]. Therefore, quality MARS images of apoE mice will enable features of atherosclerotic lesions to be interpreted and quantified within aortic vessels.

A knockout mouse is a genetically modified mouse that has an existing gene inactivated, or 'knocked out', which is replaced/disrupted with an artificial piece of DNA. In the apoE model, the gene coding for the apoE protein is inactivated by gene targeting to disrupt the apoE gene in embryonic stem cells [66]. Specifically, the creation of knockout mice involves the insertion of the neomycin resistance gene by homologous recombination in place of exon 3 and part of intron 3 of the apoE gene [67][68]. The lack of apoE protein in their plasma impair the clearance of lipoproteins, leading to the development of hypercholesterolaemia and spontaneous atherosclerosis.

ApoE knockout mice are an established model in atherosclerosis research. This rodent model resembles humans metabolically and pathophysiologically; its size allows metabolic and physiological studies, with mice developing end-stage lesions comparable with that in humans [67]. These atherosclerotic lesions are aggravated when mice are fed a high-cholesterol, Western-type diet [69]. Studies have demonstrated that apoE mice develop a full range of lesions, from fatty streaks to fibrous plaques. Nakashima *et al* noted that lesion development in mice fed a chow and a Western-type diet was not only seen in the aortic root but throughout the aorta and its principal branches [70]. This lesion development throughout the arterial tree was not observed in control mice. A common feature of atherosclerosis is an increase in the stiffness of the arterial wall, leading to decreased vascular elasticity and compliance. Research groups [71] [72] measuring vascular stiffness though pulse-wave velocity (which increases with increasing stiffness) indicated that apoE knockout mice have increased cardiac output and stroke volume, along with decreased peripheral vascular resistance. The elevated cardiac output could be a result of coronary atherosclerosis and endothelial dysfunction, limiting blood supply to the

heart, forcing the heart to work harder.

5.3.2 Mouse scans

Throughout the timeframe of this thesis, a handful of apoE mice scans were performed. The following scan used a 12 month old male apoE mouse weighing 32g, with the goal of visualising lipid signal in the liver and potential arteries, and looking for calcifications. The calibration phantom for all mice scans contained concentrations of hydroxyapatite, lipid, and water. The Al_Protocol_UOC protocol was implemented, with scan parameters including a tube voltage of 118kVp, tube current $17\mu A$, exposure time of 220ms, and 2mm Al filtration. The four energy bins were set at 18.0 - 29.9 keV, 29.9 - 44.9 keV, 44.9 - 77.9 keV, and 77.9 - 118.0 keV.

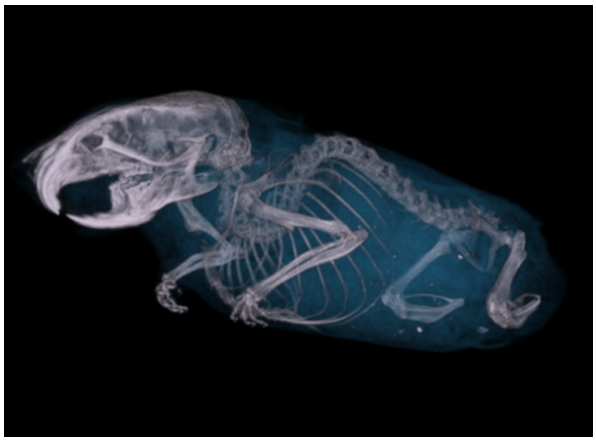

(a) MD image showing energy and water signal.

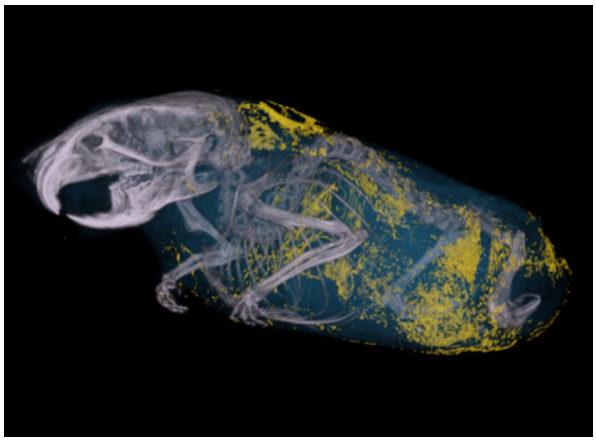

(b) MD image showing energy, lipid and water signal.

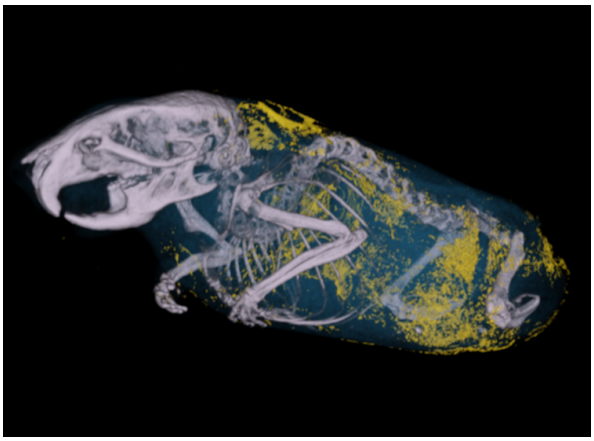

(c) MD image showing energy, HA, lipid, and water signal.

Figure 5.3: MD images of 12 month old male apoE mouse. The hydroxyapatite signal is white, lipid is yellow, and water/tissue is blue.

The material decomposition showed lipid signal around the body, with a dense signal observed in the area about the liver. This suggests the mouse may have had a fatty liver due to its inability to clear lipoproteins sufficiently. While dissecting the mouse after scanning, the liver had areas of a lighter colouring rather than the deep red the liver is normally. This supports the observation of fat deposition within the liver. No calcifications or lipid relating to

atherosclerosis were detected. This is due to the image resolution and accurately deciphering the area in the whole mouse scan where calcifications and lipid cores are expected. The ability to accurately identify calcifications and lipid in the liver and aorta in the whole mouse scan was quite tricky. In the next apoE mouse scan, the aorta and liver would be dissected and scanned separately, to see it that would help visualise features of atherosclerosis.

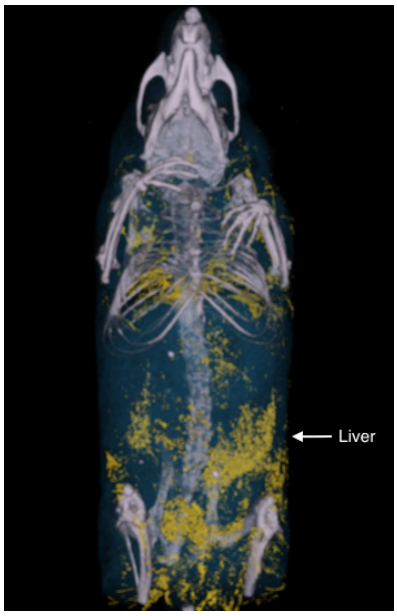

Figure 5.4: Longitudinal view of apoE mouse scan. Dense lipid signal (yellow) seen in the area where the liver may be located.

5.3.3 Aorta and liver scan

In this experiment an old apoE mouse was scanned and dissected to remove the aorta and liver to be scanned separately. The motivation behind this was to scan the organs where calcifications and lipid were expected. By doing this outside the body, a clearer view can be achieved, without the obstruction of the mouse body reducing the visualisation of these organs. The UOC_Protocol_Aluminium protocol was implemented, with scan parameters including a tube voltage of 118kVp, tube current $23\mu A$, exposure time of 100ms, and 2mm Al filtration. The four energy bins were set at 30.0 - 39.9 keV, 39.9 - 50.0 keV, 50.0 - 60.0 keV, and 60.0 - 118.0 keV.

Figure 5.5: Picture of apoE mouse aorta and liver in PCR tube for scanning.

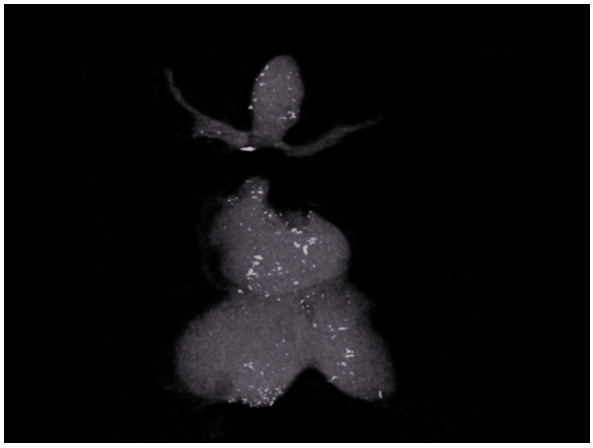

(a) MD image showing HA signal.

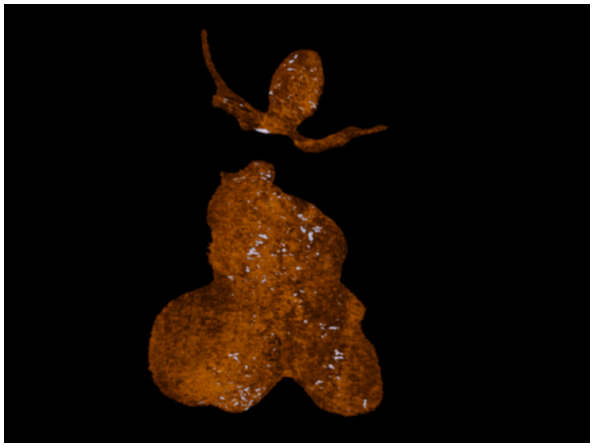

(b) MD image showing HA and water signal.

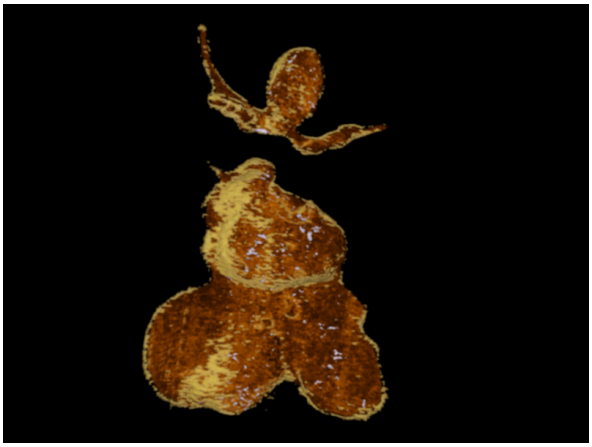

(c) MD image showing HA, lipid, and water signal.

Figure 5.6: MD images of the aorta and liver of an old apoE mouse. HA is represented in white, lipid in yellow, and water/tissue in orange.

The HA signal was set to 0.05 in the MD, to represent HA50. Possible microcalcifications in the liver are observed in Figure 5.6a. Most notable is the large calcified region at the intersection of the descending aorta and the heart. This is a very strong signal of a suggested calcified plaque. Lipid signal tended to show around the surface of the aorta and liver, this being a result of the partial volume effect. By dissecting the aorta and liver and scanning separately, areas of calcification and lipid deposition can be visualised, which may not have been identifiable in the whole mouse scan. These MD images of the whole mouse scan (Figure 5.3) and the apoE mouse aorta and liver (Figure 5.6) have not used any contrast agent to help with the visualisation; the images are a result of the calibration phantom and optimising the MD images based on the density of the materials and the HA misidentification chart.

5.4 Summary

- Lipid staining is a useful tool in histological examination, highlighting lipid structures in atherosclerotic plaques for microscopic viewing.
- The lipid-soluble dye oil-red O only stains neutral (hydrophobic) lipids such as esterified

cholesterol and triglyceride, because their solubility in liquid deposits in these lipids. The fluorescent probe filipin stains non-neutral lipids, specifically binding to 3-B-hydroxysterols. Nile red is a dye that stains both neutral and non-neutral lipids. It acts as a fluorescent hydrophobic probe, as it is only strongly fluorescent in the presence of a hydrophobic environment.

- Carotid plaque specimens were scanned with the MARS Spectral scanner, identifying regions of calcifications. Little lipid signal was observed in suspected necrotic core regions. Further experiments are needed to determine the reason for this.

- In the apoE mouse model, the gene coding for the apoE protein is inactivated by gene targeting to disrupt the apoE gene in embryonic stem cells. A 12 month old male apoE mouse was scanned to investigate the hydroxyapatite and lipid signal. An apoE mouse aorta and liver were dissected and scanned separately. A large calcified region was located at the intersection of the descending aorta and the aorta. This was measured as equivalent to HA80 by setting the HA signal to 0.08 to eliminate the calcifications in the liver using the MARS Vision software.

- The apoE mouse and aorta/liver scan show the value of the MARS spectral scanner, as these images have not used any contrast agent to aid the visualisation. The optimised images are based solely on the calibration phantom and material decomposition.

Chapter 6

Conclusion

The objective of this research was to perform quantitative imaging of vulnerable atherosclerotic plaques using the MARS spectral scanner. Each of the main components in atherosclerosis were investigated, including lipid, iron, and calcium. Lipid, iron, calcium and water-like components of plaque have distinguishable energy responses according to their spectral profiles, making them visible in the material decomposition. The concept of spectral CT was described, with details of how the scanner uses Medipix x-ray detectors to attain multiple-energy attenuation data. The value of the MARS spectral scanner in molecular imaging was discussed, with benefits in depicting markers of disease activity and disease burden, especially in the role of identifying and directing treatment for vulnerable atherosclerotic plaque.

Lipid experiments involving LDLs were established by joining iodine to the LDL. With accumulated LDL in lipid regions of atheromas, successfully joining a high Z material would enable lipid, a low-contrast material, to be visualised using spectral CT. The first experiment observed that at 10 mg/ml LDL, there was no measurable iodine signal in the liquid LDL samples in its native (control) or iodinated form. In the precipitated LDL however, both the native and iodinated samples revealed a significant iodine signal not only in the pellet but also throughout the 50% water 50% TCA solution the pellets were held in. The chlorine atoms in the TCA were recognised as an iodine signal in the material decomposition, which led to future pellet experiments being held in air in the PCR tubes. The following experiment effectively joined gold and iodine to 10 mg/ml precipitated LDL, with the material decomposition measuring a gold signal in the Au-LDL pellet in the range 13-14 mg/ml across axial, coronal, and sagittal slices. Iodine measurements produced a signal in the I-LDL pellet in the range 65-74 mg/ml across axial, coronal, and sagittal slices. The native n-LDL pellet produced no gold or iodine signal as anticipated, displaying as water in the MD. This optimised method was adapted to U937 cells, however the insufficient amount of LDL added to the cells (maximum concentration at 2 mg/ml) led to no gold or iodine contrast detected in the cell samples. The most suitable next step would be to repeat the experiment using ox-LDL rather than native-LDL, which may increase the uptake by the cells.

Ferric nitrate experiments were performed to optimise phantom studies for distinguishing iron and calcium. By principle of iron and calcium's similar spectral profiles, MARS MD showed misidentifications between particular ferric nitrate and hydroxyapatite material concentrations. Using the energy information from these misidentified materials, the material concentrations could be distinguished. This clearly demonstrates the superior ability of spectral CT technology over conventional CT in separating materials relevant in atherosclerosis. Initially using large ferric nitrate concentrations, small concentrations were studied, which more closely represented concentrations of iron in the body. Although there was no obvious misidentification, the small ferric nitrate concentrations were too small for the MARS system to accurately identify them as containing ferric nitrate using the MARS Vision material decomposition. Throughout the ferric nitrate experiments, an attempt was made to scan the ferric nitrate phantoms using two scanning protocols: the protocol currently used for ferric nitrate scanning, and the protocol used for plaque scanning. This undertaking was unsuccessful, due to errors when initiating the MD to run for the plaque protocol. With the long term goal of scanning atherosclerotic plaques to visualise intraplaque haemorrhage, an optimised phantom and scanning protocol is essential. Further work is necessary to develop an optimised phantom and protocol based on these findings, in order to make intraplaque haemorrhage and calcification visualisation attainable at the clinical level using MARS spectral CT.

This thesis also demonstrates the MARS spectral scanners ability to identify components of atherosclerotic plaque by investigating excised plaque specimens from patients and plaque development in mouse models. In the plaque study, large calcifications were observed around the bifurcation region of the artery. There were no obvious lipid signals attributing to a necrotic lipid core in the plaques. The ability to identify lipid may be a result of the protocol used. The Al protocol may identify more voxels as calcium (with no set thresholds), and hence the MD cannot give an accurate lipid content. Areas of further investigation include scanning with a different protocol, which may be less sensitive to the calcium channel. ApoE mice showed possible lipid deposition in the area of the body suspected to be the liver. By excising the apoE mouse aorta and liver, and scanning separately after the whole mouse scan, visualisation of calcifications was significantly more identifiable. The ability to identify regions of calcifications and lipid depositions around the bifurcation region in excised apoE mouse organs is promising, but more important is the ability to identify these materials in a whole mouse scan. Challenges of this include areas of the mouse body obstructing the view of specific regions of the aorta and arteries, reduced resolution and image contrast. The use of injectable contrast agents such as gold nanoparticles will be a future step in visualising atherosclerosis with the apoE mouse model.

The work in this thesis has established many avenues for future work. In regards to lipid experiments, the U937 cell study could be revisited, using ox-LDL rather than native-LDL (which

was used throughout the LDL experiments). This may increase the uptake and signal of the contrast agents gold and iodine. Another modification for the U937 study would be looking into increasing the number of iodine or gold atoms per LDL, hence a higher expectation of detecting a signal from the contrast agents if the rate of uptake remained the same. Ferric nitrate studies encompassed a large portion of this thesis. Future work includes creating an optimised protocol that is capable of scanning plaques for calcifications and intraplaque haemorrhages. This was attempted by using two scanning protocols to compare results, however issues running the MD meant only one protocol could be used for analysis. For the FeCl/CaCl experiment, different concentrations within the mixture solution could be trialled, to determine what concentrations of iron and calcium create the turning point at which iron is distinguished over calcium. Principal component analysis (PCA) was applied to ferric nitrate datasets to observe its ability to distinguish materials. Improvements to the PCA code to incorporate more than one material into the ROI selection could improve the ability of PCA to distinguish materials. There was success in scanning plaque specimens, apoE mice and excised mice aorta and liver. Next steps include lipid staining of plaques and histology to confirm the presence of lipid with the images from MARS Vision. Future work could also involve scanning plaque specimens and apoE mice with the ferric nitrate phantom and protocol once this has been optimised, in the hope of observing intraplaque haemorrhage alongside calcifications. Work involving intravenous injection of gold nanoparticles into apoE mice to observe areas of contrast agent uptake would be a worthwhile ongoing experiment for atherosclerosis research using spectral CT.

This thesis details work contributing to the quantification of vulnerable atherosclerotic plaque features using MARS spectral CT. Multi-energy CT is a superior imaging modality for atherosclerosis research compared to current imaging modalities, enabling users to acquire multi-energy datasets from a single acquisition using a standard x-ray tube operated at a single accelerating voltage. This gives spectral CT the advantage over current imaging techniques, which do not possess the spatial resolution to distinguish material components by morphology nor the spectroscopic ability to determine the composition from characteristic spectral information. Until a suitable technique becomes clinically available, the field of medical imaging will be restricted in its ability to identify vulnerable atherosclerotic plaque in patients. This thesis demonstrates the potential of spectral CT to identify material components of atherosclerotic plaque in vivo, which relates to the long term goals of the MARS group, as they translate this technology to a commercial, human scale MARS scanner. With application in atherosclerosis many other diseases, the MARS spectral scanner is a true asset in the field of medical imaging.

Bibliography

[1] G. Soloperto and S. Casciaro, "Progress in atherosclerotic plaque imaging," *World J Radiol*, vol. 4, no. 8, pp. 353–371, 2012.

[2] Z. R. Binti, "Spectral micro-ct imaging of ex vivo atherosclerotic plaque," Ph.D. dissertation, University of Canterbury, 2012.

[3] J. P. Ronaldson, R. Zainon, N. J. Scott, S. P. Gieseg, A. P. Butler, P. H. Butler, and N. G. Anderson, "Toward quantifying the composition of soft tissues by spectral ct with medipix3," *Med. Phys.*, vol. 39, no. 11, pp. 6847–6857, 2012.

[4] N. H. Foundation, "Heart foundation," https://www.heartfoundation.org.nz.

[5] N. G. Anderson and A. P. Butler, "Clinical applications of spectral molecular imaging: potential and challenges," *Contrast media and molecular imaging*, vol. 9, pp. 3–12, 2014.

[6] I. Danad, Z. A. Fayad, M. J. Willemink, and J. K. Min, "New applications of cardiac computed tomography," *Cardiovascular Imaging*, vol. 8, no. 6, pp. 710–723, 2015.

[7] R. Zainon, J. P. Ronaldson, T. Janmale, N. J. Scott, T. M. Buckenham, A. P. H. Butler, P. H. Butler, R. M. Doesburg, S. P. Gieseg, J. A. Roake, and N. G. Anderson, "Spectral ct of carotid atherosclerotic plaque: comparison with histology," *Molecular Imaging*, vol. 22, pp. 2581–2588, 2012.

[8] M. M. Sadeghi, D. K. Glover, G. M. Lanza, Z. A. Fayad, and L. L. Johnson, "Imaging atherosclerosis and vulnerable plaque," *J Nucl Med*, vol. 51, no. 5, pp. 51S–65S, 2010.

[9] M. Wintermark, S. S. Jawadi, J. H. Rapp, and et al, "High-resolution ct imaging of carotid artery atherosclerotic plaques," *Am J Neuroradiol*, vol. 29, pp. 875–882, 2008.

[10] A. C. Langheinrich, M. Kampschulte, C. CroBmann, R. Moritz, W. S. Rau, R. M. Bohle, and E. L. Ritman, "Role of computed tomography voxel size in detection and discrimination of calcium and iron deposits in atherosclerotic human coronary artery specimens," *J Comput Assist Tomogr*, vol. 33, no. 4, pp. 517–522, 2009.

[11] L. Badimon, T. Padro, and G. Vilahur, "Atherosclerosis, platelets and thrombosis in acute ischaemic heart disease," *European Heart Journal: Acute Cardiovascular Care*, vol. 1, no. 1, pp. 60–74, 2012.

[12] K. R. Feingold and C. Grunfeld, "Introduction to lipids and lipoproteins," https://www.ncbi.nlm.nih.gov/books/NBK305896/.

[13] P. C. Choy, Y. L. Siow, D. Mymin, and K. O, "Lipids and atherosclerosis," *Biochemistry and Cell Biology*, vol. 82, no. 1, pp. 212–224, 2004.

[14] K. J. Moore and I. Tabas, "The cellular biology of macrophages in atherosclerosis," *Cell*, vol. 145, no. 3, pp. 341–355, 2011.

[15] K. Moore, F. Sheedy, and E. Fisher, "Macrophages in atherosclerosis: a dynamic balance," *Nature reviews immunology*, vol. 13, no. 10, pp. 709–721, 2013.

[16] I. Tabas, "Lipids and atherosclerosis," *Biochemisty of Lipids, Lipoproteins and Membranes*, pp. 573–597, 2002.

[17] G. Maiolino, G. Rossitto, P. Caielli, V. Bisogni, G. P. Rossi, and L. A. Calo, "The role of oxidised low-density lipoproteins in atherosclerosis: The myths and the facts," *Mediators of Inflammation*, 2013.

[18] E. Leiva, S. Wehinger, L. Guzman, and R. Orrego, "Role of oxidised ldl in atherosclerosis," *Intech*, pp. 55–77.

[19] R. Delewi, H. Yang, and J. Kastelein, "Atherosclerosis," https://www.textbookofcardiology.org/wiki/Atherosclerosis.

[20] M. C. Houston, "New concepts in cardiovascular disease," https://restorativemedicine.org/journal/new-concepts-cardiovascular-disease/.

[21] W. Cai, T. Gao, H. Hong, and J. Sun, "Applications of gold nanoparticles in cancer nanotechnology," *Nanotechnol Sci Appl*, vol. 4, no. 1, pp. 17–32, 2008.

[22] J. F. Hainfeld, D. N. Slatkin, T. M. Focella, and H. M. Smilowitz, "Gold nanoparticles: a new x-ray contrast agent," *The British Journal of Radiology*, vol. 79, pp. 248–253, 2006.

[23] G. J. Strijkers, "Targeted nanoparticles for cardiovascular molecular imaging," *Current Radiology Reports*, vol. 1, pp. 191–204, 2013.

[24] D. P. Cormode, E. Roessl, A. Thran, T. Skajaa, R. E. Gordon, J.-P. Schlomka, V. Fuster, E. A. Fisher, W. J. M. Mulder, R. Proksa, and Z. A. Fayad, "Atherosclerotic plaque composition: Analysis with multicolor ct and targeted gold nanoparticles," *Radiology*, vol. 256, no. 3, pp. 774–782, 2010.

[25] D. A. Handley, C. M. Arbeeny, L. D. Witte, and S. Chien, "Colloidal gold-low density lipoprotein conjugates as membrance receptor probes," *Proceedings of the National Academy of Sciences of the USA*, vol. 78, no. 1, pp. 368–371, 1981.

[26] I. E. Allijn, J. Tang, A. J. Mieszawska, F. Fay, G. Ma, S. Russell, C. B. Callo, R. E. Gordon, E. Korkmaz, J. A. Post, Y. Zhao, H. C. Gerritsen, A. Thran, R. Proksa, H. Daerr, G. Storm, V. Fuster, E. A. Fisher, Z. A. Fayad, W. J. M. Mulder, and D. P. Cormode, "Gold nanoparticle labelling allows low-density lipoprotein imaging from the subcellular to macroscopic level," *ACS Nano*, vol. 7, no. 11, pp. 9761–9770, 2013.

[27] E. A. Merritt, "X-ray absorption edges," http://skuld.bmsc.washington.edu/scatter/data/Au.htmls.

[28] A. C. Langheinrich, M. Kampschulte, T. Buch, and R. M. Bohle, "Vasa vasorum and atherosclerosis - quid novi?" *Journal of Thrombosis and Haemostasis*, vol. 97, pp. 873–879, 2007.

[29] J. C. Sluimer, M. J. Gijbels, and S. Heeneman, "Detection of intraplaque hemorrhage in mouse atherosclerotic lesions," *Methods in molecular biology*, vol. 1339, pp. 1339–348, 2015.

[30] O. College, "Haemoglobin," http://cnx.org/content/col11496/1.6/.

[31] T. P. Sharkey-Toppen, A. K. Tewari, and S. V. Raman, "Iron and atherosclerosis: Nailing down the novel target with magnetic resonance," *Journal of Cardiovascular Translational Research*, vol. 7, no. 5, pp. 533–542, 2014.

[32] G. J. Anderson, D. Darshan, S. J. Wilkins, and D. M. Frazer, "Regulation of systemic iron homeostasis: how the body responds to changes in iron demand," *Biometals*, vol. 20, pp. 665–674, 2007.

[33] J. Wang and K. Pantopoulos, "Regulation of cellular iron metabolism," *Biochemical Journal*, vol. 434, pp. 365–381, 2011.

[34] U. Hoffmann, F. Moselewski, K. Nieman, I.-K. Jang, M. Ferencik, A. M. Rahman, R. C. Cury, S. Abbara, H. Joneidi-Jafari, S. Achenbach, and T. J. Brady, "Noninvasive assessment of plaque morphology and composition in culprit and stable lesions in acute coronary syndrome and stable lesions in stable angina by multidetector computed tomography," *Journal of the Americal College of Cardiology*, vol. 47, no. 8, pp. 1655–1662, 2006.

[35] R. Rajendran, J. A. Ronals, B. K. Rutt, B. Halliwell, and F. Watt, "Does iron inhibit calcification during atherosclerosis?" *Free Radic Biol Med*, vol. 53, no. 9, pp. 1675–1679, 2012.

[36] J. D. Hutcheson, C. Goettsch, S. Bertazzo, N. Maldonado, J. L. Ruiz, W. Goh, K. Yabusaki, T. Faits, C. Bouten, G. Franck, T. Quillard, P. Libby, M. Aikawa, S. Weinbaum, and E. Aikawa, "Genesis and growth of extracellular vesicle-derived microcalcification in atherosclerotic plaques," *Nat Mater*, vol. 15, no. 3, pp. 335–343, 2016.

[37] J. L. Ruiz, J. D. Hutcheson, and E. Aikawa, "Cardiovascular calcification: current controversies and novel concepts," *Cardiovascular Pathology*, vol. 24, pp. 207–212, 2015.

[38] G. Pasterkamp and A. van der Steen, "Intraplaque haemorrhage: An imaging marker for atherosclerotic plaque destabilisation?" *Arterioscler Thromb Vasc Biol*, vol. 32, pp. 167–168, 2012.

[39] L. Parma, F. Baganha, P. H. Quax, and M. R. de Vries, "Plaque angiogenesis and intraplaque hemorrhage in atherosclerosis," *European Journal of Pharmacology*, vol. 816, pp. 107–115, 2017.

[40] G. Balla, H. S. Jacob, J. W. Eaton, J. D. Belcher, and G. M. Vercellotti, "Hemin: a possible physiological mediator of low density lipoprotein oxidation and endothelial injury," *Arterioscler Thromb Vasc Biol*, vol. 11, no. 6, pp. 1700–1711, 1991.

[41] J.-B. Michel, R. Virmani, E. Arbustini, and G. Pasterkamp, "Intraplaque haemorrhages as the trigger of plaque vulnerability," *European Heart Journal*, vol. 32, pp. 1977–1985, 2011.

[42] M. M. Kockx, K. M. Cromheeke, M. W. Knaapen, J. M. Bosmans, G. R. De Meyer, A. G. Herman, and H. Bult, "Phagocytosis and macrophage activation associated with hemorrhagic microvessels in human athrosclerosis," *Arterioscler Thromb Vasc Biol*, vol. 23, pp. 440–446, 2003.

[43] F. D. Kolodgie, H. K. Gold, A. P. Burke, D. R. Fowler, H. S. Kruth, D. K. Weber, A. Farb, L. Guerrero, M. Hayase, R. Kutys, J. Narula, A. V. Finn, and R. Virmani, "Intraplaque hemorrhage and progression of coronary atheroma," *N. Eng. J. Med.*, vol. 349, pp. 2316–2325, 2003.

[44] A. P. Levy and P. R. Moreno, "Intraplaque hemorrhage," *Current Molecular Medicine*, vol. 6, pp. 479–488, 2006.

[45] X. Yuan, W. Li, A. Olsson, and U. Brunk, "Iron in human atheroma and ldl oxidation by macrophages following erythrophagocytosis," *Atherosclerosis*, vol. 124, pp. 61–73, 1996.

[46] A. C. Langheinrich, A. Michniewicz, D. G. Sedding, B. Lai, S. M. Jorgensen, R. M. Bohle, and E. L. Ritman, "Quantitative x-ray imaging of intraplaque hemorrhage in aortas of apoe$^{-/-}$/ldl$^{-/-}$ double knockout mice," *Investigative Radiology*, vol. 42, no. 45, pp. 263–273, 2007.

[47] I. T. Jolliffe, "Principal component analysis," *Springer, New York*, 2002.

[48] A. P. H. Butler, J. Butzer, N. Schleich, N. J. Cook, N. G. Anderson, N. Scott, N. De Ruiter, R. Grasset, L. Tlustos, and P. H. Butler, "Processing of spectral x-ray data with principal components analysis," *Nuclear Instruments and Methods in Physics Research A*, vol. 633, pp. S140–S142, 2011.

[49] M. Ringnér, "What is principal component analysis," *Nature Biotechnology*, vol. 26, no. 3, pp. 303–304, 2008.

[50] J. R. Bennett, A. M. T. Opie, Q. Xu, H. Yu, M. Walsh, A. Butler, P. Butler, G. Cao, A. Mohs, and G. Wang, "Hybrid spectral micro-ct: System design, implementation, and preliminary results," *IEEE Transactions on Biomedical Engineering*, vol. 61, no. 2, pp. 246–253, 2014.

[51] I. T. Jolliffe, "Principal components analysis," *New York: Springer-Verlag*, 1986.

[52] A. R. Kalukin, M. Van Geet, and R. Swennen, "Principal component analysis of multienergy x-ray computed tomography of mineral samples," *IEEE Transactions on Nuclear Science*, vol. 47, no. 5, pp. 1729–1736, 2000.

[53] J. Butzer, A. P. H. Butler, P. H. Butler, P. J. Bones, N. Cook, and L. Tlustos, "Medipix imaging - evaluation of datasets with pca," *Accepted for presentation at Image and Vision Computing New Zealand, 2008. IVCNZ 2008. 23rd International Conference*, 2008.

[54] Z. Chen, M. Ichetovkin, M. Kurtz, E. Zycband, D. Kawka, J. Woods, X. He, A. S. Plump, and E. Hailman, "Cholesterol in human atherosclerotic plaque is a marker for underlying disease state and plaque vulnerability," *Lipids in Health and Disease*, vol. 9, no. 61, pp. 1–8, 2010.

[55] K. Athenstaedt, in *Neutral Lipids in Yeast: Synthesis, Storage and Degradation.* Springer, 2010, pp. 472–478.

[56] J. H. Rapp, W. E. Connor, D. S. Lin, T. Inahara, and J. M. Porter, "Lipids of human atherosclerotic plaques and xanthomas: clues to the mechanism of plaque progression," *J Lipid Res*, vol. 24, pp. 1329–1335, 1983.

[57] J. R. Guyton and K. F. Klemp, "Development of the atherosclerotic core region. chemical and ultrastructural analysis of microdissected atherosclerotic lesions from human aorta," *Arterioscler Thromb*, vol. 14, pp. 1305–1314, 1994.

[58] H. S. Kruth, "Localisation of unesterified cholesterol in human atherosclerotic lesion. demonstration of filipin-positive, oil-red-o-negative particles," *Am J Pathol*, vol. 114, no. 2, pp. 201–208, 1984.

[59] S. Xu, Y. Huang, Y. Xie, T. Lan, K. Le, J. Chen, S. Chen, S. Gao, X. Xu, X. Shen, H. Huang, and P. Lui, "Evaluation of foam cell formation in cultured macrophages: an improved method with oil red o staining and dil-oxldl uptake," *Cytotechnology*, vol. 62, pp. 473–481, 2010.

[60] H. S. Kruth and D. L. Fry, "Histochemical detection and differentiationof free and esterified cholesterol in swine atherosclerosis using filipin," *Experimental and Molecular Pathology*, vol. 40, pp. 288–294, 1984.

[61] D. Hirsch, R. Azoury, S. Sarig, and H. S. Kruth, "Colocalisation of cholesterol and hydroxyapatite in human atherosclerotic lesions," *Calcif Tissue Int*, vol. 52, pp. 94–98, 1993.

[62] P. Greenspan, E. P. Mayer, and S. D. Fowler, "Nile red: A selective fluorescent stain for intracellular lipid droplets," *The Journal of Cell Biology*, vol. 100, pp. 965–973, 1985.

[63] S. D. Fowler and P. Greenspan, "Application of nile red, a fluorescent hydrophobic probe, for the detection of neutral lipid deposits in tissue sections," *The Journal of Histochemistry and Cytochemistry*, vol. 33, no. 8, pp. 833–836, 1985.

[64] K. S. Meir and E. Leitersdorf, "Atherosclerosis in the apolipoprotein e-deficient mouse . a decade of progress," *Arterioscler Thromb Vasc Biol*, vol. 24, pp. 1006–1014, 2004.

[65] L. K. Curtiss and W. A. Boisvert, "Apolipoprotein e and atherosclerosis," *Curr Opin Lipidol*, vol. 11, pp. 243–251, 2000.

[66] S. H. Zhang, R. L. Reddick, J. A. Piedrahita, and N. Maeda, "Spontaneous hypercholesterolemia and arterial lesions in mice lacking apolipoprotein e," *Science*, vol. 258, pp. 468–471, 1992.

[67] G. Kolovou, K. Anagnostopoulou, D. P. Mikhailidis, and D. V. Cokkinos, "Apolipoprotein e knockout models," *Current Pharmaceutical Design*, vol. 14, pp. 338–351, 2008.

[68] A. Seitz, D. Gourevitch, X. Zhang, L. Clark, P. Chen, M. Kragol, and et al, "Sense and antisense transcripts of the apolipoprotein e genein normal and apoe knockout mice, their expression after spinal cord injury and corresponding human transcripts," *Hum Mol Genet*, vol. 14, pp. 2661–2670, 2005.

[69] T. P. O'Neill, "Apolipoprotein e-deficient mouse model of human atherosclerosis," *Toxicologic pathology*, vol. 25, no. 1, pp. 20–21, 1997.

[70] Y. Nakashima, A. S. Plump, E. W. Raines, J. L. Breslow, and R. Ross, "Apoe-deficient mice develop lesions of all phases of atherosclerosis throughout the arterial tree," *Arterioscler Thromb*, vol. 14, pp. 133–140, 1993.

[71] Y. Wang, M. Halks-Miller, R. Vergona, M. Sullivan, R. Fitch, C. Mallari, and et al, "Increased aortic stiffness assessed by pulse wave velocity in apolipoprotein e-deficient mice," *Am J Physiol Heart Circ Physiol*, vol. 278, pp. H428–34, 2000.

[72] C. Hartley, A. Reddy, S. Madala, B. Martin-McNulty, R. Vergona, M. Sullivan, and et al, "Hemodynamic changes in apolipoprotein e-deficient knockout mice," *Am J Physiol Heart Circ Physiol*, vol. 279, pp. H2326–34, 2000.